

BIO-INSPIRED STRUCTURAL COLORS: PHOTONIC BAND GAP TUNING IN COLLOIDAL PHOTONIC CRYSTALS AND APPLICATIONS

Thesis Submitted to AcSIR for the Award of the Degree of
DOCTOR OF PHILOSOPHY
in **CHEMICAL SCIENCES**



By
Vipin V. V.

Registration No: 10CC13J39001

Under the guidance of
Dr. Saju Pillai




**CSIR-NATIONAL INSTITUTE FOR INTERDISCIPLINARY
SCIENCE AND TECHNOLOGY (CSIR-NIIST)
THIRUVANANTHAPURAM-695019, KERALA, INDIA**

December, 2019

Dedicated to my family & all my teachers...

DECLARATION

I hereby declare that the Ph.D. thesis entitled “**Bio-inspired Structural Colors: Photonic Band Gap Tuning in Colloidal Photonic Crystals and Applications**” is an independent work carried out by me at the **Materials Science and Technology Division (MSTD), CSIR-National Institute for Interdisciplinary Science and Technology (CSIR-NIIST), Thiruvananthapuram** under the supervision of **Dr. Saju Pillai, Senior Scientist** and it has not been submitted anywhere else for any other degree, diploma, or title.


5/12/2019
Vipin V. V.

Thiruvananthapuram

December, 2019

**CSIR-NATIONAL INSTITUTE FOR
INTERDISCIPLINARY SCIENCE AND
TECHNOLOGY (CSIR-NIIST)**
Council of Scientific and Industrial Research (CSIR)
GOVERNMENT OF INDIA
Thiruvananthapuram-695019, India



Dr. Saju Pillai
Senior Scientist



Functional Materials Section
Materials Science and Technology Division

CERTIFICATE

This is to certify that the work incorporated in this Ph.D. thesis entitled “*Bio-inspired structural colors: Photonic Band Gap Tuning in Colloidal Photonic Crystals and Applications*” submitted by *Mr. Vipin V. V.* to *Academy of Scientific and Innovative Research (AcSIR)* in partial fulfilment of the requirements for the award of the *Degree of Doctor of Philosophy* in *Chemical Sciences* embodies original research work under my guidance. I further certify that this work has not been submitted to any other University or Institution in part or full for the award of any degree or diploma. Research materials obtained from other sources have been duly acknowledged in the thesis. Any text, illustrations and tables used in the thesis from other sources have also been duly cited and acknowledged.

Dr. Saju Pillai

(Thesis Supervisor)

Vipin V. V.

(Student)

Thiruvananthapuram

December, 2019

Telephone: 0471 2515489 (office) 09400553366 (mobile) **E-mail:** pillai_saju@niist.res.in

ACKNOWLEDGEMENTS

Dr. Saju Pillai, being my supervisor, I have immense pleasure and gratitude to recount my days of the past few years with him. The continuous encouragement, constant support and the mode of professionalism that he has induced in me not only influenced my career but also helped me a lot in my personal life. I really admire his positive attitude, great patience and compassionate behavior for his colleagues and others. His guidance, affection and the freedom he gave me during the course of my doctoral studies helped me to complete my thesis without any overexertion.

I am extremely thankful to Dr. K. G. K. Warriar for giving valuable advices in the initial stage of my research.

I wish to thank Dr. A. Ajayaghosh, Dr. Suresh Das and Dr. Gangan Prathap, present and former Directors of the CSIR-National Institute for Interdisciplinary Science and Technology for providing me the necessary facilities for carrying out the work.

I am thankful to Dr. C. H. Suresh, Dr. Luxmi Varma and Dr. Mangalam S. Nair, present and former AcSIR program co-ordinators at CSIR-NIIST, for timely help and advice for the academic procedures of AcSIR.

I would like to acknowledge Dr. Savithri, Dr. Harikrishna Bhat, Dr. P. Prabhakar Rao, Dr. M. L. P. Reddy and Dr. M.T. Sebastian, present and former Heads, MSTD for allowing me to conduct my research at MSTD.

Dr. E. Bhoje Gowd, Dr. T. P. D. Rajan and Dr. Joshy Joseph (DAC members) are acknowledged for their constant support and suggestions in DAC meetings.

I am grateful to Dr. J. D. Sudha and Dr. Adersh Asok for their valuable suggestions.

I am immensely thankful to Dr. Parvathy R. Chandran and Mr. Animesh M. R. for their valuable contribution in my research articles.

I express my sincere gratitude to Ms. Silpa T. S. for her valuable support. I thank Mrs. Aswathy Raju, Ms. Anu Thankappan, Mrs. Drisya and Mrs. Harsha Harish for their valuable contribution in my research works.

I am grateful to Mr. A. Peer Mohamed for his constant support and help in characterization facilities at the Functional Materials Section. I am also thankful to Dr. Subrata Das, Mr. Kiran, Mr. Robert Philip, Mrs. Lucy Paul, Mrs. Soumya, Mr. M. R. Chandran, Mr. Harish and Ms. Anju P. for supporting with characterization techniques.

I will cherish the memorable days with my lab mates, Dr. Reny thankam Thomas, Dr. Aswathy, Mrs. Sumina N. B, Mrs. Nabeela Kallayi, Mrs. Raji V Nair, Ms. Meghana Mary Thomas, Ms. Hasna Hakkim, Ms. Gopika P, Mr. Rahul Raj, Ms. Adithya, Mr. Deepu mohan, Mr. Achu R, Ms. Manasi Ingle, Ms. Athira, Ms. Anupama, Ms. Hemaja, Ms. Farsana, Mr. Yadhu Krishanan, Ms. Rohini, Ms. Anna Shaji.

I am thankful to Dr. Manu Jose, Dr. P. Shaiju, Dr. Baku Nagendra, Dr. Harsha. N., Dr. Sandeep. C, Dr. Arindamal, Mr. Vijayakumar and Mr. Rajeev for the valuable suggestions and support during my research work.

I express my heartfelt thanks to Mrs. Sijila Rosely, Mrs. Deepthi Krishnan, Mr. Sivaprasad, Ms. Praveena, Mrs. Sruthi, Ms. Ashitha, Mr. Virat, Mr. Renjith, Mr. Ashish and Ms. Jerin for their support and help in the entire research work.

Words fall short in expressing my gratitude to my friends Mr. Sujai P. T., Mr. John Paul, Mr. Vipin G. Krishnan, Mr. Sujith and Dr. Baiju T. V. for their lovely companionship that made my stay at Trivandrum unforgettable.

No words can reproduce my heartfelt love and gratitude I have for my parents, sisters and relatives. I would also like to thank my in-laws for their love, and support. I thank them all for the endless love, constant encouragement and prayers to achieve this goal in my life.

I acknowledge UGC, New Delhi, for the financial support.

Above all, I bow to the Almighty for bestowing his blessings upon me.

CONTENTS

Declaration	i
Certificate	ii
Acknowledgments	iii
Contents	iv
List of figures	ix
List of schemes	xvii
List of tables	xix
List of abbreviations	xxi
Abstract	xxiii
Chapter 1 Introduction	(3-42)
1.1. Structural colors	3
1.2. History of remarkable studies on structural color	4
1.3. Structural color from photonic crystals (PCs) material and existence of photonic band gap (PBG) in PCs	5
1.4. Classification of PCs	6
1.5. PCs found in nature	7
1.5.1. Color changing stimuli-responsive PCs found in nature	8
1.6. Fabrication of PC	10
1.7. Colloidal self-assembly and colloidal PC	10
1.7.1. Building blocks in colloidal self-assembly	12
1.7.2. Forces in colloidal self-assembly	13
1.7.2.1. Repulsive forces	13
1.7.2.2. Attractive forces	14

2.3.2. Synthesis of polystyrene (PS) microspheres and fabrication of PS CPCs	48
2.3.3. Fabrication of PS CPCs	49
2.3.4. Preparation of PS CPC powder	49
2.3.5. Fabrication of silica IO-PC using PS CPCs as template and preparation of silica IO-PC powder	49
2.3.6. Characterization	49
2.4. Results and Discussion	50
2.4.1 Synthesis monodispersed PS microspheres	50
2.4.2. Fabrication of PS-based CPCs	55
2.4.2.1. Pre-treatment of substrate	55
2.4.2.2. Fabrication of PS-based CPCs by evaporation induced vertical deposition method	56
2.4.3. Structural color and tuning of PBG in PS CPCs	59
2.4.4. Fabrication of PS CPC on flexible substrate	63
2.4.5. Structure, defect, contact angle and thermal stability of PS CPC	63
2.4.6. Angle-dependent structural color in PS CPCs	65
2.4.7. Mechanism of colloidal self-assembly	66
2.4.8. Optical properties of PS CPC powder	67
2.4.9. Fabrication of silica IO-PC using PS CPC as a template	68
2.4.10. Optical properties of silica IO-PC powder	70
2.5. Conclusion	72
References	73

Chapter 3	Fluorescence enhancement of dye by tuning the photonic band gap and host-guest complex formation	(79-100)
3.1. Abstract		79
3.2. Introduction		79
3.3. Experimental		82
3.3.1. Chemicals and materials		82
3.3.2. Synthesis of polystyrene (PS) microspheres and fabrication of PS CPCs		82
3.3.3. Preparation of CB7-RhB host-guest complex		83
3.3.4. Preparation of fluorescent PS CPC films		83
3.3.5. Characterization		84
3.4. Results and discussion		84
3.4.1. Fabrication of PS-based CPCs		84
3.4.2. Fluorescence enhancement of RhB dyes on PS CPC		86
3.4.3. Host-guest complexation triggered enhanced fluorescence		90
3.4.4. Host-guest complexation and PBG effect triggered enhanced fluorescence		92
3.4.5. Mechanism of fluorescence enhancement		93
3.5. Conclusion		98
References		98
Chapter 4	Aptasensor based on stimuli-responsive photonic crystals of core-shell microspheres for pesticide detection	(103-125)
4.1. Abstract		103
4.2. Introduction		103

4.3. Experimental	107
4.3.1 Chemicals and materials	107
4.3.2. Synthesis and self-assembly of Monodispersed PS@poly(MMA-EGDMA-AA) core-shell microspheres	107
4.3.3. Fabrication of aptasensor based on RPC (RPC-A)	108
4.3.4. Characterization	108
4.4. Results and Discussion	109
4.4.1. Synthesis monodispersed PS@poly(MMA-EGDMA-AA) core-shell Microspheres	109
4.4.2. Fabrication of CS microsphere-based PCs (CS-RPCs)	112
4.4.3. Fabrication of photonic crystals-based aptasensor (RPC-A) and sensing of Omethoate	116
4.4.4. Selectivity studies of RPC-A	121
4.5. Conclusions	123
References	123
Chapter 5	129
Summary and Scope of Future Work	129
Thesis output	131

LIST OF FIGURES

Figure No.	Title	Page No.
Chapter 1		
Fig. 1.1.	Structural color seen in a) butterfly b) beetle and c) peacock	3
Fig. 1.2.	a) Schematic of diffraction of incident light wavelength in a typical PC at PBG and b) Blue coloration of a bird due to the existence of PBG at blue color	6
Fig. 1.3.	Classification of PC according to crystal arrangement	7
Fig. 1.4.	a-g) Schematic, morphology of microstructure and photographs of structural color found in some well-studied natural creatures h and i) photograph and SEM image of an opal stone	8
Fig. 1.5.	a) Stimuli-responsive color change in <i>Paracheirodon innesi</i> by swelling induced alteration in lattice spacing and b) Stimuli-responsive color change in a beetle by refractive index variation	9
Fig. 1.6.	a), b) Photograph of reversible color change of a male chameleon during relaxed and excited state, c) and d) corresponding TEM images showing the changes in lattice spacing	10
Fig. 1.7.	SEM images of a) CC, c) colloidal amorphous array of silica particles, b) and d) represent corresponding digital photographs showing the structural color. The scale bar is 1 μm and 1 mm for SEM images and digital photographs, respectively	11
Fig. 1.8.	Schematic of colloidal particles having various shapes employed in colloidal self-assembly	13
Fig. 1.9.	Schematic diagram of various forces acting during colloidal self-assembly process on solid substrate	15

Fig. 1.10.	SEM images of 1D b), c) planar view and section view of 2D, d) 3D e) binary and f) polynary CCs	16
Fig. 1.11.	Different types of colloidal self-assembly method (a) air-liquid interface assembly, (b) evaporation deposition, (c) electrophoretic deposition, (d) sedimentation, (e) dipping deposition, (f) slit filling	18
Fig. 1.12.	a) Schematic diagram of Bragg diffraction b) Reflectance spectra of CC showing PBG (inset figure shows SEM image) c) schematic diagram of thin-film interference and d) structural color of CC (inset figure shows SEM image) Thin film	19
Fig. 1.13.	Self-assembled colloidal structure having a) long-range ordered arrangement with angle-dependent structural color b) short-range ordered arrangement with angle-independent structural color	20
Fig. 1.14.	PBG diagram of a typical PC	21
Fig. 1.15.	a) Schematic diagram showing the template-based fabrication process of macroporous inverse opal b), c) SEM images of silica inverse opal (scale bar: 2 μm) and acrylic acid-based inverse opal hydrogel	22
Fig. 1.16.	Stimuli-response of a PC by changes in lattice spacing via swelling or deswelling mechanism	23
Fig. 1.17.	a) Structural color of thermoresponsive PC gel b) Reflectance spectra of thermoresponsive PC gel at different temperature	24
Fig. 1.18.	a) Mechanism of color change of PC of PS colloid in PDMS film and b) corresponding blue shift in diffraction peak	24
Fig. 1.19.	Photoisomerization of an optically active molecule between two form under UV and visible light	25
Fig. 1.20.	a) Mechanism of surfactant detection via swelling induced lattice spacing change b) surfactant concentration dependent diffraction wavelength shift and corresponding changes in structural color is shown in the inset	26

Fig. 1.21.	a) SEM images and powder X-ray diffraction pattern of the nanocrystalline TiO ₂ inverse opal b) enhancement factor of photocatalytic degradation of methylene blue on TiO ₂ inverse opal with different PBG at 0° and 45° normal to the films, c) Schematic diagram of a DSC coupled with PC structure d) SEM image of inverse opal TiO ₂ , e) Schematic of a double heterostructure PC f) Enhancement factor of Rhodamine B on E, F, E-F, F-E, E-F-E and F-E-F PCs	28
Fig. 1.22.	Inkjet printed QR code consisting of bumps, plates, and coffee-rings shaped PC dots which show four images under different lighting condition	29
Fig. 1.23.	a) PC based on shape memory polymer showing solvent responsive color change, b) angle-dependent color changing PC pattern, c) angle-dependent color changing inverse opal PC pattern and d) inkjet-printed PC pattern showing colored and colorless appearance under different lighting condition	30
Fig. 1.24.	a) Schematic of fabrication of inverse opal gel b) schematic of cell structure and c) color change of PC at different voltage	31

Chapter 2

Fig. 2.1.	a) Digital photograph of PS microspheres suspension, b) SEM image, c) and d) TEM images of PS microspheres	51
Fig. 2.2.	a), b) and c) Particle size distribution of PS microsphere synthesized by varying the mol % of monomer (styrene)	53
Fig. 2.3.	a) FTIR spectra and b) XPS high-resolution C1s narrow scan of PS microspheres	54
Fig. 2.4.	a) TGA and b) DSC curve of PS microspheres	55
Fig. 2.5.	Contact angle measurements of a), c) before pre-treatment and b), d) after pre-treatment on glass substrate and flexible polymer substrate mylar film, respectively	56

Fig. 2.6.	Schematic representation of a) vertical deposition method, b) represents experimental set-up of vertical deposition method on a water bath, c) digital photograph of PS colloid suspension and CPC fabricated from it, d-f) represents the SEM image of PS CPC obtained using vertical deposition method in desiccator at a relative humidity of 90 %, 74 %, and 30 % respectively, and g-h) represents the SEM images of PS CPC obtained using vertical deposition method on water bath at 70 and 55 °C respectively	58
Fig. 2.7.	a) Digital photograph of PS CPCs on a glass substrate, b) SEM micrographs, (corresponding digital photographs in the inset) and c) reflectance spectra of violet, green and orange colored PS CPCs	61
Fig. 2.8.	Reflectance spectra of a) violet, b) green and c) orange CPCs of varying film thicknesses.	62
Fig. 2.9.	a) b), c) represents digital photograph of PS CPC on flexible substrate and d) demonstrate the structural stability of PS CPC film under mechanical bending conditions	63
Fig. 2.10.	a), b), c), d) represents the SEM micrograph of PS CPCs revealing the structure and defects, e) represents contact angle measurement of PSCPC, f), g), h) and i) represents SEM micrograph of PS CPC at RT, 110°C, 150°C and 180°C, respectively.	64
Fig. 2.11.	a), b) represents the structural color of a violet PS CPC at different viewing angle and c) shows the structural color of a green PS CPC on a flexible substrate revealing different colors at different areas due to the changes in viewing angle	65
Fig. 2.12.	a) Mechanism of colloidal-self-assembly in vertical deposition method and b) capillary force acting at the triple phase boundary which direct the colloid particles to come together	67
Fig. 2.13.	a) Digital photograph of orange PS CPC and CPC powder, b) and c) SEM images of PS CPC powder at different	68

magnifications, 10 μm and 5 μm respectively, d and e) represents OM images of PS CPC powder with scale bar 250 μm and 100 μm respectively, f) and g) depicts schematic representation depicting the reflection in both CPC film and CPC powder, respectively

- Fig. 2.14.** a) Schematic representation of PS CPC based template fabrication of silica IO-PC, b) digital photograph of silica IO-PC, c) and d) represents SEM images at different magnifications, 1 μm and 500 nm respectively, and f) represents the FTIR spectra of silica IO-PC. 69
- Fig. 2.15.** a) photograph of silica IO-PC powder, b) and c) represents SEM image of silica IO-PC powder (Scale bar: 10 μm and 1 μm), d) represents OM image of silica IO-PC powder (Scale bar: 100 μm) and e) represents the schematic diagram showing reflection in silica IO-PC powder 70
- Fig. 2.16.** a) Digital photograph, b) SEM image of charcoal powder respectively, c), d) Digital photograph of 4 and 8 weight % charcoal containing silica IO-PC powder respectively, e) and f) SEM image of charcoal containing silica IO-PC powder and schematic representation of reflection in charcoal containing silica IO-PC powder 72

Chapter 3

- Fig. 3.1.** SEM micrographs, corresponding digital photographs (inset) and b) reflectance spectra of violet, green and orange colored PS CPCs with film thickness of 6.8, 9.0 and 7.5 μm , respectively. 85
- Fig. 3.2.** a) Absorption and b) FL spectra of 10^{-6} M aqueous RhB solution 87

Fig. 3.3.	a) Schematic representation of the control sample and all the CPC samples b) FLmax from different points of RhB coated control samples (PS)	88
Fig. 3.4.	Fluorescence spectra of RhB on violet, green and orange colored PS CPCs	89
Fig. 3.5.	Fig. 3.5. a) Absorption spectra of 10^{-6} M aqueous solution of RhB in the presence of various molar ratio of CB7 b) FL maxima of 10^{-6} M aqueous solution of RhB in the presence of various molar ratio of CB7 and c) Digital photographs of aqueous solution of RhB in the presence of various molar ratio of CB7	91
Fig. 3.6.	Fluorescence spectra of CB7-RhB complex of different molar ratio of CB7 a) 0.5, b) 1, and c) 1.5 on various PS CPCs and d) Fluorescence enhancement factor of RhB, CB-RhB ₁ , CB-RhB ₂ and CB-RhB ₃ on violet, green and orange colored PS CPCs	93
Fig. 3.7.	a) Fluorescence spectra of RhB and CB-RhB ₁ , CB-RhB ₂ and CB-RhB ₃ on planar PS film b) Fluorescence enhancement factor of CB-RhB ₁ , CB-RhB ₂ and CB-RhB ₃ with respect to RhB coated planar PS film c) Fluorescence decay curves of RhB and CB-RhB ₃ on planar PS film and d) Fluorescence enhancement factor of CB-RhB ₁ , CB-RhB ₂ and CB-RhB ₃ on violet, green and orange colored CPC films, calculated using host-guest complex coated planar PS film of corresponding molar ratio as control sample	97

Chapter 4

Fig. 4.1.	a) Digital photograph b) DLS spectrum of CS microsphere suspension, and c) TEM image of CS microspheres	110
Fig. 4.2.	a) FT-IR spectra b) XPS survey spectra and c) C1s narrow scan of CS microspheres	111

Fig. 4.3.	a) TGA and b) DSC curve of CS microspheres	112
Fig. 4.4.	a) Digital photograph, b) SEM image and c) reflectance spectra of CS-RPC respectively	113
Fig. 4.5.	a) Digital photographs of CS-RPC at various viewing angle, b) and c) represents schematic representation of arrangement of uniform and non-uniform CS microsphere in CS-RPC, respectively	115
Fig. 4.6.	a) and b) represents digital photograph and SEM micrograph of PVA-RPC film	116
Fig. 4.7.	a), b) represent XPS survey spectra of PVA-RPC and RPC-A respectively, c), d) represents C1s and N1s narrow scan of RPC-A and e) represents the SEM micrograph of RPC-A film	118
Fig. 4.8.	Reflectance spectra of dried RPC-A and RPC-A after equilibrating with water	119
Fig. 4.9.	a) and b) represents reflectance spectra and corresponding λ_{\max} of RPC-A film in different concentrations of omethoate solutions, respectively, c) represents reflectance spectra of non-functionalized PVA-RPC film in different omethoate solutions	121
Fig. 4.10.	a), b) represents reflectance spectra and corresponding λ_{\max} of RPC-A film in different methyl parathion solutions respectively and c), d) represents reflectance spectra and corresponding λ_{\max} of RPC-A film in different carbofuran solutions respectively	122

LIST OF SCHEMES

Scheme No.	Title	Page No.
Chapter 3		
Scheme 3.1	Schematic illustration of the method adopted for fluorescence enhancement	82
Scheme 3.2	Schematic representation of mechanism of fluorescence enhancement of RhB and CB7-RhB host-guest complex on PS CPC films	95
Chapter 4		
Scheme 4.1	Mechanism of omethoate sensing using core-shell microsphere RPC: a) Shrinking of hydrogel shell in the presence of omethoate and corresponding blue shift in Bragg diffraction and b) binding mechanism of omethoate with DNA-aptamer on the core-shell microsphere.	106
Scheme 4.2	Covalent coupling of aptamer with carboxyl group of CS microsphere in PVA-RPC via EDC-NHS coupling	117

LIST OF TABLES

Table No.	Title	Page No.
Chapter 2		
Table 2.1.	Amount of styrene, corresponding hydrodynamic diameter, PDI and zeta potential of as-synthesized PS microspheres	52
Table 2.2	Atomic % of PS microspheres from XPS data	54
Table 2.3.	Contact angle measurements of glass substrate and a flexible polymer substrate before and after pre-treatment	56
Table 2.4.	Experimental setup, relative humidity, temperature and time of vertical deposition method	59
Table 2.5.	Particle size and photonic band gap (PBG) positions of violet, green and orange colored PS CPCs	61
Chapter 3		
Table 3.1.	Photonic band gap positions of violet, green and orange colored PS CPCs	86
Table 3.2.	Fluorescence enhancement factor of methylene blue on violet, green and orange colored CPCs	90
Table 3.3.	Fluorescence lifetime T_i , relative percentage (in parenthesis) and average life-time T_{Av} of RhB and CB-RhB ₃ on planar PS film	98
Chapter 4		
Table 4.1.	Atomic % of CS and PS microspheres from XPS data	111
Table 4.2.	Atomic % of PVA-RPC and RPC-A	119

LIST OF ABBREVIATION

3D-OM	Three-dimensionally ordered macroporous
AA	Acrylic acid
CB	Cucurbituril
CB7	Cucurbit[7]uril
CB10	Cucurbit[10]uril
CC	Colloidal Crystal
CPC	Colloidal Photonic Crystals
CS	Core-Shell
CS-RPC	Photonic crystals of CS microspheres
DLS	Dynamic Light Scattering
DSC	Differential Scanning Calorimetry
EGDMA	Ethylene glycol dimethacrylate
EDC	Ethyl-3-(3-dimethylaminopropyl)carbodiimide
FE-SEM	Field-Emission Scanning Electron Microscope
FT-IR	Fourier Transform-Infrared
IO	Inverse Opal
IOH_{PAM}	Polyacrylamide Inverse Opal Hydrogel
IO-PC	Inverse Opal Photonic Crystal
LB	Langmuir Blodgett technique
LOD	Limit of Detection
MMA	Methyl methacrylate
NHS	N-Hydroxysuccinimide
OM	Optical Microscope
PBG	Photonic Band Gap
PC	Photonic Crystal
PDI	Polydispersity index
PS	Polystyrene

PVA	Polyvinyl alcohol
QD	Quantum Dots
RhB	Rhodamine B
RPC	Stimuli-responsive PC
RPC-A	RPC aptasensor
SDS	Sodium dodecyl sulfate
SEM	Scanning Electron Microscope
TCSPC	Time-Correlated Single-Photon Counting
TEM	Transmission Electron Microscope
TEOS	Tetraethyl orthosilicate
TGA	Thermogravimetric Analysis
XPS	X-ray Photoelectron Spectroscopy

Abstract

Structural colors, originated due to the interaction of light with micro or nano-structures, are bright and resistant to photobleaching. They are produced by optical phenomena like interference, diffraction, scattering, etc. Structural color from the marvelous periodic architecture seen in a living organism, such as butterflies, beetles, peacocks, etc. has attracted the scientific community to develop bio-inspired structurally colored materials. Photonic crystals (PCs) are a special class of materials that exhibit brilliant structural color due to Bragg diffraction from the periodic architecture. The unique optical properties of PCs due to the existence of photonic band gap (PBG) offer a potential platform for controlling the propagation of light. Self-assembly of colloidal particles offer a cost-effective way for colloidal photonic crystal (CPC) fabrication. Among different types of fabrication methods, the present thesis is focused on the colloidal self-assembly method for PC fabrication.

CPCs, prepared by the colloidal self-assembly method, are well-ordered periodic dielectric architectures of monodispersed inorganic/polymeric microspheres. A typical CPC consists of periodic arrangement of colloidal microspheres and air-voids. Among various methodologies of CPCs fabrication, the vertical deposition method offers three-dimensional (3D) CPC with very few structural defects. CPCs possess unique optical properties with both angle-dependent and angle-independent structural colors. By tuning PBG via the diameter of colloidal microspheres, CPCs of different structural colors can be obtained from their respective colloidal suspensions. Furthermore, using CPC as a sacrificial template and infiltrating a secondary material in the air-voids, macroporous inverse opal PC (IO-PC) can be fabricated by inverting CPC structure. Moreover, slow photon at the PBG edge, known as PBG effect is very promising to increase light-matter interaction. Interestingly, CPCs having stimuli-responsive materials shows PBG shift in the presence of external stimuli and thus paves the way to produce color changing stimuli-responsive CPCs (RPCs) viable for various applications such as

chemical/biochemical sensor for safety (food and environment) and product authentication.

Among various applications of CPCs, the present thesis deals with some of the research problems associated with IO-PC, PC enhanced fluorescence of dye molecules using PBG effect and RPCs.

Firstly, experimental conditions for the synthesis of highly monodispersed polystyrene (PS) microspheres and the fabrication of PS based colloidal PCs (PS CPCs) were optimized. Large-area CPCs with orderly arranged PS microspheres and brilliant structural color are prepared by evaporation induced vertical deposition method on a plasma-treated hydrophilic glass substrate as well as on a flexible polymer film. The PBG of PS CPCs is tuned by varying the diameter of PS microspheres. PS CPCs showed an angle-dependent structural color with respect to viewing angle. CPC coatings on flexible polymer films exhibit excellent structural stability even upon bending the substrate. Additionally, PS CPCs were used as a sacrificial template for the preparation of three-dimensionally ordered macroporous (3D-OM) silica IO-PC. However, the powder form of silica IO-PC was white and lost the structural color due to the random orientation of the particles in the silica IO-PC powder and the scattering of light. To make structural color visible in powder silica IO-PC, charcoal flakes are used as a background absorber for the scattered light, which may find application in low-angle dependent structural color display via ink formulation.

Further, dual enhancement in fluorescence intensity was demonstrated by the compiled effect of PBG of PS CPC and host-guest chemistry. Most of the existing strategies for PC enhanced fluorescence focus on the fabrication of complex CPC architectures such as heterostructure, dual-heterostructure, and multiple-hetero structure CPCs. We combined the effect of two independent fluorescence enhancement strategies, which is very simple. PS CPCs with three different structural colors (violet, green, and orange) and a macrocyclic host molecule, cucurbit[7]uril (CB7), were selected for enhancing the fluorescence signal of a model dye, rhodamine B (RhB). The combined effects of the macrocyclic host, CB7, and the highly ordered structure of the CPCs significantly contribute to achieving over 150-fold fluorescence enhancement of

RhB. Slow photons near the PBGs of the PS CPCs facilitate enhanced light-matter interaction, while CB7 helps to prevent aggregation-induced self-quenching of RhB.

Finally, an aptasensor based on stimuli-responsive photonic crystals (RPC-A) of core-shell (CS) microspheres is developed and demonstrated the selective detection of a model pesticide. Highly monodispersed core-shell microspheres of polystyrene@poly(methyl methacrylate-ethylene glycol dimethacrylate-acrylic acid) were synthesized, and RPCs were fabricated using vertical deposition method. The RPCs consist of CS microspheres embedded in PVA matrix, which was more stable than conventional hydrogel-based RPCs of inverse opal PC, microgel based PC, polymerized crystalline colloidal array, etc. Omethoate selective DNA-aptamer sequence was selected as the recognition probe and covalently attached to poly(MMA-EGDMA-AA) hydrogel shell via EDC-NHS chemistry. The specific binding of omethoate with single-stranded DNA along with the conformational changes of the aptamer cause shrinkage of poly(MMA-EGDMA-AA) hydrogel shell and the corresponding shift in Bragg diffraction peaks can be used for the detection of a wide concentration range of omethoate.

Chapter 1

Introduction

1.1. Structural colors

Structural color is a type of non-pigmentary coloration which involves the interaction of light with specific material architectures or geometric structures with spatial variations at the micro or nano length scale, and which is originated by thin-film interference, multiple interferences, diffraction gratings, photonic crystals, etc.¹ Whereas the other two common types of colors, pigments and dyes show color due to the exchange of energy between light and electron, where electrons are excited to higher energy levels. However, structural color is due to fundamental optical processes such as reflection, refraction, interference, diffraction, scattering, etc.¹ Color of the sky, bright color of many animals (e.g. wings of butterfly, barbules of peacock tail feather, etc.), and iridescent color of soap bubbles are some of the typical examples for structural color. Butterfly, beetle and peacock are the most studied biological objects to disclose the mystery of structural coloration mechanism (fig. 1.1).² Structural color can be classified into iridescent (angle-dependent structural color) or non-iridescent color (angle-independent structural color), where the former is changed with respect to the viewing angle and latter remains identical regardless of viewing angle. For example, iridescent color can be produced by interference or diffraction, whereas non-iridescent structural color can be seen by light scattering.¹ Considering the physical mechanisms of structural coloration, both interference and diffraction can give rise to angle-dependent structural colors by regularly arranged micro or nano structure, and some forms of scattering can give rise to angle-independent structural color by irregularity of the micro or nano structure.¹ Unlike, relatively toxic pigmentary colorations, structural color is bright and resistant to photobleaching.

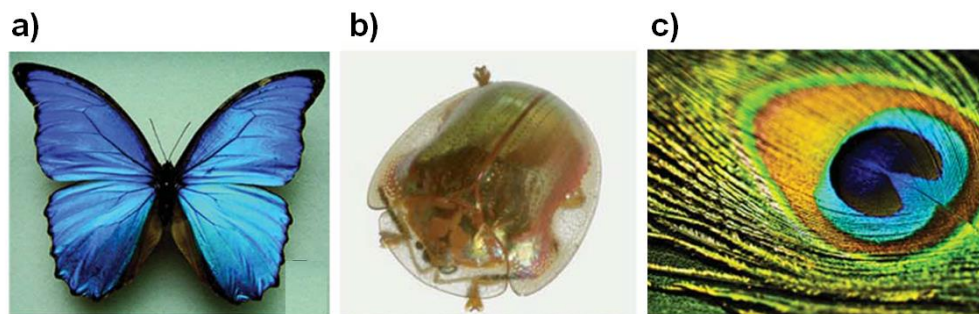


Fig. 1.1. Structural color seen in a) butterfly² b) beetle⁵ and c) peacock.²

1.2. History of remarkable studies on structural color

Till 17th century, it was believed that the coloration in a material is only due to the chemical coloration like that of dyes and pigments. Later by the development of new theories and modern instruments, it was proved that apart from chemical coloration, there are various other mechanisms of coloration in nature, and structural coloration is being the most interesting. The oldest scientific explanation of structural color was written by Hooke in his book, "*Micrographia*", which was published in 1665.³ His studies revealed that the color of peacock's feathers was not due to pigment. He further explained that the presence of marvelous structure is due to the alternate layer of solid material and air is the leading cause of color of peacock's feathers. In an interesting study, he observed that the brilliant structural color of peacock feather was destroyed by a drop of water. In 1704, Newton explained in his book "*Opticks*" that colors of the peacock feathers arose from the thinness of the transparent part.⁴ Later, the development of electromagnetic theory by Maxwell in 1873 and the experimental study of electromagnetic waves by Hertz in 1884 helped to understand the structural coloration mechanism details.¹ However, there was a debate between two hypotheses, one of which was based on pigmentary coloration. Structural colors in nature have fascinated scientists for many years; however, the correct explanation of coloration mechanism was done only after the development of scanning electron microscope (SEM) in 1940.² This discovery has triggered a new thought on the explanation and understanding of the structural coloration found in nature. Lord Rayleigh sought the help of electromagnetic theory, and he explained that the angle-dependent color is not possible by ordinary coloration mechanism of dyes, but achievable by geometric structure.¹ The development of the electron microscope helped Frank and Ruska to explain the mechanism behind the blue coloration of the feathers of ivory-breasted pitta.¹ The fascinating structural color of opals was a great mystery until C. V. Raman and Jayaraman in 1953 gave the correct explanation for it.⁵ They explained that the periodically varying refractive index due to the regular array of silica particles gives the magnificent colors to opal, and later, Sanders proved it with electron microscopy.⁶ This knowledge helped in the development of colloid based PC as an important candidate for

structural color materials. Till now the structural color was a hot subject, and intense research was already performed to unlock the coloration mechanism of many living and non-living objects.

1.3. Structural color from photonic crystals (PCs) material and the existence of photonic band gap (PBG) in PCs

Photonic Crystals (PCs) are a special class of materials that exhibit brilliant structural color due to Bragg diffraction from the periodic architecture and can mould the flow of light. In detail, a typical PC consists of periodic arrangement of dielectric material, which induces periodic modulation of the refractive index. Even though the repeating units are colorless, their periodic organization imparts coloration to PC. The fundamental optical process in the coloration mechanism of a typical PC is diffraction on the length scale of the wavelength of the incident light. The diffraction of incident light by the periodic arrangement in PC architecture provides a range of electromagnetic waves which is prohibited from propagating through it and thus, it is diffracted (fig. 1.2a).^{7, 8} This region of electromagnetic waves, namely Photonic Band Gap (PBG) provides a potential platform for controlling the propagation of light. Due to the presence of different dielectric media and refractive index contrast, light is scattered and/or diffracted at PBG, where interference of the scattered waves is destructive in all directions. The main advantage due to the existence of PBG is structural coloration. For example, fig. 1.2b shows the blue coloration of a bird due to the existence of PBG at blue wavelength.

Analog to semiconductor where the flow of electron is controlled, PCs affect the flow of photon. Like the electronic band gap in semiconductor, PBG is the main attractive characteristic property of PCs which makes the optical properties unique and fascinating and can be used to control the flow of light. The position of PBG is determined by the length scale of the structure.⁷ In the case of X-ray diffraction, X-rays are diffracted from atomic or ionic crystal, where the size of the constituent particles (atoms or ions) is of the order of the wavelength of light. In the case of PC, for obtaining diffraction in the visible region, the size of the constituent particles or building block must be of the order

of the wavelength of visible light. The wavelength region at PBG cannot be propagated through a PC. The width of the PBG is directly proportional to the refractive index contrast. PBG can be classified into complete PBG (or full PBG) and incomplete PBG (pseudo-PBG). A complete PBG is obtained when the light cannot propagate in all directions, whereas, incomplete PBG is the one in which light cannot propagate in only some direction. Refractive index contrast and lattice topography determine the type of PBG.⁵

The wavelength-dependent PBG or structural color in a typical PC can be described by a modified Bragg equation^{2,9,15} given below. The Bragg equation is modified to accommodate Snell's law for the refraction of light. Unlike in X-ray diffraction, in the context of PC, refractive index contrast is not negligible.

$$\lambda_{max} = 2d_{(111)}(n_{eff}^2 - \sin^2\theta)^{1/2}$$

Where, λ_{max} denotes the wavelength maxima of PBG, $d_{(111)}$ is the interplanar distance between adjacent crystallographic planes, and n_{eff} is the effective refractive index of the structure.

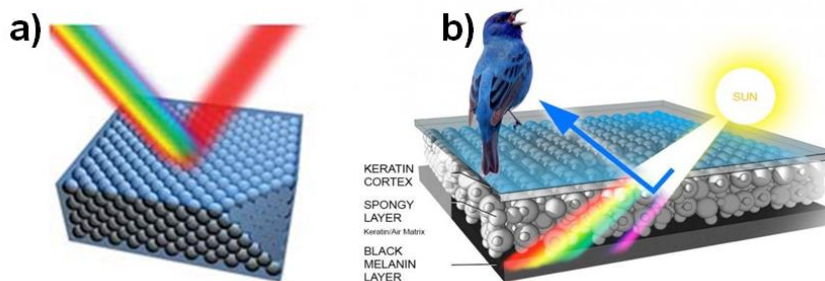


Fig. 1.2. a) Schematic of diffraction of incident light wavelength in a typical PC at PBG and b) Blue coloration of a bird due to the existence of PBG at blue color.⁸

1.4. Classification of PCs

According to the periodicity of geometric structure or based on the direction of the modulation of the refractive index, PCs can be one dimensional (1D), two dimensional (2D), and three dimensional (3D) PCs (fig. 1.3).¹⁰ 1D PC has periodic arrangement only in a direction; thus, we obtain the color only through a line of vision.

2D PC has a periodic arrangement in two directions. In 3D PCs, periodicity of the structure is maintained along with all the three directions, and PBG appears in all directions. Unlike the 1D and 2D ones, 3D PCs can reflect light incident from any direction.

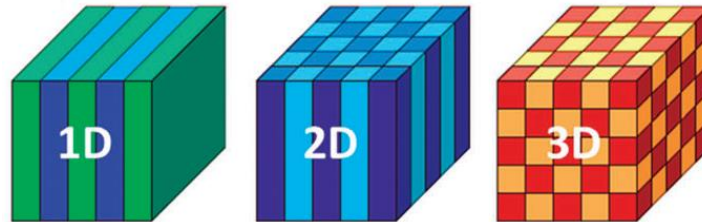


Fig. 1.3. Classification of PC according to crystal arrangement.¹⁰

1.5. PCs found in nature

The brilliant structural colors from the PC architecture found in both living and non-living objects give beauty to our colorful world. Many natural creatures consist of PC architecture and they may be 1D, 2D, or 3D PCs.¹¹ Some flowers, insects, birds, fishes, leaves, berries, and algae (fig.1.4a–c) have 1D PC or 1D grating.¹¹ Some insects, such as moth and some butterflies, consists of structures like 2D gratings. These structures help in antireflection, self-cleaning, and increases the efficiency of vision (fig. 1.4d).¹¹ Besides, 2D gratings can be found in some worms (fig. 1.4e),¹¹ and they consist of close-packed arrangement of hollow cylinders. 3D PC is seen in some beetle (*Pachyrhynchus argus*), and the structural color is visible from any direction of the beetle (fig. 1.4f).¹¹ 3D PC with inverse opal structure can be seen in some butterflies (fig. 1.4g) which comprised of a periodic arrangement of air-filled voids within a network of the interconnecting cuticle.¹¹ These structures show structural color in wide viewing angle. Opal, the most beautiful gemstone is a typical example of a natural PC (fig. 1.4h). Scientifically, opal is a mineraloid known as $\text{SiO}_2 \cdot n\text{H}_2\text{O}$ (hydrated silicon dioxide). John Sanders et al. characterized the arrangement of silica spheres of opal structures, and which provide iridescent colors.⁶ The coloration found in opal is due to its microstructure, where a well-ordered, close-packed 3D array of silica spheres (SEM image in fig. 1.4i), embedded in a

silica-based matrix that has a slightly different refractive index from that of the spheres.¹² The light incident on opals is diffracted in different directions, giving angle-dependant structural color. The color of opal can range from colorless, white, light grey to dark grey, black and all the colors of the spectrum in visible light. A greater understanding of the structure and optical properties of PCs found in the biological world trigger the research to develop bio-inspired material with bright structural colors.

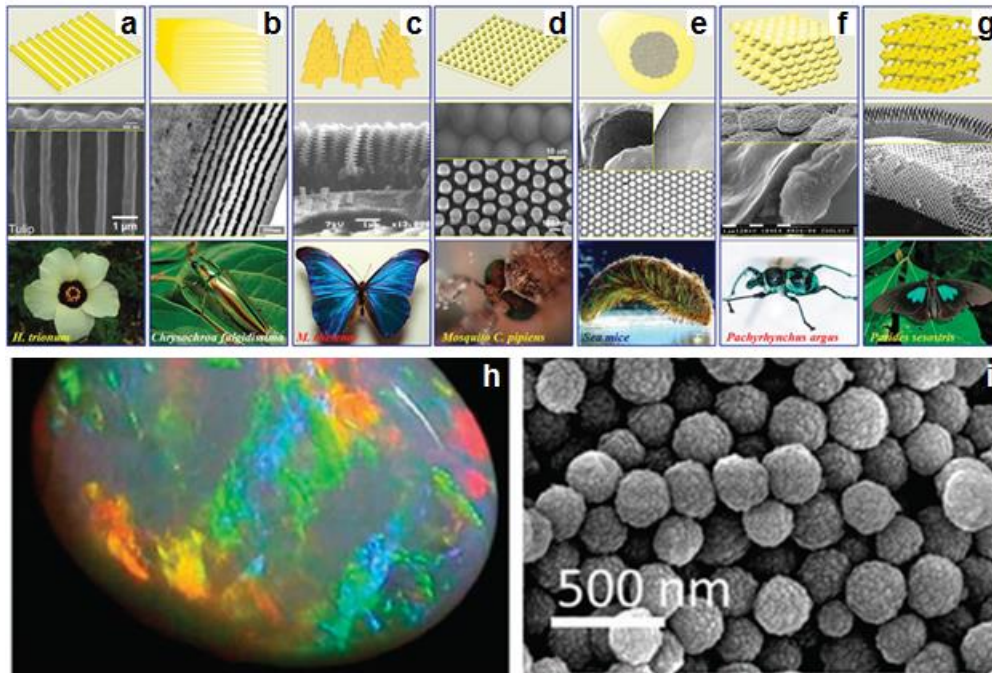


Fig. 1.4. a-g) Schematic, morphology of microstructure and photographs of structural color found in some well-studied natural creatures¹¹, h and i) photograph and SEM image of an opal stone.¹²

1.5.1. Color changing stimuli-responsive PCs found in nature

In nature, there exist PCs with special periodic structural features and structural color in them can change in response to external stimuli from the surrounding environment. *Paracheirodon innesi*, paradise whiptail, blue damselfish, tortoise beetle, hercules beetle, etc.¹¹ are some of the examples. In these natural creatures, external stimuli cause changes in lattice spacing, shifting the diffracted waves toward blue or red. For instance, *Paracheirodon innesi* changes color from blue to yellow under stressful

conditions.¹¹ The skin of this fish consists of periodically arranged biomaterials in the skin cell, which undergo alteration with change in lattice spacing by swelling of skin cell (fig. 1.5.a). In another case, tortoise beetle and hercules beetle change their colors rapidly in response to external stresses.¹¹ The thickness and the average refractive index of their thin skin film are changed by changes in the water content in the cuticle (fig. 1.5.b).

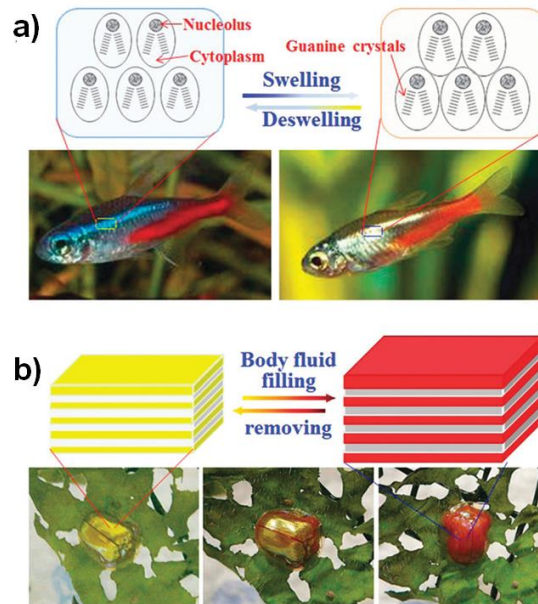


Fig. 1.5. a) Stimuli-responsive color change in *Paracheirodon innesi* by swelling induced alteration in lattice spacing and b) Stimuli-responsive color change in a beetle by refractive index variation.¹¹

Chameleons are well-studied stimuli-responsive natural PCs, and they show variable structural color during social interaction. Teyssier et al. studied the dynamic color change of panther chameleons. They showed that the variations in the spacing of guanine nanocrystals within a superficial thick layer of dermal iridophores facilitate the stimuli-responsive behavior.¹³ Fig. 1.6a and b show the reversible color change of a male chameleon during the relaxed and excited state, the corresponding TEM images in fig. 1.6c and d validate the stimuli-responsive behavior by active tuning in the lattice spacing. These stimuli-responsive PCs offer new ideas and methods for the development of bio-inspired variable structural colored materials.



Fig. 1.6. a), b) Photograph of reversible color change of a male chameleon during relaxed and excited state, c) and d) corresponding TEM images showing the changes in lattice spacing.¹³

1.6. Fabrication of PCs

Research and the development of bio-inspired PCs were initiated by Yablonovitch in 1987, who fabricated the first artificial PC called Yablonovite.¹⁴ This was a 3D PC with inverse cylindrical holes arranged in a diamond lattice. Afterward, many fabrication methods were developed, including both top-down and bottom-up approaches.¹⁵ In the top-down approach, materials with a larger size are converted into structures with smaller length scale, whereas, in the bottom-up approach, fabrication processes start at the molecular level to assemble into larger structures. In top-down approaches, microfabrication methods are commonly used.¹⁵ They include photolithography, etching techniques, holographic lithography, and glancing-angle “spiral” deposition. In the bottom-up approach, colloidal self-assembly is commonly employed.¹⁵ Compared to lithographic technique, colloidal self-assembly method is easy and economical.¹⁵

For the entire thesis work, the colloidal self-assembly method was employed for the fabrication of PCs which will be discussed in detail in the next section.

1.7. Colloidal self-assembly and colloidal PC

In colloidal self-assembly, colloidal suspension is used for the fabrication of PCs on solid substrate, and the PCs so obtained is called colloidal PCs (CPCs). A colloidal suspension consists of a dispersion medium and a dispersed phase. In colloidal self-assembly, a colloidal suspension of solid dispersed in a liquid (water) is used. In this scenario, the size of the colloidal particle range from several nanometers to

micrometers. The colloidal particles are arranged into an ordered structure with the least effort and costs, and which help to mimic the marvelous ordered micro or nano-material architecture found in living organisms such as, butterfly, beetle, fish, chameleon, etc. It is a 'bottom-up' approach for PC fabrication, where smaller particles are arranged into structures of a larger length scale. Colloidal particles are synthesized from smaller molecules (bottom-up approach). In colloidal self-assembly, colloidal particles having uniform size (highly monodispersed) and shape offers structures with highly ordered lattices, called colloidal crystals (CCs). However, the degree of ordering in the arrangement of colloidal particles can be tuned to obtain both short-range ordered structure (colloidal glass or colloidal amorphous array) and long-range ordered structure (CC) (fig. 1.7).¹⁶ The particle size domain falls on the order of wavelength of visible light, and the self-assembled structure so obtained by colloidal self-assembly is called colloidal PC (CPC), which exhibits structural color due to periodic arrangement. The arrangement of particles provides a platform to interact with light for coloration. The structural color, commonly referred to as bio-inspired structural color, shows the same unique optical characteristics of a typical PC.

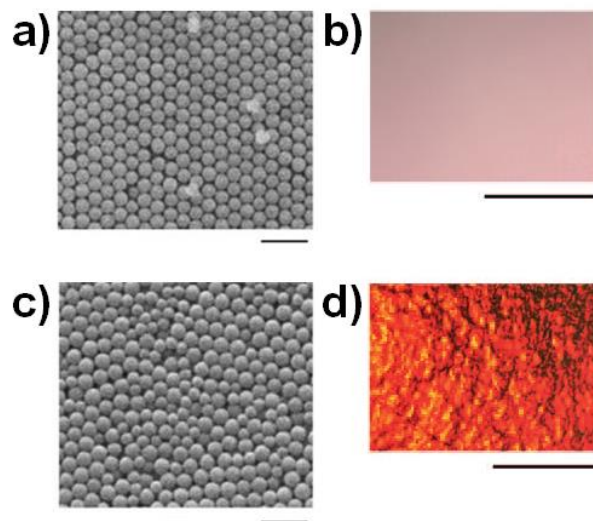


Fig. 1.7. SEM images of a) CC, c) colloidal amorphous array of silica particles, b) and d) represent corresponding digital photographs showing the structural color. The scale bar is 1 μm and 1 mm for SEM images and digital photographs, respectively.¹⁶

1.7.1. Building blocks in colloidal self-assembly

An aqua-based or organic-solvent-based colloid having nano/micro particles capable of moving with respect to each other is used in colloidal self-assembly. Colloidal particles of various shape and uniform size (large or small) are employed as a building block of colloidal self-assembly. Fig. 1.8 represents a colloidal particle of various shapes used in colloidal self-assembly.¹⁷ Monodispersed spherical particles are the most often used, highly symmetric building block and can form close-packed long-range ordered hexagonal crystal packing (fcc or hcp). Similar to spherical particles, monodispersed cube form simple cubic lattice by colloidal self-assembly. Colloidal particles with specific surface functional groups provide additional functionality. Furthermore, a higher architectural complexity was achieved by using particles like patchy particles,¹⁸⁻²⁰ core-shell- and hollow capsule systems,²¹⁻²⁴ composite particles,^{25, 26} Janus like particles,²⁷⁻³⁰ stimuli-responsive particles,³¹⁻³⁴ non-spherical particles,³⁵⁻³⁷ or in defined particle clusters³⁸⁻⁴⁰ and colloidosomes.^{41, 42}

Both inorganic and polymeric microspheres are the widely used building blocks in colloidal self-assembly. These microspheres with well-defined sizes are usually synthesized using sol-gel process and emulsion polymerization method. SiO₂, polystyrene (PS) and poly(methyl methacrylate) (PMMA) microspheres are the widely used building blocks in colloidal self-assembly. For the entire thesis work, polymeric microspheres were used for CPC fabrication.

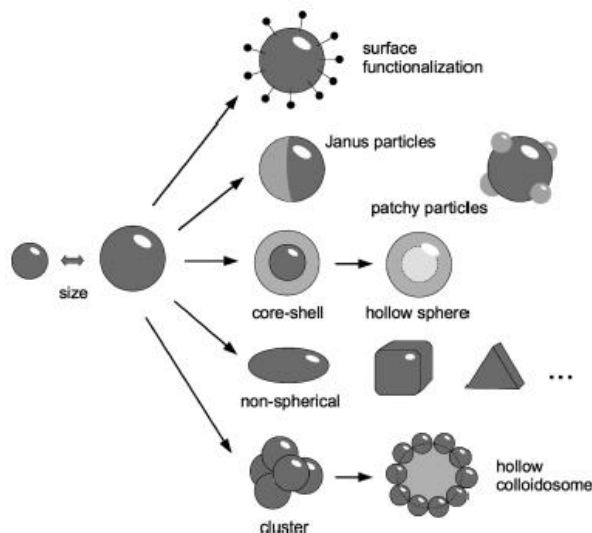


Fig. 1.8. Schematic of colloidal particles having various shapes employed in colloidal self-assembly.¹⁷

1.7.2. Forces in colloidal self-assembly

Colloidal self-assembly is a reversible process that leads to a thermodynamic minimum-energy structure. In general, the self-assembly process consists of various stages, viz. suspension, migration (towards the crystallization front), crystallization, and drying. In the colloidal self-assembly process, different types of forces act simultaneously, and colloidal self-assembly is formed when all these forces are sufficiently balanced. These forces may be internal or external. For example, repulsive and attractive forces within a colloidal particles are the internal forces. The forces acting on colloidal particles from the surrounding environment in an assembly process are the external forces. In an assembly process, there are interactions such as colloidal particle-particle, colloidal particle-substrate, and colloidal particle-solvent interactions.

1.7.2.1. Repulsive forces

At the air-water interface, the charge distribution around the particle surface is asymmetric, and the resulting dipoles arrange parallel to each other, causing repulsive forces among them (fig. 1.9a).⁴³ The same is the situation at the water-oil interface (fig. 1.9a).¹⁷ A colloid system consists of a colloidal particle with repulsive forces and which

prevents the colloid suspension from aggregation and flocculation. Repulsive forces stabilize a colloid suspension, which is due to the charge distribution around the colloidal particle, and the interaction between like charges is repulsive (fig. 1.9b).¹⁷ This electrostatic repulsion is explained in the DLVO theory.⁴⁴ The strength of the repulsive force depends on both the pH and the ionic strength of the dispersion medium.¹⁷ Additionally, there are repulsive forces among colloidal particle due to steric stabilization (fig. 1.9c).¹⁷

1.7.2.2. Attractive forces

When particles are at a solid substrate, and the thickness of liquid film becomes less than that of particle size, liquid surface undergoes deformation and the immersion capillary force (attractive) direct particle to come together (fig. 1.9d), and which is very favorable for self-assembly process to obtain close-packed structure.^{45,46} The convective flow of the dispersion medium affects the random Brownian motion and lead to hydrodynamic coupling (fig. 1.9e).¹⁷ The particles at a substrate having opposite charges interact through attractive forces (fig. 1.9f).¹⁷ Attractive forces occur among particles bridged by the dissolved polymer chain through the dispersion medium (fig. 1.9g).⁴⁷ The deformation of the meniscus at the water-air interface due to the presence of particles leads to attractive forces among them (fig. 1.9h).¹⁷ Weak Van der Waals force acts among particles and which is again attractive (fig. 1.9i).¹⁷ The depletion forces due to the presence of dissolved polymer chains or smaller nanoparticles are attractive and lead to aggregation (fig. 1.9k).⁴⁸

1.7.2.3. External forces

Particles at the surface of the dispersion medium can be directed to come together by applying external forces, as in the case of the Langmuir–Blodgett technique (fig. 1.9l).⁴⁹ The forces due to Brownian motion in a colloid are also considered as an external force (fig. 1.9m), which is driven by thermal energy (kT).^{50,51} Additionally, the gravitational force also acts on colloidal particles (fig. 1.9n).⁵²

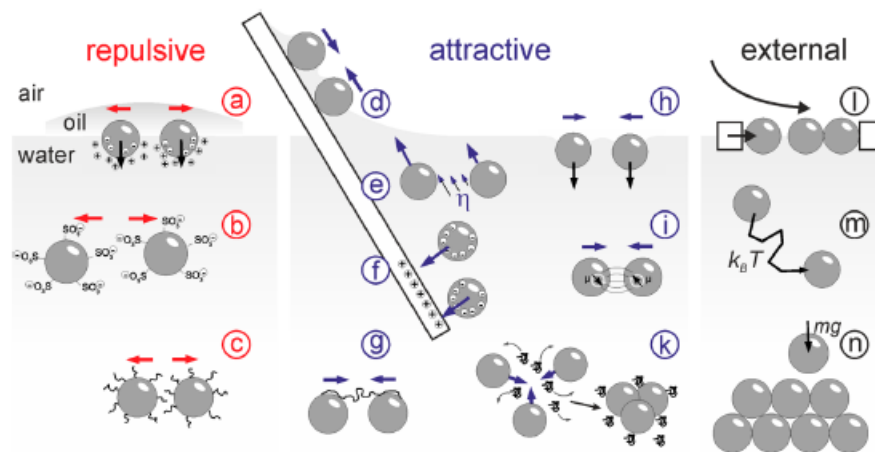


Fig. 1.9. Schematic diagram of various forces acting during colloidal self-assembly process on solid substrate.¹⁷

1.7.3. Classification and structure of colloidal crystals (CCs)

Depending on the arrangement of colloidal particles in different directions, CCs can be broadly classified into one-dimensional (1D), two-dimensional (2D) and three-dimensional (3D) CC. According to the number of types of colloidal particles present, CCs can be classified into mono, binary and polynary CCs. One dimensional CCs are 1D chain-like structure of colloids. Yang and co-workers fabricated 1D CC using the Langmuir–Blodgett (SEM image in fig. 1.10a) technique.⁵³ Two-dimensional CCs consist of a layer colloid particles (SEM image in fig. 1.10b).⁵⁴ A. Mihi *et al.* used spin-coating method for 2D CC fabrication.⁵⁵ Three-dimensional CCs consist of self-assembled structure in all three dimensions, which has a multilayer structure (SEM image in fig. 1.10c)⁵⁴, and it can be prepared using solvent evaporation method.⁵⁴ A mono-component CCs consist of only one type of particle (SEM images in fig. 1.10a-d)⁵⁴, whereas binary (SEM image in fig. 1.10e) and polynary (SEM image in fig. 1.10f) CCs consist of two⁵⁶ and more than two⁵⁷ type of particle having different particle size, respectively. These structures can be prepared using solvent evaporation methods.

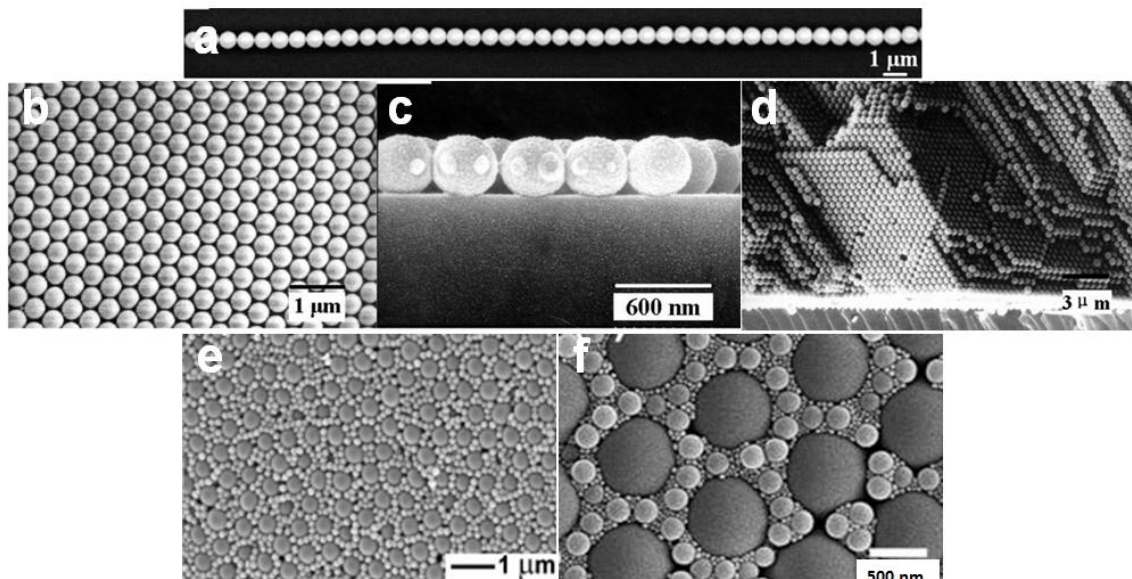


Fig. 1.10. SEM images of a) 1D⁵³ b), c) planar view and section view of 2D⁵⁴, d) 3D⁵⁴ e) binary⁵⁶ and f) polynary CCs⁵⁷.

CCs adopt different types of structures, and that depends upon the method of fabrication and the type of colloidal particles used. 2D and 3D structures of monodispersed microspheres show both hexagonal and square array pattern, and hexagonal array being thermodynamically more stable.^{58, 59} For example, a hexagonal array can be prepared using spin-coating on a planar substrate,⁵⁵ and square array can be prepared by reducing the capillary force using a surfactant.⁵⁴ In the case of binary CC, by varying the volume fraction of each colloid, different types of structure, viz. LS₁, LS₂, LS₃, etc. (L represents large spheres, S represents small spheres) can be achieved.⁶⁰⁻⁶⁵ Monodispersed colloid shows both hexagonal close packing (hcp), and face-centered cubic closed (fcc) packing, and fcc being thermodynamically more stable lattice.⁶⁶⁻⁶⁸ Apart from these structures, CC with a non-close packed structure is also possible, which can be fabricated using hydrogel-based microspheres, where the hydrogel undergoes deswelling to provide non-close-packed structure.^{58, 69, 70} Another important structural feature of CC is its porosity due to the presence of air voids. For example, the fcc structure of the monodispersed microsphere consists of 26 vol% air voids and 74 vol% of spheres. These pores are interconnected and provide room for the incorporation of functional materials into it. Due to the existence of air voids, CCs were employed as a

sacrificial template for macroporous materials fabrication. CC consists of structural defects such as cracks, grain boundaries, vacancy, and interstitial defects.⁵⁴ These defects have a remarkable role in optical properties. Just like that of semiconductor, artificially engineered defects such as point-defect, line-defect, planar-defect were introduced to tune the optical properties⁷¹⁻⁷⁴ which are useful in optical waveguides, reflectors, switches, etc. These defects are very helpful in controlling the direction of light propagation. Defects arise due to a number of reasons. Vacancy defect arise due to the non-monodisperse suspension for CC fabrication.

1.7.4. Types of colloidal self-assembly

In general, CC can be fabricated by solvent evaporation driven self-assembly, self-assembly process at the interface, directed assembly like spin coating, electric field, magnetic field, and light-driven assembly. Drop-casting of colloid suspension on a substrate, and the subsequent solvent evaporation is the most simple method of colloidal self-assembly. When the droplet is subjected to evaporation, due to the pinning of contact line on the substrate there will be solvent flux which directs the colloidal particles towards the contact line where particles are arranged to self-assembled structure (“coffee ring” effect). CCs are usually fabricated using air-liquid interface assembly, evaporation deposition, electrophoretic, sedimentation, dipping deposition and slit filling methods (fig. 1.11).⁷⁵⁻⁷⁷ In air-liquid interface assembly, colloidal particles are spontaneously moved towards the interface to minimize the energy, and self-assembled structure is formed by Van der Waals attraction combined with electrostatic or steric interaction. In evaporation deposition, the colloid suspension is subjected to evaporation, and when the thickness of the liquid film becomes less than that of particle size, capillary forces act at the triple-phase boundary, which directs the particle to come together to obtain close-packed structure. In electrophoretic deposition, self-assembly process occurs with the help of an applied electric field. While in sedimentation method, larger colloid undergoes sedimentation by the effect of gravity to obtain the self-assembled structure. In the dipping deposition method, self-assembly is formed on a substrate vertically dipped in the colloid suspension, and close-packed structures are

formed by the capillary force at the triple-phase boundary. In slit filling, the colloidal suspension is placed on a slit, and close-packed structures are formed within the slit by removing the dispersion medium. Apart from these methods, there are many other techniques such as LB technique,⁷⁸ floating packing,^{79, 80} vertical deposition,⁸¹ spin coating,^{82, 83} air-pulse-drive assembly.⁸⁴

CCs fabricated using colloidal self-assembly method consist of various structural defect such as point defects, dislocations, stacking faults, domains and cracks.⁵⁴ These defects provide interesting functional features to CCs and control its optical properties. Defects are spontaneously formed during self-assembly process. However, they can be intentionally fabricated. Defects arise due to a number of reasons. For example, vacancy defect arises due to the non-monodisperse suspension for CC fabrication. Defects are spontaneously formed due to entropic reasons. Different colloidal self-assembly method generates different types and numbers of defects. For instance, vertical deposition produces defect concentrations of about 0.01 per fcc elementary cell. At the same time, in sedimentation method, CCs are obtained with one vacancy and one Frenkel defect per 50–100 fcc elementary cells.

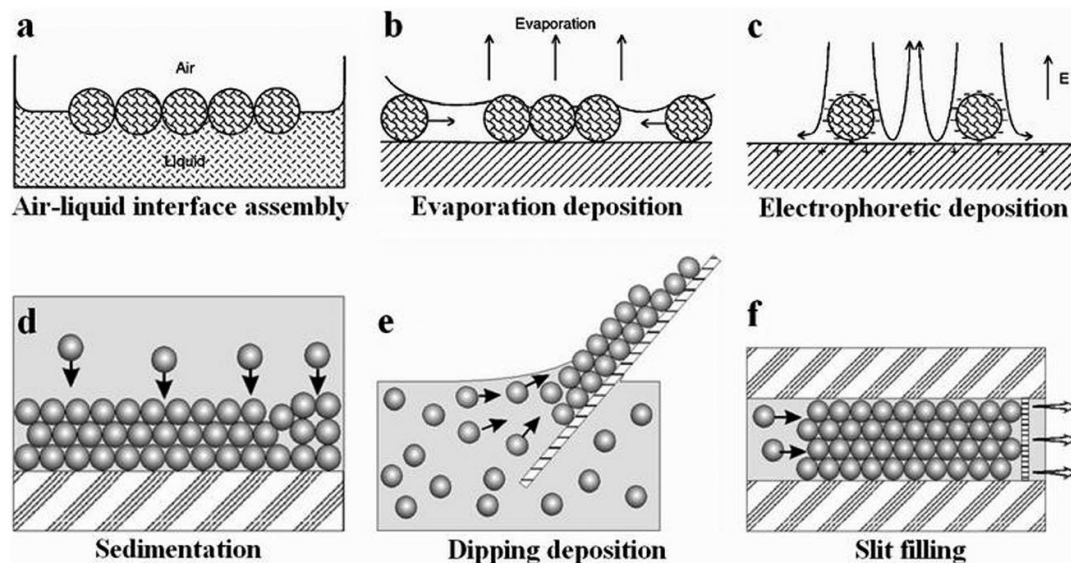


Fig. 1.11. Different types of colloidal self-assembly method (a) air–liquid interface assembly, (b) evaporation deposition, (c) electrophoretic deposition, (d) sedimentation, (e) dipping deposition, (f) slit filling.⁸⁵

1.7.5 Optical properties of CC

The arrangement of colloidal particles possess periodic changes in refractive index, since a typical CC consists of orderly arranged colloids and air voids and cause Bragg diffraction of visible light (fig. 1.12a and b). The Bragg diffraction in visible light provides structural color and PBG (fig. 1.12d).⁸⁶⁻⁸⁸ Hence the photonic structure of a CC, termed as colloidal PC (CPC), generates an optical band gap, where the electromagnetic waves are prohibited from propagating through it. In general, if the dielectric constant contrast of air voids and colloids is large, a complete photonic band gap can be obtained.⁸⁹⁻⁹¹ Usually, the CCs are fabricated using polymeric or silica microspheres, where dielectric constant contrast is low, providing only incomplete PBG.⁸⁵ The characteristics of CPC due to PBG depend on the structures, components, and incidence angles. Apart from Bragg diffraction, thin-film interference also provides coloration to CC (fig. 1.12c).⁹²

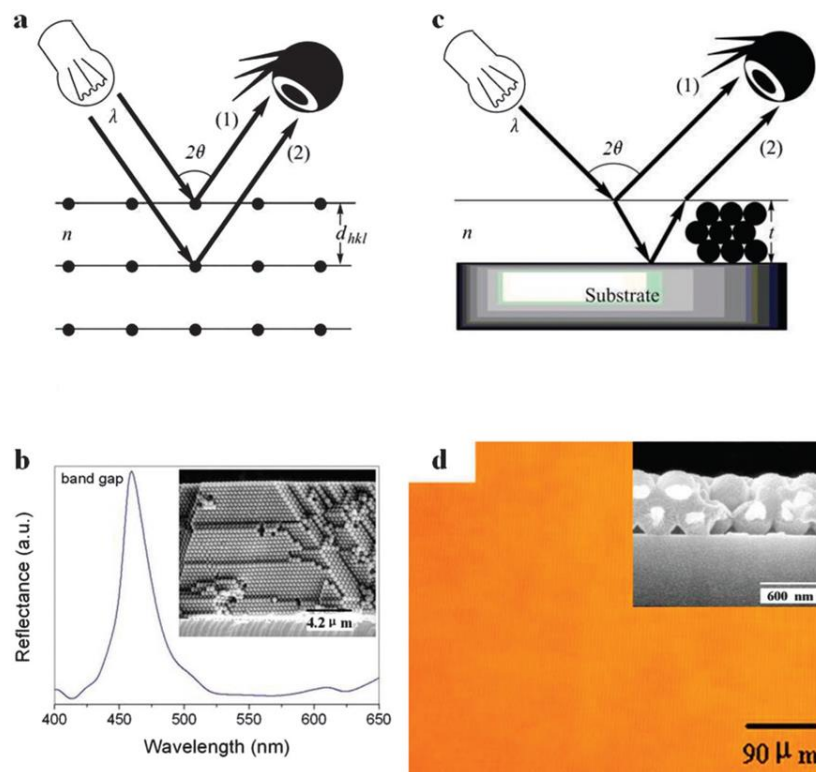


Fig. 1.12. a) Schematic diagram of Bragg diffraction b) Reflectance spectra of CC showing PBG (inset figure shows SEM image) c) schematic diagram of thin-film interference and d) structural color of CC (inset figure shows SEM image)⁹²

CC having long-range ordered structure shows angle-dependent structural color, where the structural color changes with respect to the viewing angle (fig. 1.13a).⁹³ The structure of the long-range ordered colloidal array is anisotropic; thus, it shows iridescence structural color. When the colloidal particles are short-ordered assembled, the structural color is independent of the angle⁹³ (fig. 1.13b), where Bragg diffraction is weak, and scattering is strong. The structure of the short-range ordered colloidal array is isotropic; thus, it shows non-iridescence structural color. The same scenario is observed in the case of opals, and opal can be classified as precious opal and common opal. The precious opal consists of long-range ordered silica particle, and thus it shows angle-dependent structural color.⁵ The common opal is opaque that possesses only short-range ordered silica array; thus, it lacks angle-dependent structural color.⁵

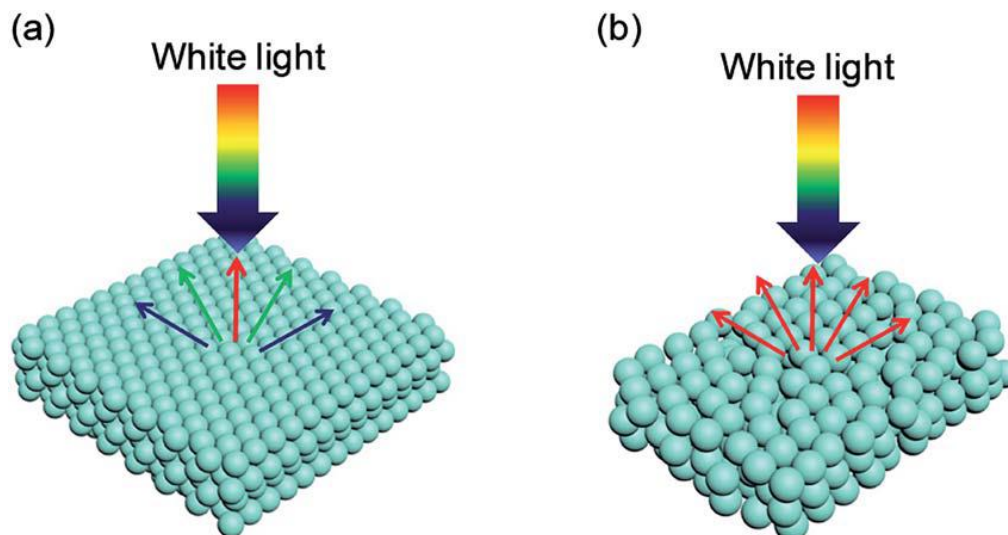


Fig. 1.13. Self-assembled colloidal structure having a) long-range ordered arrangement with angle-dependent structural color b) short-range ordered arrangement with angle-independent structural color.⁹³

1.7.6. Slow photon and PBG effect

Photons propagating with reduced group velocity are called slow photons. “The group velocity of light is the velocity at which the envelope of the light wave propagates through space.” When a PC is considered, slow photons exist at energies just above and below the PBG, more clearly at the PBG edge (fig. 1.14).⁹⁴ At the red-edge of PBG, the

electromagnetic field of slow photons are predominantly localized on the high-dielectric material (colloid particles in the case of CPC) (fig. 1.14).⁹⁵ However, at the blue-edge of PBG, the electromagnetic field of slow photons are predominantly localized on the low-dielectric material (air voids in the case of CPC) (fig. 1.14).⁹⁵ The existence of slow photons is observed in CPC, and the group velocity was measured in CCs using white-light interferometry.^{96,97} The group velocity in CPC decreases with increasing thickness up to 30 layers. It is well-known that light-matter interaction can be increased with the help of slow photons. Slow photons in CPC has been used for low threshold lasing, fluorescence enhancement, amplified photochemistry, etc.⁹⁴

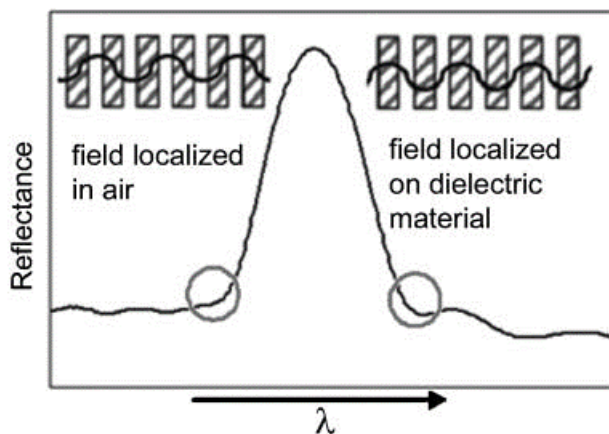


Fig. 1.14. PBG diagram of a typical PC.⁹⁸

1.7.7. Applications CPCs

1.7.7.1. CPCs as a template for macroporous inverse opal PC

CCs of monodispersed microspheres were employed as a sacrificial template for fabricating the three-dimensionally ordered macroporous materials or inverse opals. The porous materials thus obtained show the exact inverse replica of the template and which maintains the optical characteristic of the template such as Bragg diffraction and PBG. This structure shows well-ordered periodicity with interconnected pore and nano-sized walls. The template-based fabrication process consists of the infiltration of another material in the air voids of the CC followed by the subsequent removal of the template (microspheres) by chemical or thermal etching (fig. 1.15a).⁹⁹ PS and silica microsphere-

based CCs are the two commonly used templates. PS can be removed by chemical etching with solvents like xylene or thermal etching at a higher temperature, whereas silica can be removed using HF acid. The structural color of the macroporous inverse opal can be tuned by varying the diameter of the microsphere of the parent template. Till now, several types of both inorganic and polymeric macroporous inverse opal have been reported. For example, Zhang *et al.* prepared silica inverse opal using PS CPC as template (fig. 1.15b). Later, Xu *et al.* have prepared inverse opal hydrogel based on acrylic acid using silica CC as the template (fig. 1.15c).¹⁰⁰

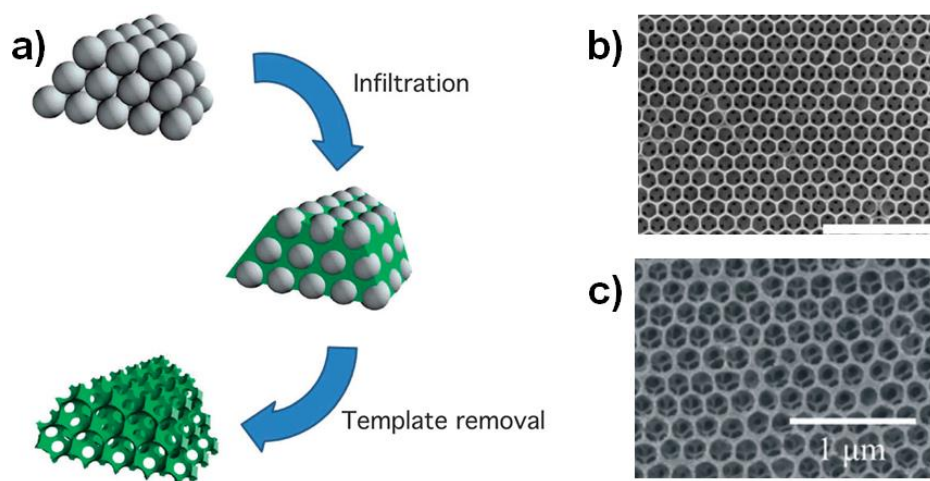


Fig. 1.15. a) Schematic diagram showing the template-based fabrication process of macroporous inverse opal⁹⁹ b), c) SEM images of silica inverse opal (scale bar: 2 μm)Ref and acrylic acid-based inverse opal hydrogel¹⁰⁰.

1.7.7.2. Stimuli-responsive PCs for sensing application

The development of stimuli-responsive PC offers a potential platform for both chemical sensing and biosensing. Stimuli-responsive PCs are a particular class of materials with structural color that has the ability to change their color via PBG shift. In general, PBG and hence the structural color of a PC can be altered by changing the refractive index or lattice spacing. Stimuli-responsive PCs can be created in two ways. In one approach, when a stimulus (for example solvent) is infiltrated into the voids of CC, and the resulting changes in the effective refractive index can cause PBG shift. Another

way to induce color change is by incorporating stimuli-responsive material into the PC structure. For example, hydrogels are an important candidate for stimuli-responsive polymeric material, which can undergo volume phase transition by swelling or deswelling. The schematic representation in fig. 1.16 depicts the stimuli-response of a PC by changes in lattice spacing via the swelling mechanism.¹⁰¹ Based on these considerations, several sensing platforms have been developed.

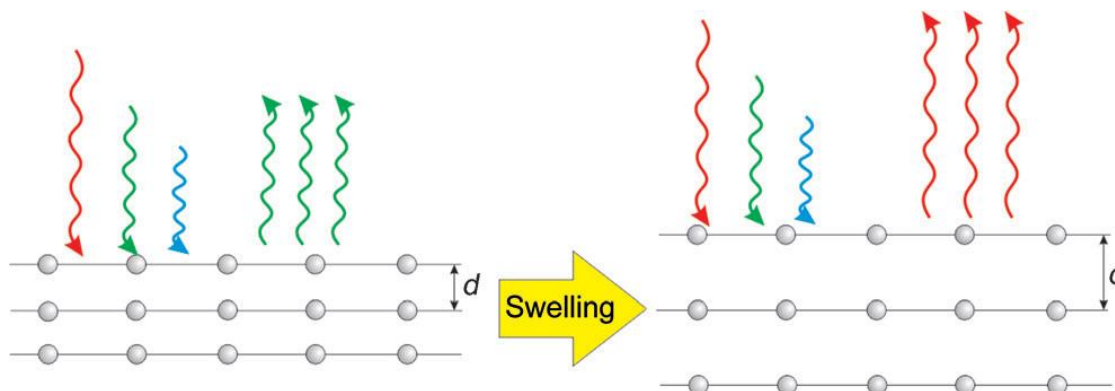


Fig. 1.16. Stimuli-response of a PC by changes in lattice spacing via swelling or deswelling mechanism.¹⁰¹

1.7.7.3. Thermoresponsive PCs

Poly (N-isopropylacrylamide) (PNIPAM) based hydrogels are the commonly used temperature responsive material to make thermoresponsive PCs. PNIPAM shows a hydrated state and a dehydrated state around its lower critical solution temperature (LCST, ca. 32 °C). Above LCST, PNIPAM expels water resulting in the shrinkage of the structure, and the corresponding shift in lattice spacing of PC can cause a color change. When the temperature is decreased, color is reversibly changed to the original color by swelling. Takeoka *et al.* fabricated a porous thermoresponsive PC gel (fig. 1.17a) using SiO₂ microspheres based CC as a template.¹⁰² They studied its temperature-responsive behavior and found that the PBG was shifted at various temperatures (fig. 1.17b). However, these structures cannot be used for high-temperature applications, where inorganic based PCs can be employed. Inorganic materials can undergo a phase

transition at high temperature, and the corresponding refractive index variations can lead to color change. These materials include Ag_2Se ,¹⁰³ BaTiO_3 ,¹⁰³ VO_2 ,¹⁰⁴ Si ,¹⁰⁵ etc.

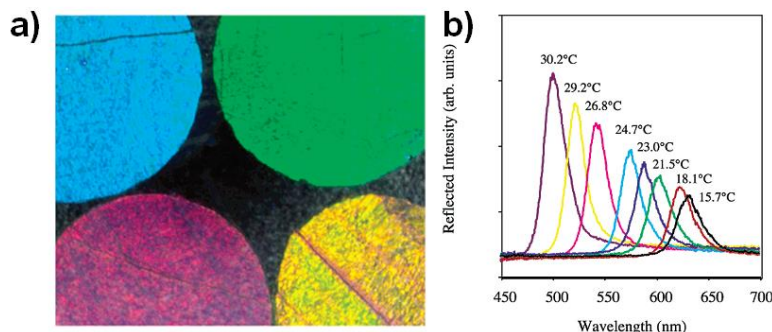


Fig. 1.17. a) Structural color of thermoresponsive PC gel b) Reflectance spectra of thermoresponsive PC gel at different temperature.¹⁰²

1.7.7.4. Mechanically responsive PCs

Mechanically responsive PC undergoes color changes under the influence of pressing, stretching, stress, compression, etc. Asher *et al.* fabricated a PC consisting of PS microsphere in N-vinylpyrrolidone/acrylamide copolymer.¹⁰⁶ When PC is subjected to stretching, the structural color showed a blue shift via a decrease in lattice spacing. Fudouzi *et al.* prepared PS CCs in poly(dimethylsiloxane) (PDMS), which showed a decrease in lattice spacing when stretched (fig. 1.18a) and which lead to a blue shift of the diffraction peak(fig. 1.18b).¹⁰⁷

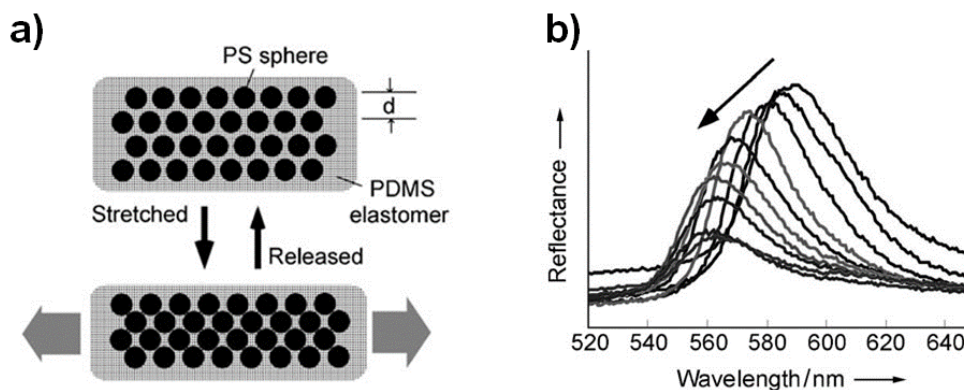


Fig. 1.18. a) Mechanism of color change of PC of PS colloid in PDMS film and b) corresponding blue shift in diffraction peak.¹⁰⁷

1.7.7.5. Optically responsive PCs

PCs having photosensitive molecules exhibit optically responsive property. Spirobenzopyran chromophore is a vital molecule that can undergo photoisomerization under the influence of UV or visible light. PC with spirobenzopyran functionalized hydrogel undergoes volume phase transition upon irradiation, which can alter the Bragg diffraction position.¹⁰⁸ Gu *et al.* utilized a spiroopyran derivative, 1,3-dihydro-1,3,3-trimethylspiro[2H-indol-2,3'-[3H]naphth[2,1-b][1,4]oxazine] as the optically responsive molecules, which showed spiroopyran and merocyanine forms (fig. 1.19) under different light condition (UV and visible light).¹⁰⁹

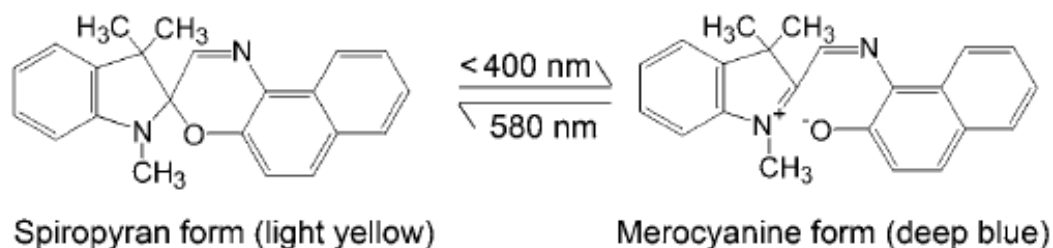


Fig. 1.19. Photoisomerization of an optically active molecule between two form under UV and visible light.¹⁰⁹

1.7.7.6. Chemically responsive PCs

Chemically responsive PC for various stimuli have already been reported, such as ions, solvent molecules, biomolecules, etc. The main advantages of these PCs are that it can be used for the label-free naked-eye detection of various chemical species. For example, Asher *et al.* used PC hydrogel for surfactant (SDS) detection where, 2D PC embedded in a poly(N-isopropylacrylamide) (PNIPAAm)-based hydrogel film was used.¹¹⁰ In the presence of surfactant, lattice spacing is increased (fig. 1.20a) which leads to red shift in the diffraction wavelength (fig. 1.20b), and the corresponding changes in structural color can be used for the visual detection of a broad concentration range of surfactant. The same principle was employed for the detection of a variety of chemical stimuli. The same group prepared a PC based on hydrogel consisting of covalently attached crown ether as a probe for detecting Pb^{2+} , Ba^{2+} , and K^{+} ions.¹¹¹⁻¹¹³ These ions

bind to the crown ether, which results in a shift in Bragg diffraction by swelling induced changes in lattice spacing. Braun *et al.* reported a pH sensitive PC based on the inverse opal PC of HEMA and AA hydrogel.¹¹⁴ At higher pH, the carboxyl group on the hydrogel network undergo ionization, which leads to changes in PBG position. There are many reports on glucose-responsive PC hydrogel, where phenylboronic acid was used as the recognition element for glucose, which leads to changes in structural color.¹¹⁵⁻¹²¹ Peng *et al.* prepared a responsive hydrogel of polyacrylamide for detecting the percentage of various alcohol in aqueous solution.¹²² Zang *et al.* used molecularly imprinted photonic polymer for the selective sensing of amino acid, where molecularly imprinting technology was employed on hydrogel network for the selective binding of amino acid.¹²³ Ye *et al.* used a photonic hydrogel for the screening of heavy metal ion where aptamer was used as the recognition probe.¹²⁴ G. Chuang *et al.* fabricated a 3D PC based on chitosan which is responsive towards various organic solvents.¹²⁵

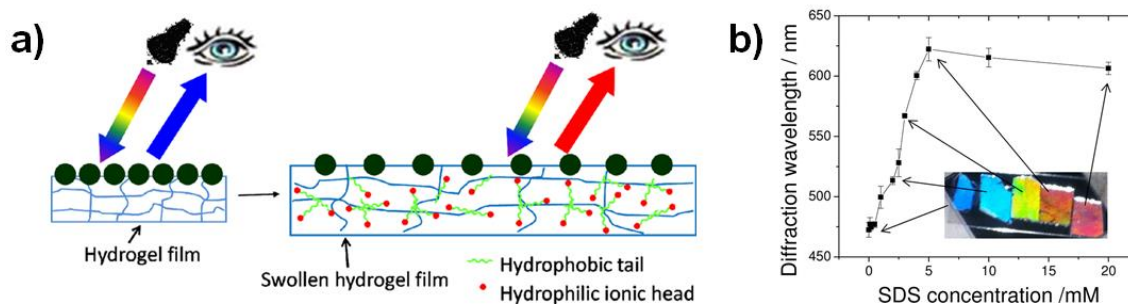


Fig. 1.20. a) Mechanism of surfactant detection via swelling induced lattice spacing change b) surfactant concentration dependent diffraction wavelength shift and corresponding changes in structural color is shown in the inset.¹¹⁰

1.7.7.7. Optical application of CPC based on PBG effect

The slow photon at the PBG edge was used for increasing the light-matter interaction and find applications in various fields such as low threshold lasers,¹²⁶ fluorescence enhancement,¹²⁷ photocatalysis,¹²⁸ etc. For example, Chen *et al.* utilized slow photon effect for the enhanced degradation of methylene blue on nanocrystalline TiO₂ inverse opals.¹²⁸ In this work, an inverse opal TiO₂ (SEM image in fig. 1.21a) was made using PS CC as a template, and the PBG of inverse opal was tuned to match the

anatase TiO₂ absorption, which promoted increased absorption and a larger population of electron-hole pairs. Among TiO₂ inverse opal having different PBG, inverse opals with the red-edge of the PBG at 370 nm only showed two-fold enhancement in dye degradation due to slow photon effect (fig. 1.21b). In another application, Guldin *et al.* coupled 3D porous PC (TiO₂ inverse opal) (fig. 1.21c and d) with dye-sensitized solar cells (DSCs) and they observed increased light-harvesting.¹²⁹ This particular architecture allowed Bragg diffraction, slow photon effect, and multiple scattering at disordered regions in the PC facilitated enhanced light harvesting. Another important application of slow photons is the fluorescent enhancement of dye molecules.¹³⁰ Slow photons at the PBG edge have been used for increasing fluorescence intensity by increased absorption and increased extraction. There are two modes of fluorescence enhancement, 1) if the excitation wavelength of dye molecules falls at the PBG edge, enhanced absorption can be achieved 2) if the emission wavelength falls at the PBG edge, increased extraction can be achieved. Eftekhari *et al.* used a double heterostructure PC (fig. 21e) made of PS microsphere for the fluorescence enhancement of a model dye (RhodamineB).¹³¹ This double-heterostructure PC consist of different PC layer having dissimilar PBG (E layer, F layer). This system has the advantage that PBG of all the PC layer can be tuned to match PBG edge with both excitation and emission wavelength. Compared to monolithic PC (E and F) and heterostructure PC (E-F and FE), double heterostructure PC (E-F-E and F-E-F) showed the highest enhancement factor (fig. 1.21f). This structure was used for increasing the detection limit of fluorescence-based sensing platforms.

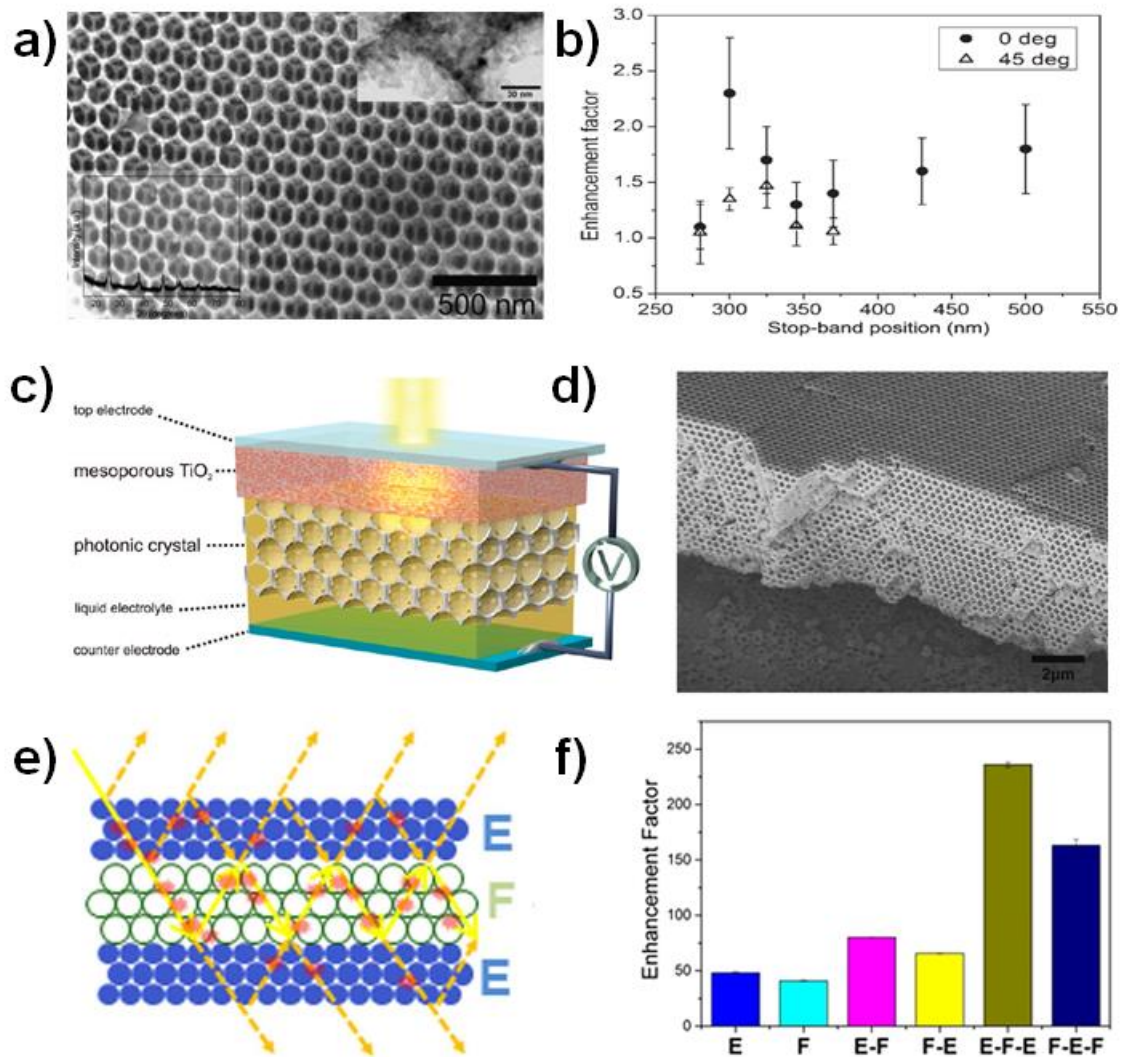


Fig. 1.21. a) SEM images and powder X-ray diffraction pattern of the nanocrystalline TiO₂ inverse opal b) enhancement factor of photocatalytic degradation of methylene blue on TiO₂ inverse opal with different PBG at 0° and 45° normal to the films¹²⁸, c) Schematic diagram of a DSC coupled with PC structure d) SEM image of inverse opal TiO₂¹²⁹, e) Schematic of a double heterostructure PC f) Enhancement factor of Rhodamine B on E, F, E-F, F-E, E-F-E and F-E-F PCs.¹³¹

1.7.7.8. Anticounterfeiting

Recently, CPCs are demonstrated to transfer high-security anticounterfeiting features on various surfaces, by various printing technology, and inkjet printing is the most commonly used printing method. The distinct pattern of PC can be made into

various substrates such as paper and polymer and is very difficult for counterfeiting. The angle-dependent structural color of CPCs offers sophisticated security features. As the coloration is due to structure, their bright color lasts for a long time. Hou *et al.* developed a QR code by inkjet printing, which consists of four security features such as three different shaped PC (bump, plate, and coffee ring) and fluorescence (fig. 1.22).¹³² They were able to show four security patterns under different lighting conditions (fig. 1.22).

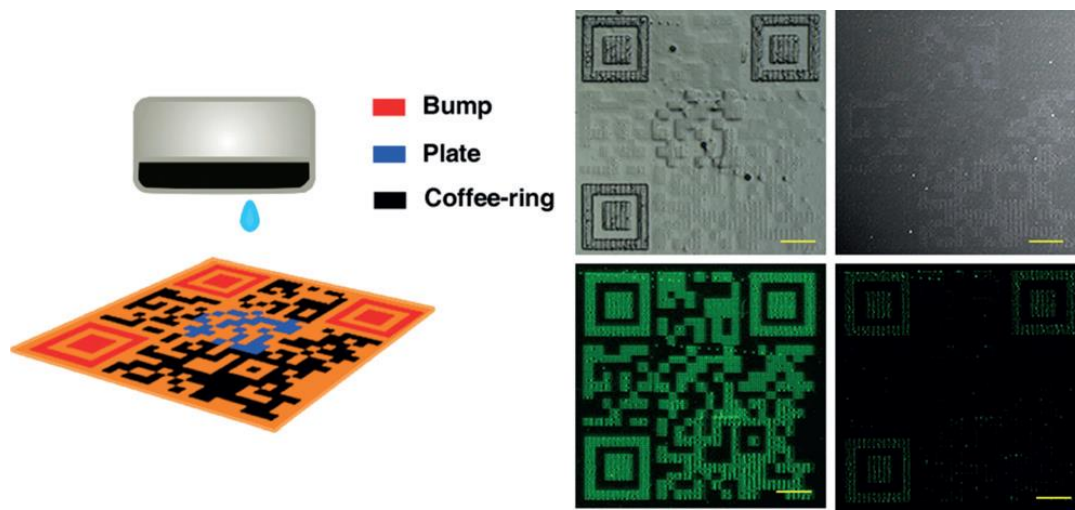


Fig. 1.22. Inkjet printed QR code consisting of bumps, plates, and coffee-rings shaped PC dots which show four images under different lighting condition.¹³²

In this context, stimuli-responsive PCs offer a potential platform, since pattern can be seen only under the influence of external stimuli. Shape memory polymers are one class of stimuli-responsive material and can be employed as a PC for security feature fabrication. For example, Fang *et al.* developed a porous PC based on shape memory polymer, which showed different colors in acetone as well as in the absence of acetone (fig. 1.23a).¹³³ In a different approach, various images with angle-dependent structural color-changing behavior are employed. For example, Lee *et al.* reported patterns with CPC, which changed its color at various viewing angles (fig. 1.23b).¹³⁴ In another approach, the inverse opal PC was used for making complicated patterns, which also changed its structural color with respect to the viewing angle (fig. 1.23c).¹³⁵ In recent report, a monolayer of CPCs was developed by inkjet printing, which shows no structural

color in daylight, but shows color in flashlight (fig. 1.23d), and they also demonstrated its application potential in some of the products.¹³⁶

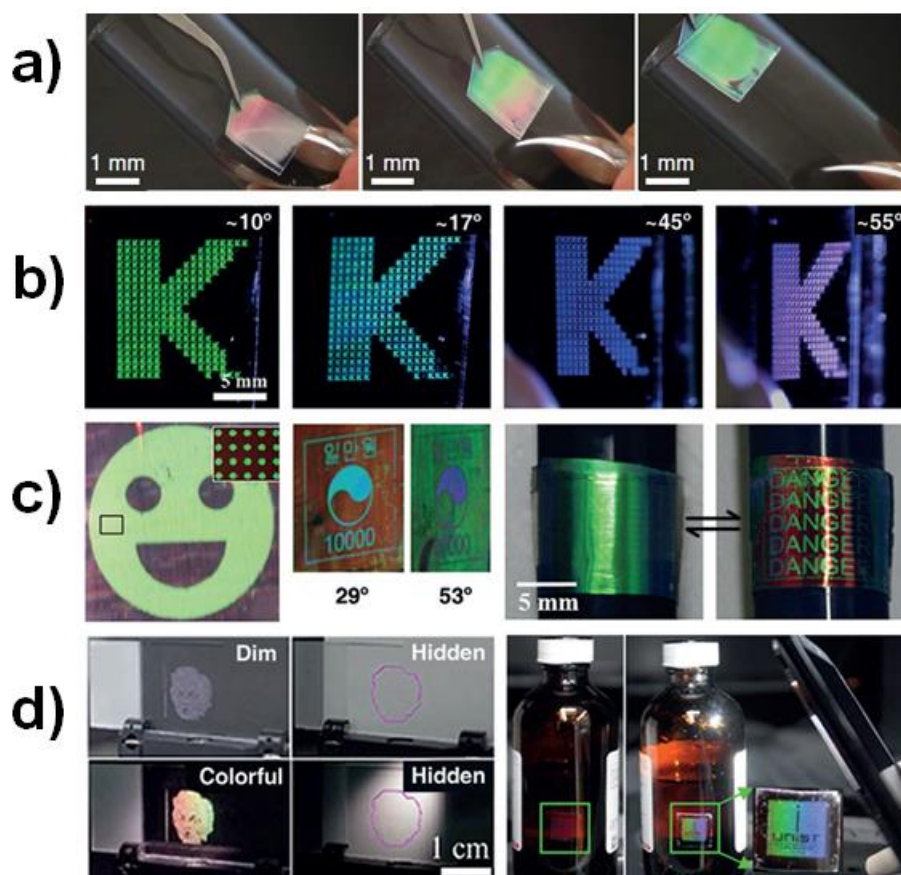


Fig. 1.23. a) PC based on shape memory polymer showing solvent responsive color change¹³³, b) angle-dependent color changing PC pattern¹³⁴, c) angle-dependent color changing inverse opal PC pattern¹³⁵ and d) inkjet-printed PC pattern showing colored and colorless appearance under different lighting condition.¹³⁶

1.7.7.9. Display

Due to its bright structural color, PC can be employed for display applications. For example, Ozin *et al.* developed an electrically responsive PC for display application, and that changed the structural color towards different voltage condition.¹³⁷ They fabricated an inverse polymer-gel PC using silica-based CC as a template which was removed by chemical etching using HF acid. (fig. 1.24a). Inverse polymer-gel PC consists

of polyferrocenylsilane (PFS) derivatives polyferrocenylmethylvinylsilane (PFMVS) and polyferrocenyldivinylsilane (PFDVS). This film was able to stay as a free-standing film, which was collected onto indium tin oxide (ITO)-coated glass for observing the electrically responsive color shifting. The color display consists of a button cell (fig. 1.24b), which contains inverse polymer-gel opal, ITO glass (working electrode), ITO-glass or FTO-glass (counter electrode), hotmelt ionomer spacer, and a liquid. The color change towards the applied electrical potential is based on swelling of the polymer, which changes the lattice spacing leading to shifting in Bragg diffraction wavelength (fig.1.24c).

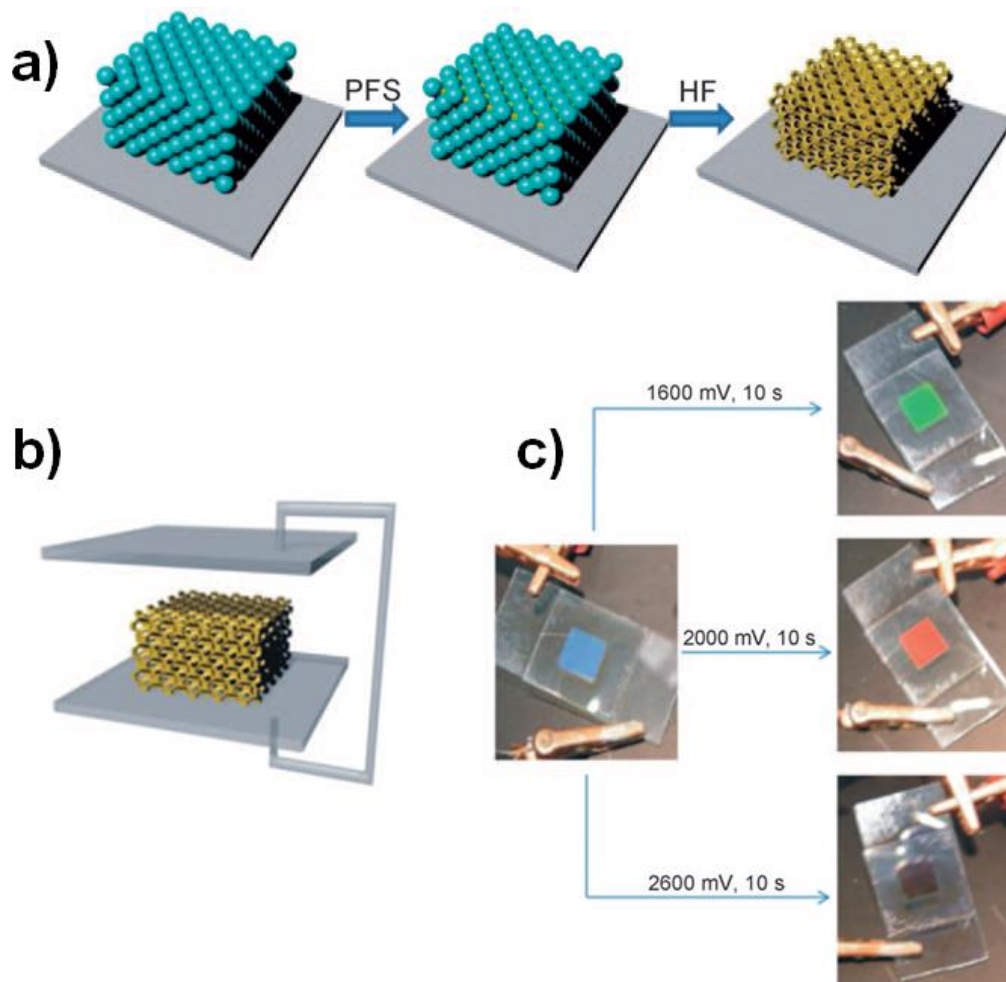


Fig. 1.24. a) Schematic of fabrication of inverse opal gel b) schematic of cell structure and c) color change of PC at different voltage.¹³⁷

1.8. Objectives of the present thesis

The entire thesis work is focused on the bio-inspired structural color of colloidal photonic crystals (CPC). Among different types of fabrication methods, we adopted a vertical deposition method for CPC fabrication. However, large-area CPC with excellent optical quality requires highly monodispersed polymeric/inorganic microspheres, which require optimization of experimental parameters in synthesis. Further, parameters for solvent evaporation driven self-assembly of colloidal microspheres are optimized by fine tuning relative humidity, temperature, and evaporation time. The optical properties, such as the structural color and photonic band gap (PBG), depend upon the quality of the crystal structure of CPC. Additionally, the optical properties, such as the dependency of structural color on viewing angle, are also determined by the crystal structure of CPC.

CPCs and inverse opal PCs (IO-PCs) obtained by CPC based templating method show brilliant structural color due to Bragg diffraction. However, their powder form is white due to light scattering. Currently, existing methods utilized smaller black particles for absorbing scattered light to enhance the color intensity. However, the non-uniform distribution of these particles within the PC structure affects the periodic modulation of the refractive index in CPCs. Interestingly, the use of larger black particles can solve this problem. Particles having size larger than the air-voids in CPCs and IO-PCs could not enter the periodic structure and thus, maintain periodic modulation of the refractive index. In another application such as PC enhanced fluorescence, the currently existing methods using heterostructure CPC, dual-hetero structure CPC, and multiple-hetero structure CPC are very complicated. A dual strategy viz. photonic band gap effect and host-guest complexation could be adopted for the enhancement of a fluorescent probe by using an easily fabricated CPC. Additionally, in one of the potential applications of CPCs for making stimuli-responsive color-changing PCs (RPC), the core-shell microsphere has not been widely explored. Additionally, Aptamer- based recognition probe can offer a better platform in RPCs with its selective binding of target molecules.

The specific objectives of the present research work are to explore the bio-inspired structural color of polymer-based CPC for the development of structurally colored IO-PC powder, a method for PC enhanced fluorescence, and RPC based sensing platform. The specific objectives of the thesis are,

1. To synthesize highly monodispersed polystyrene (PS) microspheres having good colloidal stability and fabrication of long-range ordered PS CPC.
2. To regain the structural color of silica IO-PC powder using large sized charcoal flakes as the background absorber for the scattered light of powdered silica IO-PCs.
3. To demonstrate a method for fluorescence enhancement of a model dye molecule by the compiled effect of photonic band gap (PBG) and cucurbit[7]uril based host-guest complexation.
4. To prepare a stimuli-responsive photonic crystal based on core-shell microsphere with covalently bound DNA-aptamer (recognition probe) and to demonstrate its use for the selective detection of an organophosphorus pesticide (omethoate).

1.9. Layout of the thesis

The thesis is organized into five chapters, as

Chapter 1 provides an introduction to structural color and photonic crystals. Special emphasis is given to colloidal self-assembly and colloidal photonic crystals. Optical properties, fabrication methods, and applications of colloidal photonic crystals are discussed in detail.

Chapter 2 deals with the synthesis of highly monodispersed polystyrene microspheres and the fabrication of colloidal photonic crystal using the vertical deposition method. A three-dimensionally ordered macroporous silica inverse opal powder was also prepared, and charcoal flakes are used as an absorber for scattered light.

Chapter 3 demonstrates the fluorescence enhancement of a model dye by tuning the photonic band gap and host-guest complex formation. The encapsulation of a model dye (Rhodamine B) in cucurbit[7]uril host molecule increases the fluorescence intensity, and

further, for additional fluorescence enhancement, photonic band edge effect of polystyrene colloidal photonic crystals was explored.

Chapter 4 focused on the development of an aptasensor for pesticide (omethoate, a model pesticide) detection, which is based on a stimuli-responsive colloidal photonic crystal of a core-shell microsphere. An omethoate selective single-stranded DNA-aptamer was used as the recognition probe and is covalently bound to core-shell microsphere-based colloidal photonic crystal using EDC-NHS chemistry

Chapter 5 summarizes the entire thesis work highlighting the advances made in the development of colloidal photonic crystal based structurally colored materials. We also discuss the scope of future work in this area.

References

1. S. Kinoshita, S. Yoshioka and J. Miyazaki, *Reports on Progress in Physics*, 2008, **71**, 076401.
2. J. Sun, B. Bhushan and J. Tong, *RSC Advances*, 2013, **3**, 14862-14889.
3. R. Hooke, *Micrographia: some physiological descriptions of minute bodies made by magnifying glasses with observations and inquiries thereupon*, Good Press, 2019.
4. I. Newton, *Opticks, or, a treatise of the reflections, refractions, inflections & colours of light*, Courier Corporation, 1952.
5. Y. Takeoka, *Journal of Materials Chemistry C*, 2013, **1**, 6059-6074.
6. P. Darragh, A. Gaskin, B. Terrell and J. Sanders, *Nature*, 1966, **209**, 13-16.
7. L. Gonzalez-Urbina, K. Baert, B. Kolaric, J. Perez-Moreno and K. Clays, *Chemical reviews*, 2011, **112**, 2268-2285.
8. S.-H. Kim, S. Y. Lee, S.-M. Yang and G.-R. Yi, *NPG Asia Materials*, 2011, **3**, 25-33.
9. V. V. Vipin, P. R. Chandran, A. M. Ramachandran, A. P. Mohamed and S. Pillai, *New Journal of Chemistry*, 2019, **43**, 16264-16272.
10. E. Armstrong and C. O'Dwyer, *Journal of Materials Chemistry C*, 2015, **3**, 6109-6143.

11. Y. Zhao, Z. Xie, H. Gu, C. Zhu and Z. Gu, *Chemical Society Reviews*, 2012, **41**, 3297-3317.
12. E. s. Gaillou, E. Fritsch, B. Aguilar-Reyes, B. Rondeau, J. Post, A. Barreau and M. Ostroumov, *American Mineralogist*, 2008, **93**, 1865-1873.
13. J. Teyssier, S. V. Saenko, D. Van Der Marel and M. C. Milinkovitch, *Nature communications*, 2015, **6**, 6368.
14. E. Yablonovitch, *Physical Review Letters*, 1987, **58**, 2059-2062.
15. J. Ge and Y. Yin, *Angewandte Chemie International Edition*, 2011, **50**, 1492-1522.
16. M. Harun-Ur-Rashid, A. Bin Imran, T. Seki, M. Ishii, H. Nakamura and Y. Takeoka, *ChemPhysChem*, 2010, **11**, 579-583.
17. N. Vogel, M. Retsch, C.-A. Fustin, A. del Campo and U. Jonas, *Chemical reviews*, 2015, **115**, 6265-6311.
18. G.-R. Yi, D. J. Pine and S. Sacanna, *Journal of Physics: Condensed Matter*, 2013, **25**, 193101.
19. H. Bao, T. Bihr, A.-S. Smith and R. N. K. Taylor, *Nanoscale*, 2014, **6**, 3954-3966.
20. H. Bao, W. Peukert and R. K. Taylor, *Advanced Materials*, 2011, **23**, 2644-2649.
21. T. Still, R. Sainidou, M. Retsch, U. Jonas, P. Spahn, G. Hellmann and G. Fytas, *Nano letters*, 2008, **8**, 3194-3199.
22. M. Retsch, M. Schmelzeisen, H.-J. r. Butt and E. L. Thomas, *Nano letters*, 2011, **11**, 1389-1394.
23. L. Isa, E. Amstad, K. Schwenke, E. Del Gado, P. Ilg, M. Kröger and E. Reimhult, *Soft Matter*, 2011, **7**, 7663-7675.
24. C. Graf, D. L. Vossen, A. Imhof and A. van Blaaderen, *Langmuir*, 2003, **19**, 6693-6700.
25. C. R. van den Brom, I. Anac, R. F. Roskamp, M. Retsch, U. Jonas, B. Menges and J. A. Preece, *Journal of Materials Chemistry*, 2010, **20**, 4827-4839.
26. S. Fischer, A. Salcher, A. Kornowski, H. Weller and S. Förster, *Angewandte Chemie International Edition*, 2011, **50**, 7811-7814.
27. Z. Nie, W. Li, M. Seo, S. Xu and E. Kumacheva, *Journal of the American Chemical Society*, 2006, **128**, 9408-9412.
28. A. Walther and A. H. Müller, *Soft Matter*, 2008, **4**, 663-668.

29. A. Perro, S. Reculosa, S. Ravaine, E. Bourgeat-Lami and E. Duguet, *Journal of materials chemistry*, 2005, **15**, 3745-3760.
30. A. Walther and A. H. Muller, *Chemical reviews*, 2013, **113**, 5194-5261.
31. R. Contreras-Cáceres, J. Pacifico, I. Pastoriza-Santos, J. Pérez-Juste, A. Fernández-Barbero and L. M. Liz-Marzán, *Advanced Functional Materials*, 2009, **19**, 3070-3076.
32. D. Klinger and K. Landfester, *Macromolecular rapid communications*, 2011, **32**, 1979-1985.
33. D. Klinger and K. Landfester, *Soft Matter*, 2011, **7**, 1426-1440.
34. D. Klinger and K. Landfester, *Polymer*, 2012, **53**, 5209-5231.
35. Z. Zhang, P. Pfliegerer, A. B. Schofield, C. Clasen and J. Vermant, *Journal of the American Chemical Society*, 2010, **133**, 392-395.
36. M. M. Panczyk, J.-G. Park, N. J. Wagner and E. M. Furst, *Langmuir*, 2012, **29**, 75-81.
37. C. Herrmann, A. Turshatov and D. Crespy, *ACS Macro Letters*, 2012, **1**, 907-909.
38. N. Pazos-Perez, C. S. Wagner, J. M. Romo-Herrera, L. M. Liz-Marzán, F. J. García de Abajo, A. Wittemann, A. Fery and R. A. Alvarez-Puebla, *Angewandte Chemie International Edition*, 2012, **51**, 12688-12693.
39. Y. Wang, Y. Wang, D. R. Breed, V. N. Manoharan, L. Feng, A. D. Hollingsworth, M. Weck and D. J. Pine, *Nature*, 2012, **491**, 51.
40. V. N. Manoharan, M. T. Elsesser and D. J. Pine, *Science*, 2003, **301**, 483-487.
41. A. Dinsmore, M. F. Hsu, M. Nikolaides, M. Marquez, A. Bausch and D. Weitz, *Science*, 2002, **298**, 1006-1009.
42. C. S. Wagner, A. Fortini, E. Hofmann, T. Lunkenbein, M. Schmidt and A. Wittemann, *Soft Matter*, 2012, **8**, 1928-1933.
43. P. Pieranski, *Physical Review Letters*, 1980, **45**, 569.
44. B. Deryagin and L. Landau, *J. Exp. Theor. Phys*, 1941, **11**, 802.
45. P. A. Kralchevsky and K. Nagayama, *Advances in colloid and interface science*, 2000, **85**, 145-192.
46. K. Nagayama, *Langmuir*, 1994, **10**, 23-36.

47. E. Dickinson and L. Eriksson, *Advances in Colloid and Interface Science*, 1991, **34**, 1-29.
48. P. Jenkins and M. Snowden, *Advances in colloid and interface science*, 1996, **68**, 57-96.
49. K. U. Fulda and B. Tieke, *Advanced Materials*, 1994, **6**, 288-290.
50. M. Von Smoluchowski, *Annalen der physik*, 1906, **326**, 756-780.
51. J. N. Israelachvili, *Intermolecular and surface forces*, Academic press, 2015.
52. E. Dokou, M. A. Barteau, N. J. Wagner and A. M. Lenhoff, *Journal of colloid and interface science*, 2001, **240**, 9-16.
53. A. R. Tao, J. Huang and P. Yang, *Accounts of Chemical Research*, 2008, **41**, 1662-1673.
54. H. Cong and W. Cao, *Langmuir*, 2003, **19**, 8177-8181.
55. A. Mihi, M. Ocaña and H. Míguez, *Advanced Materials*, 2006, **18**, 2244-2249.
56. R. Mukhopadhyay, O. Al-Hanbali, S. Pillai, A. G. Hemmersam, R. L. Meyer, A. C. Hunter, K. J. Rutt, F. Besenbacher, S. M. Moghimi and P. Kingshott, *Journal of the American Chemical Society*, 2007, **129**, 13390-13391.
57. G. Singh, S. Pillai, A. Arpanaei and P. Kingshott, *Soft Matter*, 2011, **7**, 3290-3294.
58. H. Cong and W. Cao, *The Journal of Physical Chemistry B*, 2005, **109**, 1695-1698.
59. J. Zhang, Y. Li, X. Zhang and B. Yang, *Advanced Materials*, 2010, **22**, 4249-4269.
60. F. Li, D. P. Josephson and A. Stein, *Angewandte Chemie International Edition*, 2011, **50**, 360-388.
61. P. Kumnorkaew and J. F. Gilchrist, *Langmuir*, 2009, **25**, 6070-6075.
62. L. Wang, Y. Wan, Y. Li, Z. Cai, H.-L. Li, X. S. Zhao and Q. Li, *Langmuir*, 2009, **25**, 6753-6759.
63. V. Kitaev and G. A. Ozin, *Advanced Materials*, 2003, **15**, 75-78.
64. A. Emoto, E. Uchida and T. Fukuda, *Colloids and Surfaces A: Physicochemical and Engineering Aspects*, 2012, **396**, 189-194.
65. N. V. Dziomkina, M. A. Hempenius and G. J. Vancso, *Colloids and Surfaces A: Physicochemical and Engineering Aspects*, 2009, **342**, 8-15.
66. B. You, N. Wen, L. Shi, L. Wu and J. Zi, *Journal of Materials Chemistry*, 2009, **19**, 3594-3597.

67. B. T. Holland, C. F. Blanford and A. Stein, *Science*, 1998, **281**, 538-540.
68. O. D. Velev, T. A. Jede, R. F. Lobo and A. M. Lenhoff, *Nature*, 1997, **389**, 447-448.
69. J. Li, S. Zhang, H. Chen, Z.-Z. Gu and Z. Lu, *Colloids and Surfaces A: Physicochemical and Engineering Aspects*, 2007, **299**, 54-57.
70. G. Zhang, D. Wang, Z.-Z. Gu, J. Hartmann and H. Möhwald, *Chemistry of Materials*, 2005, **17**, 5268-5274.
71. F. Jonsson, C. M. S. Torres, J. Seekamp, M. Schniedergers, A. Tiedemann, J. Ye and R. Zentel, *Microelectronic Engineering*, 2005, **78-79**, 429-435.
72. Q. Yan, L. K. Teh, Q. Shao, C. C. Wong and Y.-M. Chiang, *Langmuir*, 2008, **24**, 1796-1800.
73. P. Massé, S. Reculosa, K. Clays and S. Ravaine, *Chemical Physics Letters*, 2006, **422**, 251-255.
74. Q. Yan, Z. Zhou, X. S. Zhao and S. J. Chua, *Advanced Materials*, 2005, **17**, 1917-1920.
75. X. Ye and L. Qi, *Nano Today*, 2011, **6**, 608-631.
76. O. D. Velev and A. M. Lenhoff, *Current Opinion in Colloid & Interface Science*, 2000, **5**, 56-63.
77. Y. Xia, B. Gates, Y. Yin and Y. Lu, *Advanced Materials*, 2000, **12**, 693-713.
78. M. Bardosova, M. E. Pemble, I. M. Povey and R. H. Tredgold, *Advanced Materials*, 2010, **22**, 3104-3124.
79. Y. Fu, Z. Jin, G. Liu and Y. Yin, *Synthetic Metals*, 2009, **159**, 1744-1750.
80. A. Wang, S.-L. Chen and P. Dong, *Materials Letters*, 2009, **63**, 1586-1589.
81. J. Zhang, X. Luo, X. Yan and G. Zhu, *Thin Solid Films*, 2010, **518**, 5204-5208.
82. Y. G. Ko, D. H. Shin, G. S. Lee and U. S. Choi, *Colloids and Surfaces A: Physicochemical and Engineering Aspects*, 2011, **385**, 188-194.
83. P. Colson, R. Cloots and C. Henrist, *Langmuir*, 2011, **27**, 12800-12806.
84. T. Kanai, T. Sawada, A. Toyotama and K. Kitamura, *Advanced Functional Materials*, 2005, **15**, 25-29.
85. H. Cong, B. Yu, J. Tang, Z. Li and X. Liu, *Chemical Society Reviews*, 2013, **42**, 7774-7800.
86. O. Sato, S. Kubo and Z.-Z. Gu, *Accounts of Chemical Research*, 2009, **42**, 1-10.

87. Y. Zhang, J. Wang, Y. Huang, Y. Song and L. Jiang, *Journal of Materials Chemistry*, 2011, **21**, 14113-14126.
88. P. H. C. Camargo, Z.-Y. Li and Y. Xia, *Soft Matter*, 2007, **3**, 1215-1222.
89. G. von Freymann, V. Kitaev, B. V. Lotsch and G. A. Ozin, *Chemical Society Reviews*, 2013, **42**, 2528-2554.
90. J. F. Galisteo-López, M. Ibisate, R. Sapienza, L. S. Froufe-Pérez, Á. Blanco and C. López, *Advanced Materials*, 2011, **23**, 30-69.
91. Q. Yan, L. Wang and X. S. Zhao, *Advanced Functional Materials*, 2007, **17**, 3695-3706.
92. H. Cong and W. Cao, *Langmuir*, 2004, **20**, 8049-8053.
93. P. Liu, L. Bai, J. Yang, H. Gu, Q. Zhong, Z. Xie and Z. Gu, *Nanoscale Advances*, 2019, **1**, 1672-1685.
94. J. I. Chen, G. von Freymann, S. Y. Choi, V. Kitaev and G. A. Ozin, *Journal of Materials Chemistry*, 2008, **18**, 369-373.
95. R. D. Meade, A. M. Rappe, K. D. Brommer and J. D. Joannopoulos, *J. Opt. Soc. Am. B*, 1993, **10**, 328-332.
96. G. v. Freymann, S. John, S. Wong, V. Kitaev and G. A. Ozin, *Applied Physics Letters*, 2005, **86**, 053108.
97. J. F. Galisteo-López, M. Galli, M. Patrini, A. Balestreri, L. C. Andreani and C. López, *Physical Review B*, 2006, **73**, 125103.
98. S. Nishimura, N. Abrams, B. A. Lewis, L. I. Halaoui, T. E. Mallouk, K. D. Benkstein, J. van de Lagemaat and A. J. Frank, *Journal of the American Chemical Society*, 2003, **125**, 6306-6310.
99. A. Stein, B. E. Wilson and S. G. Rudisill, *Chemical Society Reviews*, 2013, **42**, 2763-2803.
100. D. Xu, W. Zhu, C. Wang, T. Tian, J. Cui, J. Li, H. Wang and G. Li, *Chemistry–A European Journal*, 2014, **20**, 16620-16625.
101. C. Fenzl, T. Hirsch and O. S. Wolfbeis, *Angewandte Chemie International Edition*, 2014, **53**, 3318-3335.
102. Y. Takeoka and M. Watanabe, *Langmuir*, 2003, **19**, 9104-9106.

103. U. Jeong and Y. Xia, *Angewandte Chemie International Edition*, 2005, **44**, 3099-3103.
104. A. Pevtsov, D. Kurdyukov, V. Golubev, A. Akimov, A. Meluchev, A. Sel'kin, A. Kaplyanskii, D. Yakovlev and M. Bayer, *Physical Review B*, 2007, **75**, 153101.
105. N. Tétreault, H. Míguez, S. Yang, V. Kitaev and G. A. Ozin, *Advanced Materials*, 2003, **15**, 1167-1172.
106. S. A. Asher, J. Holtz, L. Liu and Z. Wu, *Journal of the American Chemical Society*, 1994, **116**, 4997-4998.
107. H. Fudouzi and T. Sawada, *Langmuir*, 2006, **22**, 1365-1368.
108. M. Kamenjicki Maurer, I. K. Lednev and S. A. Asher, *Advanced Functional Materials*, 2005, **15**, 1401-1406.
109. Z. Z. Gu, T. Iyoda, A. Fujishima and O. Sato, *Advanced Materials*, 2001, **13**, 1295-1298.
110. J.-T. Zhang, N. Smith and S. A. Asher, *Analytical chemistry*, 2012, **84**, 6416-6420.
111. J. H. Holtz and S. A. Asher, *Nature*, 1997, **389**, 829.
112. J. H. Holtz, J. S. Holtz, C. H. Munro and S. A. Asher, *Analytical Chemistry*, 1998, **70**, 780-791.
113. C. E. Reese and S. A. Asher, *Analytical chemistry*, 2003, **75**, 3915-3918.
114. Y. J. Lee and P. V. Braun, *Advanced Materials*, 2003, **15**, 563-566.
115. X. Feng, J. Xu, Y. Liu and W. Zhao, *Journal of Materials Chemistry B*, 2019.
116. X. Hong, Y. Peng, J. Bai, B. Ning, Y. Liu, Z. Zhou and Z. Gao, *Small*, 2014, **10**, 1308-1313.
117. C. Chen, Z.-Q. Dong, J.-H. Shen, H.-W. Chen, Y.-H. Zhu and Z.-G. Zhu, *ACS Omega*, 2018, **3**, 3211-3217.
118. V. L. Alexeev, A. C. Sharma, A. V. Goponenko, S. Das, I. K. Lednev, C. S. Wilcox, D. N. Finegold and S. A. Asher, *Analytical chemistry*, 2003, **75**, 2316-2323.
119. M. Ben-Moshe, V. L. Alexeev and S. A. Asher, *Analytical chemistry*, 2006, **78**, 5149-5157.
120. M. M. Ward Muscatello, L. E. Stunja and S. A. Asher, *Analytical chemistry*, 2009, **81**, 4978-4986.

121. C. Zhang, M. D. Losego and P. V. Braun, *Chemistry of Materials*, 2013, **25**, 3239-3250.
122. Z. Pan, J. Ma, J. Yan, M. Zhou and J. Gao, *Journal of Materials Chemistry*, 2012, **22**, 2018-2025.
123. Y.-X. Zhang, P.-Y. Zhao and L.-P. Yu, *Sensors and Actuators B: Chemical*, 2013, **181**, 850-857.
124. B.-F. Ye, Y.-J. Zhao, Y. Cheng, T.-T. Li, Z.-Y. Xie, X.-W. Zhao and Z.-Z. Gu, *Nanoscale*, 2012, **4**, 5998-6003.
125. G. Huang, Y. Yin, Z. Pan, M. Chen, L. Zhang, Y. Liu, Y. Zhang and J. Gao, *Biomacromolecules*, 2014, **15**, 4396-4402.
126. Y. Matsuhisa, Y. Huang, Y. Zhou, S.-T. Wu, R. Ozaki, Y. Takao, A. Fujii and M. Ozaki, *Applied Physics Letters*, 2007, **90**, 091114.
127. A. Pokhriyal, M. Lu, V. Chaudhery, S. George and B. T. Cunningham, *Applied physics letters*, 2013, **102**, 221114.
128. J. I. L. Chen, G. von Freymann, S. Y. Choi, V. Kitaev and G. A. Ozin, *Advanced Materials*, 2006, **18**, 1915-1919.
129. S. Guldin, S. Huttner, M. Kolle, M. E. Welland, P. Muller-Buschbaum, R. H. Friend, U. Steiner and N. Tetreault, *Nano letters*, 2010, **10**, 2303-2309.
130. P. Zhou, D. Zhou, L. Tao, Y. Zhu, W. Xu, S. Xu, S. Cui, L. Xu and H. Song, *Light: Science & Applications*, 2014, **3**, e209.
131. E. Eftekhari, X. Li, T. H. Kim, Z. Gan, I. S. Cole, D. Zhao, D. Kielpinski, M. Gu and Q. Li, *Scientific reports*, 2015, **5**, 14439.
132. J. Hou, H. Zhang, B. Su, M. Li, Q. Yang, L. Jiang and Y. Song, *Chemistry–An Asian Journal*, 2016, **11**, 2680-2685.
133. Y. Fang, Y. Ni, B. Choi, S. Y. Leo, J. Gao, B. Ge, C. Taylor, V. Basile and P. Jiang, *Advanced Materials*, 2015, **27**, 3696-3704.
134. H. S. Lee, T. S. Shim, H. Hwang, S.-M. Yang and S.-H. Kim, *Chemistry of Materials*, 2013, **25**, 2684-2690.
135. Y. Heo, H. Kang, J. S. Lee, Y. K. Oh and S. H. Kim, *Small*, 2016, **12**, 3819-3826.
136. H. Nam, K. Song, D. Ha and T. Kim, *Scientific reports*, 2016, **6**, 30885.

137. D. P. Puzzo, A. C. Arsenault, I. Manners and G. A. Ozin, *Angewandte Chemie International Edition*, 2009, **48**, 943-947.

Chapter 2

Synthesis of polystyrene microspheres and fabrication of colloidal photonic crystals

2.1. Abstract

Bio-inspired structural coloration in colloidal photonic crystals (CPCs) obtained from highly monodispersed microspheres show angle-dependent color shifting property. In this chapter, highly monodispersed polystyrene (PS) colloidal microspheres were synthesized by emulsion polymerization method. Further, PS microspheres of different particle sizes with narrow size distributions were employed for the fabrication of angle-dependent color shifting CPCs. Later, the CPCs were used as a sacrificial template for the preparation of silica inverse opal photonic crystals (IO-PCs). Large-area CPCs with orderly arranged PS microspheres and brilliant structural color were fabricated by evaporation induced vertical deposition method onto plasma-treated surfaces of hydrophilic glass and flexible polymer films. CPC coatings on flexible polymer films exhibited excellent structural stability even under bending conditions. The photonic band gap (PBG) of PS CPC was tuned by varying the diameter of PS microspheres. In fact, in some of the applications such as color displays, cosmetics, etc., CPCs are required to be in powder form. However, due to light scattering and the random orientation of particles, the powder form of PS CPCs appear white. To address this problem, a more stable three-dimensionally ordered macroporous (3D-OM) silica IO-PC powder was prepared using PS CPC as a template, and charcoal flakes were used as a background absorber for scattered light. Owing to the larger size, charcoal flakes cannot enter into the pores of silica inverse opal (IO), thus maintaining its periodic structural features. Interestingly, silica IO-PC powder showed angle-independent structural color, which may find potential applications such as color displays, sensors, barcodes, etc. where wide-viewing angle-dependent structural color is still challenging.

2.2. Introduction

Many creatures in nature, such as butterflies, beetles, and peacocks show brilliant structural colors by the interaction of light with periodic nano or microstructures on their surfaces.¹⁻³ The color obtained by mimicking the magnificent ordered structures found in natural creatures is commonly referred to as bio-inspired

structural color. Mimicking such nanostructures employs state-of-the-art nanofabrication techniques that are slow, expensive, and not scalable. Strikingly, colloidal microspheres of inorganic/polymeric materials have an attractive property of self-assembling into an ordered structure.^{4, 5} Self-assembly is a fundamental mechanism by which larger structures are formed from smaller structures (bottom-up approach). The self-assembly of colloidal spheres to provide highly ordered crystal, known as colloidal crystals (CCs), find possible applications in various fields such as preparation of photonic crystals (PCs),⁶⁻⁸ three-dimensionally ordered macroporous materials (3D-OM),⁹⁻¹¹ fluorescence enhancement,¹²⁻¹⁴ sensors,¹⁵⁻¹⁷ security materials,¹⁸⁻²⁰ etc. It is worth noting that the length scale of the colloidal particles can be tuned to match the order of the wavelength of visible light. Hence, the ordered colloidal nanoparticles in CC provide structural color by the diffraction of visible light passing through the microstructure.

Self-assembly of colloidal particles, known as colloidal self-assembly, has been of great interest due to the simple preparation method of both the colloidal suspension and well-ordered CCs. Colloidal self-assembly is the commonly used bottom-up approach for PC fabrication, and the PC so obtained is termed as colloidal PC (CPC). In general, CPC of colloid microspheres consists of a periodic arrangement of colloidal particles and air-voids.²¹ Thus, a CPC structure consists of periodic dielectric materials and subsequent periodic modulation in the refractive index provides a platform for the incident light to get diffracted. The Bragg diffraction of visible light from CPC creates a forbidden region of electromagnetic waves from propagating through it.⁴ This region of electromagnetic waves is known as the photonic band gap (PBG) of CPC and which provides brilliant structural colors.

Among various building blocks for colloidal self-assembly, colloid particles with spherical morphology (microspheres), are very promising for highly ordered CPC with close-packed structure. Besides, the microsphere should be highly monodispersed for long-range close-packed arrangement. Emulsion polymerization is the most commonly used method for the synthesis of monodispersed polymer microspheres. Until now, various methods have been reported for CPC fabrication. Solvent evaporation driven

self-assembly,²¹ self-assembly process at the interface,²² sedimentation,²² dipping deposition,²³ slit filling,²⁴ Langmuir Blodgett (LB) technique,²⁵ floating packing,²¹ vertical deposition,²⁶ directed assembly like spin coating,²⁷ electric field,²⁸ etc. are some of the well-known methods. Among various methods, the vertical deposition method provides three dimensional (3D) CPCs with very few defects.

Furthermore, one of the interesting optical properties of CPCs is that the structural color of CPC changes with respect to the viewing angle. CPCs of long-range ordered structures show wide-viewing angle-dependent structural color, namely iridescent color.²⁹ However, low angle-dependent structural colored materials can also be made from colloidal self-assembly. In general, short-range ordered structures of colloidal particle, known as colloidal amorphous array, shows angle independent structural color, namely non-iridescence color.²⁹ Both angle-dependent and angle-independent structural color has its own application potential. For example, in anti-counterfeiting, angle-dependent structural color is more suitable, since it is very difficult to copy them than angle independent structural color. In the case of sensing through naked-eye detection of analyte molecules, angle-independent structural colors are highly preferred, since eye cannot determine the exact viewing angle.

It is noteworthy that in some of the application, CPCs in thin film cannot be directly used, where CPCs in powder form is required. However, powder CPC is white due to light scattering and random orientation of particles in the powder form. It has already been demonstrated that the light-absorbing materials can be used in CPC structure to enhance the intensity of light by absorbing incoherently scattered light. For example, Pursiainen *et al.* used sub-50-nm carbon black particles to enhance the color intensity of highly ordered polymeric colloidal crystal films.³⁰ Zhehong *et al.* also used carbon black for enhancing the structural color of silica-based CPCs. The aforementioned methods utilized smaller black nanoparticles for absorbing scattered light. Non-uniform distribution of smaller black nanoparticles in the pores affects the periodic modulation of the refractive index of PC architecture.

Moreover, polymeric CPC is not structurally stable at higher temperatures. Besides, in CPCs there is only physical contact among microspheres, which further

makes it less stable. However, CPCs were used as a sacrificial template for the fabrication of more stable three-dimensionally ordered macroporous materials (3D-OM).³¹⁻³³ Among various 3D-OM fabricated using CPC based templating method, 3D-OM of silica IO-PC based materials are less toxic, chemically more stable and easy to synthesis.^{31, 34-37}

In this chapter, experimental conditions for both the synthesis of highly monodispersed polystyrene (PS) microspheres and the fabrication of PS CPC by evaporation induced vertical deposition method are described. We synthesized highly monodispersed PS microsphere using the emulsion polymerization method. The particle size was tuned via the concentration of the monomer (styrene). PS CPCs with brilliant structural color were prepared both on a glass substrate and on a flexible polymer substrate. Additionally, 3D-OM of silica IO-PC was prepared using PS CPC as template and silica IO-PC powder with angle-independent structural color was prepared using charcoal flakes as the absorbing material for scattered light. Compared to existing reports of the use of smaller sized carbon black nanoparticles as the background absorber for scattered light, larger-sized charcoal flakes, cannot enter into the pores of silica IO-PC which maintain its periodic structural features.

2.3. Experimental

2.3.1. Chemicals and materials

Styrene, Tetraethyl orthosilicate (TEOS) and activated charcoal were purchased from Sigma-Aldrich (India). Sodium dodecyl sulfate (SDS), hydrochloric acid (HCl), ethanol and potassium per sulfate (KPS) were purchased from Merck (India). For all the experiments ultrapure deionized water (18.2 M Ω .cm, 25 °C, Milli-Q D3, Merck) was used.

2.3.2. Synthesis of polystyrene (PS) microspheres and fabrication of PS CPCs

Monodispersed PS microspheres of varying particle sizes were synthesized as reported elsewhere³⁸ and colloidal suspension was purified by centrifugation. For the synthesis, 15 mL of DI water was taken in a three-neck round bottom flask. 4.5 mg of sodium dodecyl sulfate (SDS) as emulsifier, 50 mg of potassium per sulfate (KPS) as

initiator was added with stirring under N₂ gas atmosphere and was heated to 75 °C in an oil bath for 15 min. Then, 3 ml of styrene was added dropwise and the reaction mixture was kept at a constant stirring of 350 rpm and temperature of 75 °C for 3 h to get monodispersed PS colloid.

2.3.3. Fabrication of PS CPCs

Glass coverslips were cleaned by sonication consecutively in ethanol, toluene and again in ethanol for 5 min each followed by N₂ plasma treatment for 5 min to make the glass surface clean and hydrophilic. Monolithic PS CPCs were prepared on a cleaned glass substrate via evaporation induced vertical deposition method.³⁹ The PBG of CPC was tuned by varying the diameter of PS microspheres. The thickness of CPCs films were controlled by varying the concentration (wt %) of PS colloids.

2.3.4. Preparation of PS CPC powder

PS CPC powder was made from PS CPC film prepared by a vertical deposition method. PS CPC film was scratched out and lightly ground using mortar and pestle.

2.3.5. Fabrication of silica IO-PC using PS CPCs as template and preparation of silica IO-PC powder

The precursor solution for silica IO-PC was prepared as reported elsewhere.³¹ Briefly, the precursor solution consisted of 1:1:1.5 ratios by weight of TEOS, 0.1 M HCl, and ethanol, respectively, and was stirred at room temperature for 1 h prior to use. The precursor solution was then infiltrated into the voids of the PS CPC template and was kept in the air at 500 °C for 2 h to remove the PS CPC template and to sinter the SiO₂ structure to get the silica IO-PC. Silica IO-PC film was transferred and lightly ground using mortar and pestle to get silica IO-PC powder. Silica IO-PC powder was then mixed with charcoal using mortar and pestle for absorbing scattered light.

2.3.6. Characterization

Arrangement of PS CPCs and particle size of PS microspheres were analyzed using field-emission scanning electron microscope, FE-SEM (FEI Nova NanoSEM 450). A thin layer of gold was sputtered on PS CPC films to avoid charging effect. UV-visible

reflectance spectra were recorded using UV-visible spectrophotometer (UV-2600, Shimadzu). Fluorescence emission spectra were recorded using Spectrofluorimeter (Fluorolog-HORIBA Jobin Yvon Inc). The thickness of CPC was measured on Dektak XT profilometer (Bruker). The hydrodynamic particle size of PS microspheres was obtained by Dynamic Light Scattering (Nano ZS, Malvern instrument). Fluorescence lifetime experiments were conducted using a Delta Flex modular time-correlated single-photon counting (TCSPC) spectrometer system. X-ray Photoelectron Spectroscopy (XPS) data were collected using PHI 5000 Versa Probe II ULVAC-PHI Inc., USA equipped with micro-focused (200 μm , 15 KV) monochromatic Al K α X-ray source ($h\nu = 1486.6$ eV). Survey scans were recorded with an X-ray source power of 50 W and pass energy of 187.85 eV. Narrow scans of the major elements were recorded at 46.95 eV pass energy. Data analysis and peak fitting of the XPS spectra were done using Multipak software. The carbon peak at 284.6 eV was used for the calibration of the XPS data. FTIR spectra were obtained on a PerkinElmer FTIR spectrometer. Thermogravimetric Analysis (TGA) thermograms were recorded in the heating process by using Thermal Analysis System (HITACHI, STA7300) under the nitrogen gas atmosphere at a rate of 10 $^{\circ}\text{C}/\text{min}$. Differential Scanning Calorimetry (DSC) was used to acquire glass transition temperature (T_g) of the microspheres using Perkin Elmer Pyris 6 DSC at a heating rate of 10 $^{\circ}\text{C}/\text{min}$. Optical Microscope (OM) images were obtained using Leica DMRX instrument. Photographs of all the samples were taken with Nikon D4 digital camera.

2.4. Results and Discussion

2.4.1. Synthesis monodispersed PS microspheres

Monodispersed PS microspheres were synthesized by emulsion polymerization. The as-synthesized colloid suspension was milky-white, as shown in the photograph (fig. 2.1a.). In general, the particle size of the microsphere and polydispersity index (PDI) of microspheres depends on the experimental conditions such as temperature, rotational speed (rpm) of the reaction medium, and the concentration of the reactants. To synthesize the microspheres uniform in size (monodispersed and having low PDI),

reaction temperature and rpm were kept constant throughout the reaction. The morphology of the PS microspheres was revealed by SEM and TEM (fig. 2.1b, c, and d). Low magnification SEM and TEM images (fig. 2.1b and c) indicate that the colloidal solution consists of particles of uniform size. SEM image indicates that particles were not aggregated even after drop-casting (SEM samples were prepared by drop-casting the colloid on glass coverslips and was dried overnight at 50 °C). Higher magnification TEM image (fig. 2.1d) indicates that the particles have spherical morphology. SEM and TEM images showed no cross-linking among PS microspheres. These observations suggest that the as-synthesized PS microspheres are well-suitable for large area orderly arranged colloidal crystals, which in turn enhances the optical quality of CPCs.

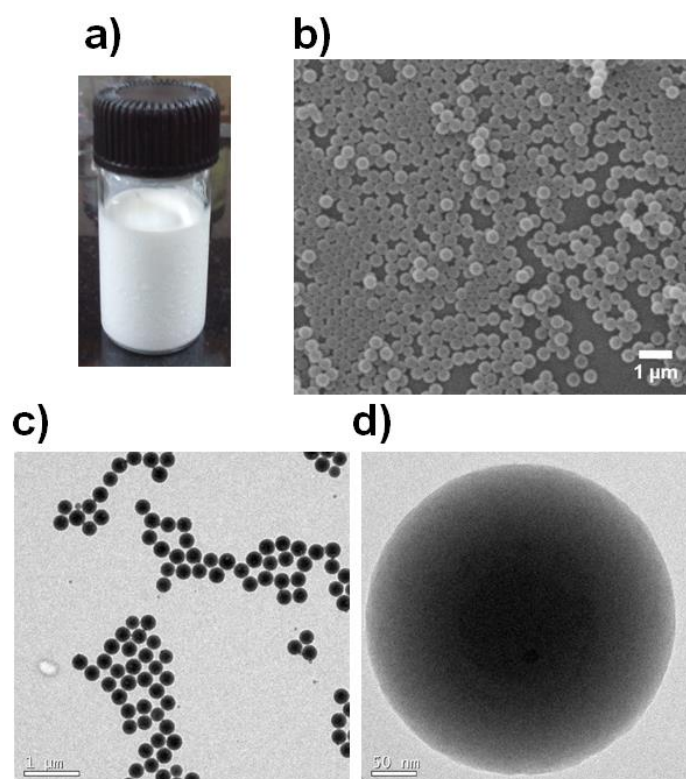


Fig. 2.1. a) Digital photograph of PS microspheres suspension b) SEM image c) and d) TEM images of PS microspheres.

The particle size of PS microspheres was tuned by varying the amount of monomer (styrene), whereas the concentration of surfactant (SDS) and initiator (KPS) were kept constant. The amount of styrene used and the corresponding hydrodynamic

diameter, PDI and zeta potential measured using DLS equipment are shown in Table 2.1, and the particle size distribution (DLS curve) is shown in fig 2.2a, b, and c, which indicates that hydrodynamic diameter was increased when the concentration of styrene was increased. The hydrodynamic diameters obtained were 190 nm, 255 nm, and 297 nm with the styrene concentrations (weight %) of 12.6 %, 13.6 %, and 14.8 %, respectively, and the corresponding particle size obtained from SEM was 180 ± 3 nm, 230 ± 5 nm and 250 ± 6 nm. The polydispersity index (PDI) of the as-synthesized PS microspheres (Table 2.1) was very low, indicating that the colloidal particles are highly monodispersed, which is an important criteria for the preparation of high-quality CPC films. Additionally zeta potential of the PS microspheres indicates that the PS suspension is more stable. As the surface charge is more negative, the particles repel one another, and thus making the colloid stable. Till nucleation and crystallization in colloidal self-assembly formation, colloidal particles should stay apart, which is facilitated by the high surface charge. During nucleation and crystallization, the repulsive force will be overcome by the attractive capillary force to get well-ordered CPCs.

Table 2.1. Amount of styrene, corresponding hydrodynamic diameter, PDI and zeta potential of as-synthesized PS microspheres

Amount of styrene (mol %)	Hydrodynamic diameter (nm)	PDI	Zeta potential (mV)
9.07	190	0.06	-37.5
9.78	255	0.06	-21.7
10.60	297	0.16	-44.3

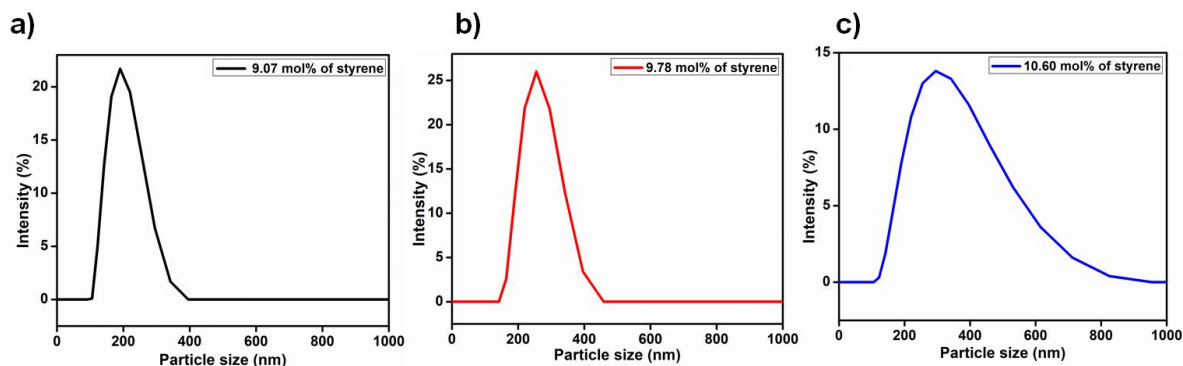


Fig. 2.2. a) b) and c) Particle size distribution of PS microspheres synthesized by varying the mol% of monomer (styrene).

Further PS microspheres were characterized using FTIR spectroscopy. The FTIR spectrum (Fig. 2.3a), including the fingerprint region, was the same as that of typical polystyrene, indicating the formation of polystyrene polymer. The aromatic C-H stretching vibration peaks at 2927 cm^{-1} and 3027 cm^{-1} and aromatic C=C stretching vibration peak at 1600 cm^{-1} , 1494 cm^{-1} , and 1447 cm^{-1} were due to the presence of benzene rings. The peak at 754 cm^{-1} and 700 cm^{-1} were due to C-H out of plane bending vibration. Additionally, XPS analysis was performed to know the elemental composition, which shows carbon and oxygen as major elements. From the XPS survey spectra, atomic % of carbon and oxygen were found to be 95.9 % and 3.3 % (Table 2.2). The oxygen may be from the adsorbed anions at the surface of PS microspheres and which contribute to the increased surface charge making the colloid stable. Narrow-scan C1s spectra shown in fig. 2.3b reveals the presence of C-C and C-O bonds. The C-O peak may be from the adsorbed anions of SDS (surfactant). The $\pi\text{-}\pi^*$ shake-up satellites peak was from aromatic ring.

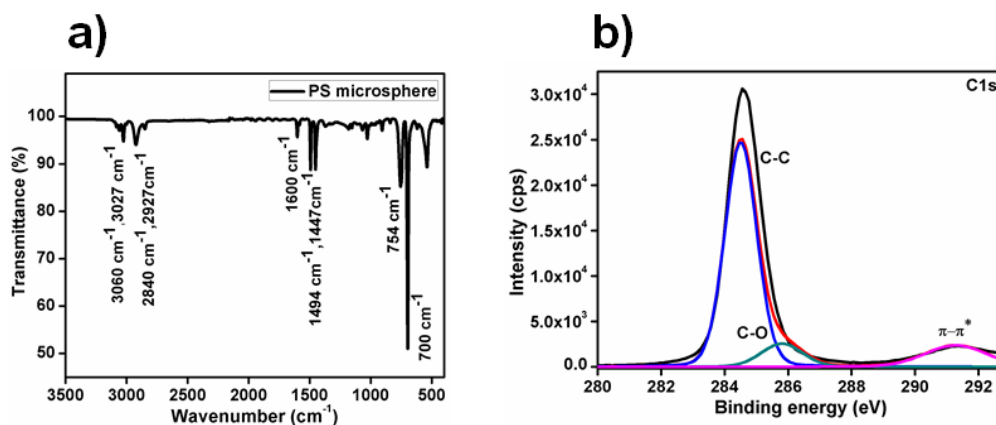


Fig. 2.3. a) FTIR spectra and b) XPS high-resolution C1s narrow scan of PS microspheres.

Table 2.2. Atomic % of PS microspheres from XPS data.

Element	Atomic %
C1s	95.9%
O1s	3.3%

Further, PS microspheres were characterized using TGA and DSC and curves are shown in Fig. 2.4a and b respectively. TGA thermogram indicates that the temperature at which 50 % weight loss occurs ($T_{0.5}$) was at 414 °C. From the DSC thermogram, the glass transition temperature (T_g) was found to be 106 °C, which indicates that the PS microsphere loses its spherical morphology at 106 °C. Thus, CPC made of PS microspheres would lose its orderly arranged periodic structure, and hence the structural color above 106 °C, which prevents it from higher temperature applications.

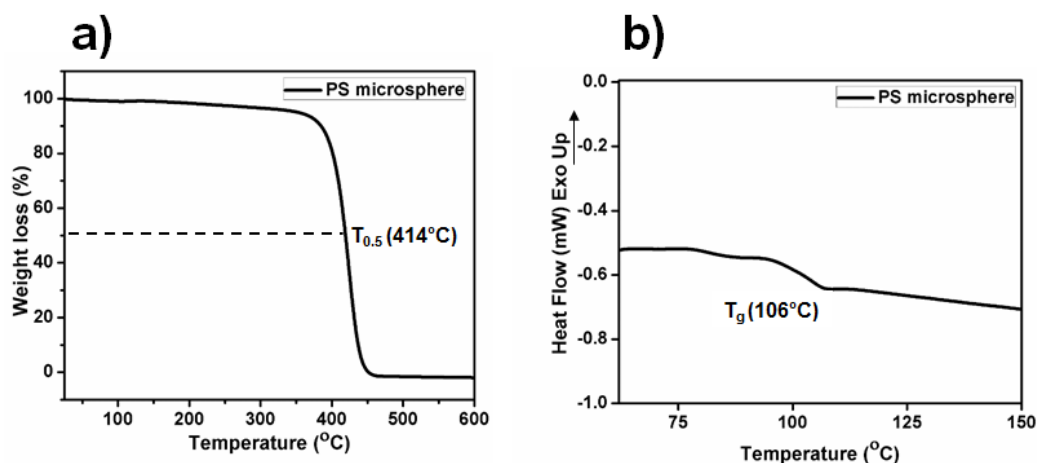


Fig. 2.4. a) TGA and b) DSC curve of PS microspheres.

2.4.2. Fabrication of PS-based CPCs

2.4.2.1. Pre-treatment of substrate

We adopted an evaporation induced vertical deposition method for PS CPC fabrication. Both glass (glass coverslips) and flexible polymer (mylar film) were used as the substrates. Any substrate which is hydrophilic or which can be made hydrophilic (example: N_2 plasma treatment) can be used for CPC fabrication. Among various substrate which can be used for CPC fabrication, herein mylar film was selected as the flexible substrate. In order to make good quality CPCs, substrates should be clean and hydrophilic. In the vertical deposition method, for wetting the substrate with solvent (water) and to obtain uniform coating, hydrophilic substrate is required. The substrates were cleaned by sonication consecutively in ethanol, toluene and again in ethanol for 15 min each followed by N_2 plasma treatment for 5 min. The pre-treatment of the substrate removed the organic and inorganic impurities from the substrate surface and made it hydrophilic. To know the hydrophilicity of the substrates, we performed water contact angle measurements, and are shown in fig. 2.5, and table 2.3. The contact angle of the glass substrate was 59° and 10° before and after N_2 plasma treatment respectively, whereas the contact angle of mylar film was 80° and 5.6° before and after pre-treatment, respectively.

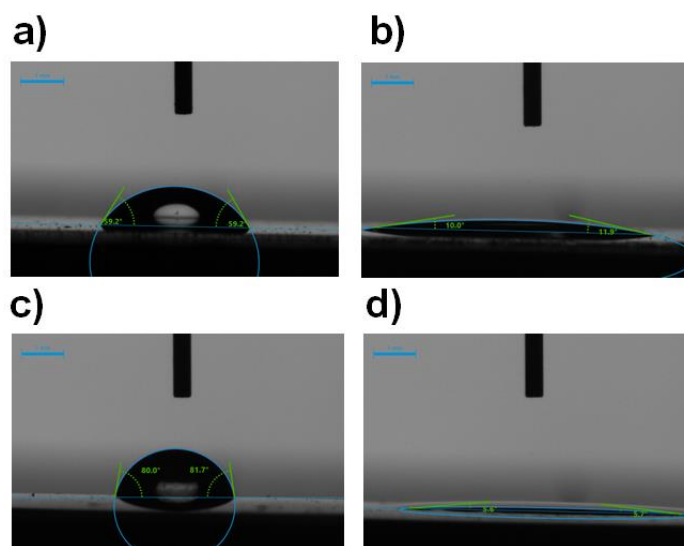


Fig. 2.5. Contact angle measurements of a) and c) before pre-treatment and b) and d) after pre-treatment on glass substrate and flexible polymer substrate (mylar film), respectively.

Table 2.3. Contact angle measurements of glass substrate and a flexible polymer substrate before and after pre-treatment.

Substrate	Water contact angle	
	Before pre-treatment	After pre-treatment
Glass coverslip	59°	10°
Mylar film	80°	5.6°

2.4.2.2. Fabrication of PS-based CPCs by evaporation induced vertical deposition method

In the vertical deposition method, orderly arranged close-packed colloidal crystals were deposited on a hydrophilic substrate. Here, the substrate is placed vertically (80° from the horizontal surface) into the colloidal suspension and is subjected to controlled evaporation (fig. 2.6a). In the vertical deposition method, the

CPC formation depends upon temperature and humidity, since the assembly formation is based on evaporation of the solvent. We optimized these parameters by varying the temperature and humidity. In general, the quality of the colloidal crystal would be excellent if the evaporation rate is slow. At higher humidity, the evaporation rate is slow. In order to know the dependence of crystalline quality at different humidity, we performed vertical deposition method in a desiccator at room temperature. The relative humidity of the system was varied by the use of salt (Table 2.4). When saturated K_2SO_4 was used, the relative humidity was 90 %, and it took 7 days for the self-assembly to be completed at room temperature (RT), since the evaporation rate was prolonged. However, the crystalline quality of CPC was excellent. SEM image in fig 2.6d shows long-range ordered close-packed arrangement at 90% humidity. Further, we reduced the relative humidity to 74 % by the use of NaCl solution, and it took 5 days for the self-assembly to be completed. The quality of CPC was excellent and the SEM micrograph is shown in fig 2.6e. Later, the relative humidity was increased to 33 % by the use of $CaCl_2$, but it took 4 days for the self-assembly to be completed. However, the quality of CPC obtained at 33 % relative humidity was not as excellent as that obtained at 90 % and 74 % humidity, and is visible from the SEM image shown in fig 2.6f. We observed that the vertical deposition method was not appreciable in desiccator owing to the long-time scale caused by very slow evaporation. Further, we performed the vertical deposition method in a water bath and the schematic representation is shown in fig 2.6b. We performed a vertical deposition method at 70 °C at relative humidity of 60-65 %; colloidal crystals were formed within 18 h. However, the crystalline quality of the CPC was not good due to fast drying. SEM image in fig 2.6g showed no long-range order. Later the temperature was decreased to 55 °C at relative humidity of 60-65 %. At this experimental condition, we obtained colloidal crystal within 24 h, and the quality of the colloidal crystal was excellent. SEM image shown in fig 2.6h showed long-range ordered and close-packed arrangement. Hence throughout the entire thesis work, we used vertical deposition in water bath at 55 °C. A digital photograph of a CPC fabricated on a hydrophilic glass substrate utilizing this method is shown in fig. 2.6c, which indicates brilliant structural color due to Bragg

diffraction. Thus, iridescent CPC was fabricated from white-colored PS colloid (Fig. 2.6c).

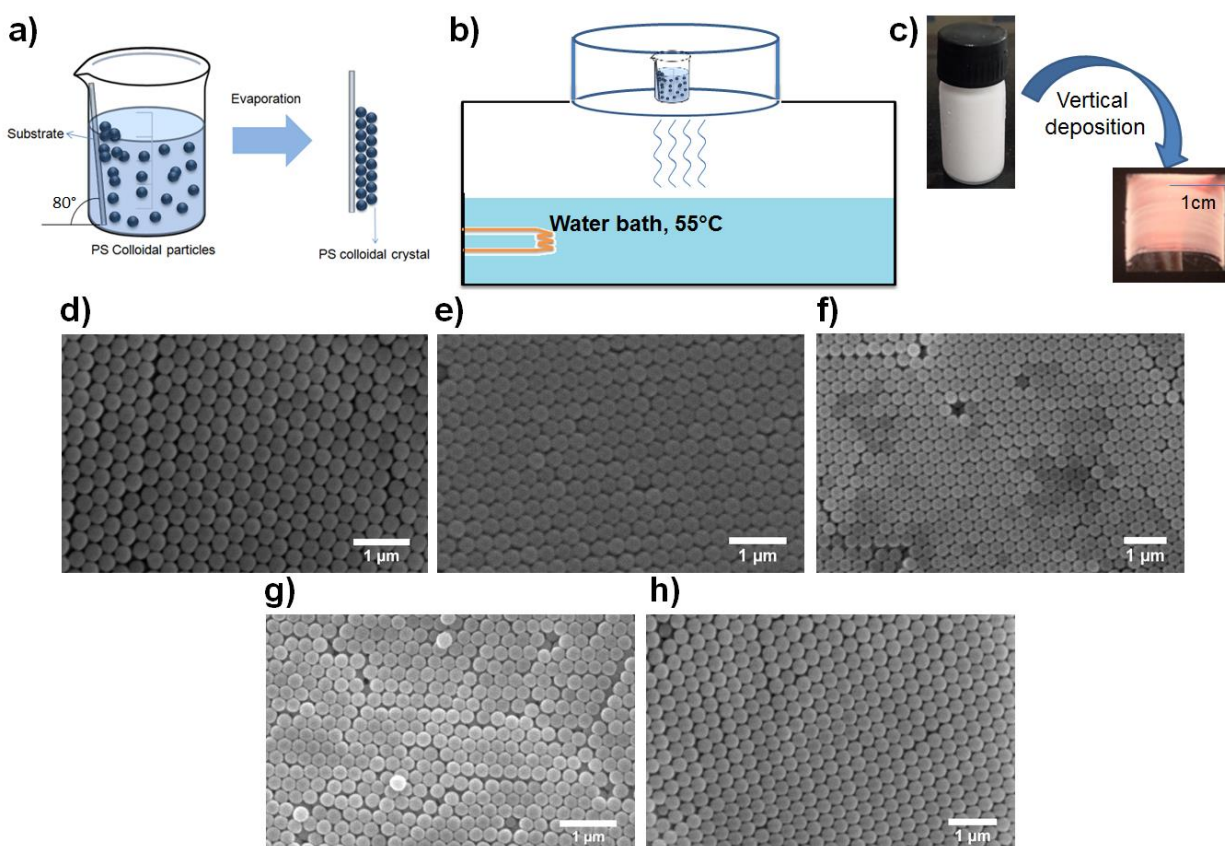


Fig. 2.6. Schematic representation of a) vertical deposition method b) represents experimental set-up of vertical deposition method on a water bath, c) digital photograph of PS colloid suspension and CPC fabricated from it and d-f) represents the SEM image of PS CPC obtained using vertical deposition method in desiccator at a relative humidity of 90 %, 74 %, and 30 % respectively, and g-h) represents the SEM images of PS CPC obtained using vertical deposition method on water bath at 70 and 55 °C respectively.

Table 2.4. Experimental setup, relative humidity, temperature and time of vertical deposition method

Experimental setup	Relative Humidity (%)	Temperature (°C)	Time
Desiccator with saturated K₂SO₄ solution	90	RT	7 days
Desiccator with saturated NaCl solution	74	RT	5 days
Desiccator with dry CaCl₂ salt	33	RT	4 days
Water bath	60-65	70	18 h
Water bath	60-65	55	24 h

2.4.3. Structural color and tuning of PBG in PS CPCs

Structural color and the PBG of PS CPCs were tuned by varying the diameter of PS microspheres. Monodispersed PS microspheres having hydrodynamic diameter 190 nm, 255 nm, and 297 nm were synthesized by varying the concentration of monomer (styrene) used (12.6, 13.6, and 14.8 weight %, respectively), and PS CPCs were fabricated using vertical deposition method as mentioned in the above section. The particle size of PS microsphere obtained from SEM micrographs was 180 ± 3 nm, 230 ± 5 nm, and 250 ± 6 nm. We prepared PS CPCs by evaporation induced vertical deposition method on a plasma cleaned hydrophilic glass substrate. Fig. 2.7b shows SEM micrographs of PS CPC films which revealed a face-centered cubic (FCC) arrangement with (111) plane parallel to the surface of the substrate. Digital photographs of CPCs were shown in fig 2.7a as well as the inset of fig. 2.7b, which exhibits different structural colors due to PS microspheres of different particle sizes. CPCs made of PS microspheres of particle size, 180 ± 3 nm, 230 ± 5 nm, and 250 ± 6 nm impart violet,

green, and orange structural colors, respectively. The PBG of PS CPC films were acquired from reflectance spectra with light incident along the normal surface of CPC films (Fig. 2.7c). On varying the diameter of PS microspheres, CPCs exhibit different PBG due to changes in spatial periodicities of dielectric constants. We obtained PBG of violet, green, and orange-colored CPC films at 414 nm, 559 nm, and 599 nm, respectively. The PBG of CPC can be calculated using Bragg's diffraction model.⁴⁰

$$\begin{aligned}\lambda_{max} &= 2d_{(111)}(n_{eff}^2 - \sin^2\theta)^{1/2} \\ &= 2(2/3)^{1/2} D(n_{eff}^2 - \sin^2\theta)^{1/2}\end{aligned}$$

where, λ_{max} denotes the wavelength maxima of reflection peak, $d_{(111)}$ is the interplanar distance between adjacent (111) crystallographic planes, D is the sphere diameter and n_{eff} is the effective refractive index of CPC film which is calculated from the equation, $n_{eff}^2 = \sum f_i n_i^2$, where n_i is the refractive index of the respective phase (PS and air) and f_i is the corresponding volume fraction. In the calculation of n_{eff} , refractive index of PS and air was taken as 1.59 and 1.0, respectively. Since CPC consist of fcc structure, volume fraction of PS and air-void was taken as 0.74 and 0.26, respectively. Table 2.5 shows the calculated and experimental values of λ_{max} of CPC films corresponding to different particle sizes of PS microspheres. It is obvious that the experimental values of λ_{max} are in agreement with calculated values indicating well-ordered PS CPCs.

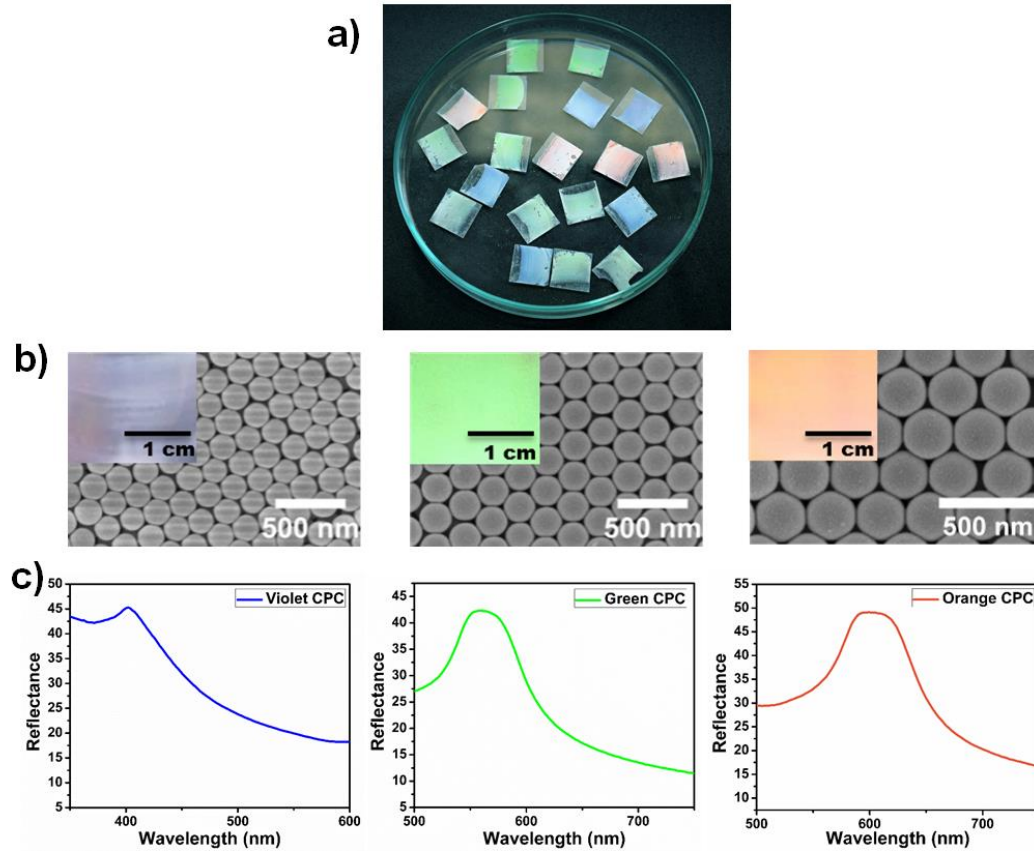


Fig. 2.7. a) Digital photograph of PS CPCs on a glass substrate and b) SEM micrographs, (corresponding digital photographs in the inset) and c) reflectance spectra of violet, green and orange colored PS CPCs.

Table 2.5. Particle size and photonic band gap (PBG) positions of violet, green and orange colored PS CPCs.

Color of PS CPC	Particle size (nm)	Calculated λ_{\max} (nm)	Experimental λ_{\max} (nm)
Violet	180±3	429	414
Green	230±5	548	559
Orange	250±6	595	599

Further, the thickness of PS CPC films was optimized for obtaining the highest reflectivity. The thickness of CPC films was tuned by varying the concentration of the PS colloid. Fig. 2.8a, b, and c show the reflectance spectra of violet, green, and orange PS CPCs films with varying film thickness, respectively, which indicate that the reflectivity of PS CPC films increases with an increase in thickness. However, after reaching maximum intensity, a further increase in film thickness reduces the intensity of Bragg diffraction, which may be due to defects in thicker CPC films.^{41, 42} Defects in the colloidal crystal cause more scattered light which reduces the intensity of Bragg diffraction. Remarkably, the position of PBG maxima remains unaffected. For each of the PS CPC films, the intensity of reflectance reached the maximum for a film thickness of around 6.7 μm .

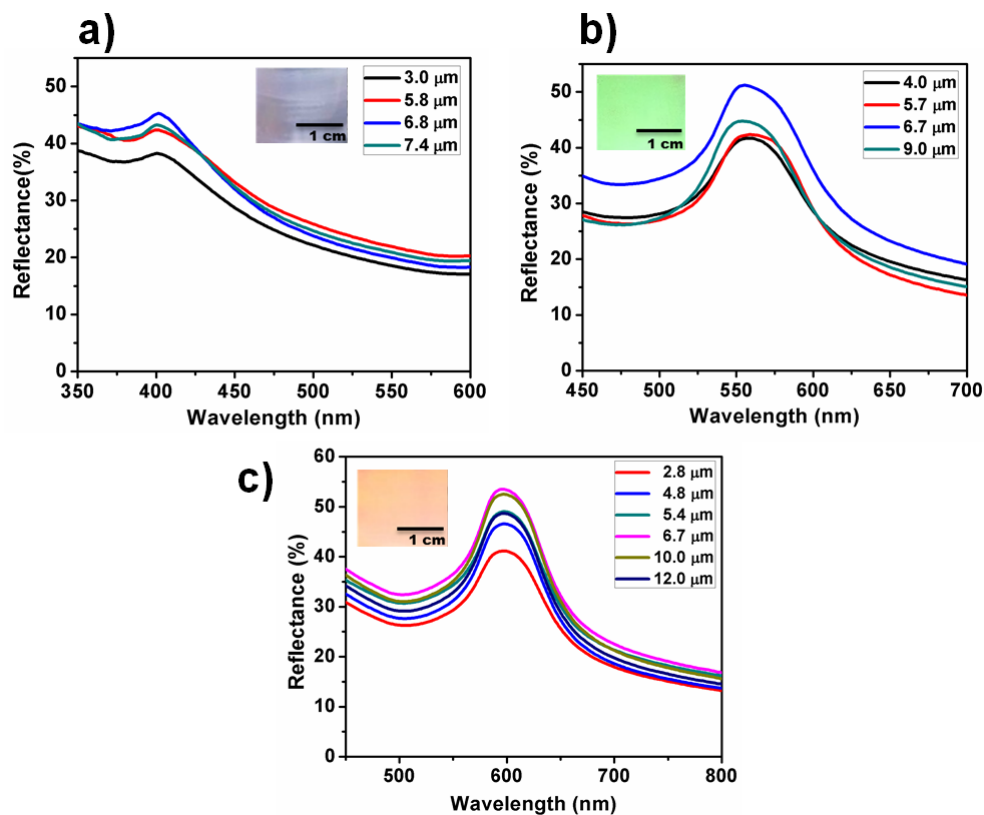


Fig. 2.8. Reflectance spectra of a) violet, b) green, and c) orange CPCs of varying film thicknesses.

2.4.4. Fabrication of PS CPC on flexible substrate

PS CPCs were fabricated on cleaned hydrophilic mylar film, and the photograph is shown in fig 2.9a, b, c, and d. PS CPCs on flexible substrate revealed brilliant structural color due to Bragg diffraction. Fig 2.9d demonstrate that the PC structure and the structural color is stable under mechanical bending conditions.

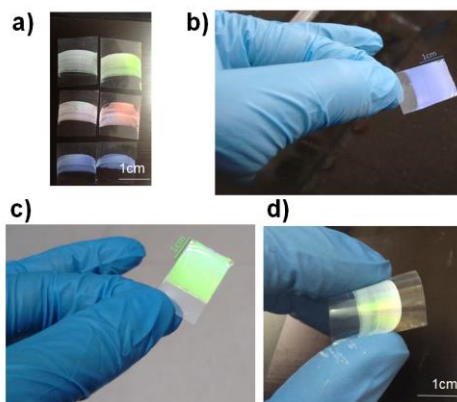


Fig. 2.9. a) b) and c) represents digital photograph of PS CPC on flexible substrate d) demonstrate the structural stability of PS CPC film on flexible substrate under mechanical bending conditions.

2.4.5. Structure, defect, contact angle and thermal stability of PS CPC

SEM micrograph in fig. 2.10a-d represents the structure and defect in PS CPCs. Fig 2.10a represents the top view image, which shows the hexagonal close-packed (111) planes, which is thermodynamically more stable. Fig. 2.10b represents the side view/sectional view of PS CPC, which indicates the three-dimensional (3D) structure. The number of layers and hence, the thickness of the PS CPC film can be controlled by varying the weight % of the PS CPC colloid used for the vertical deposition method. The PS CPC consists of a periodic arrangement of PS microsphere and air-voids. The refractive index of PS microsphere is 1.59 and that of air is 1, which leads to a periodic modulation of refractive index for structural coloration by Bragg diffraction. The air-voids existed in PS CPC are macroporous, which are interconnected, and which provide a room for the infiltration of another material. Thus PS CPC can act as a sacrificial template for the preparation of its inverse structure. As shown in fig. 2.10c and d PS

CPC consists of defects such as vacancy and cracks. This may be due to small size variation, dislocation, and stacking fault of colloids. Defects are entropically favoured to minimize free energy. Defects present in CPC affect the optical quality, and more the defect, less bright would be the structural color. In order to know the wettability of PS CPC surface, water contact angle measurement was performed and is shown in fig. 2.10e. Contact angle was found to be 115.25° , suggesting the hydrophobic behaviour of PS CPC surface. In order to understand the thermal stability of PS CPC structure, SEM micrograph were taken before and after T_g . From DSC curve (Fig. 2.4b), T_g of PS was found to be 106° . Fig. 2.10f represents SEM micrograph of PS CPC at room temperature (RT), which indicate orderly arranged PS microsphere. For studying the morphology above T_g , PS CPCs were heated in vacuum oven at various temperature for 10 min. Fig. 2.10g shows SEM micrograph of PS CPC heated at 110°C and which indicate that PS microsphere in CPC structure was fused together and air-void in the structure was lost. However, periodic arrangement of curved structure was visible at the surface. Interestingly, PS CPCs heated at 150°C and 180°C (Fig. 2.10h and i, respectively) showed planar morphology. These results indicate that PS CPC structure is not stable above T_g .

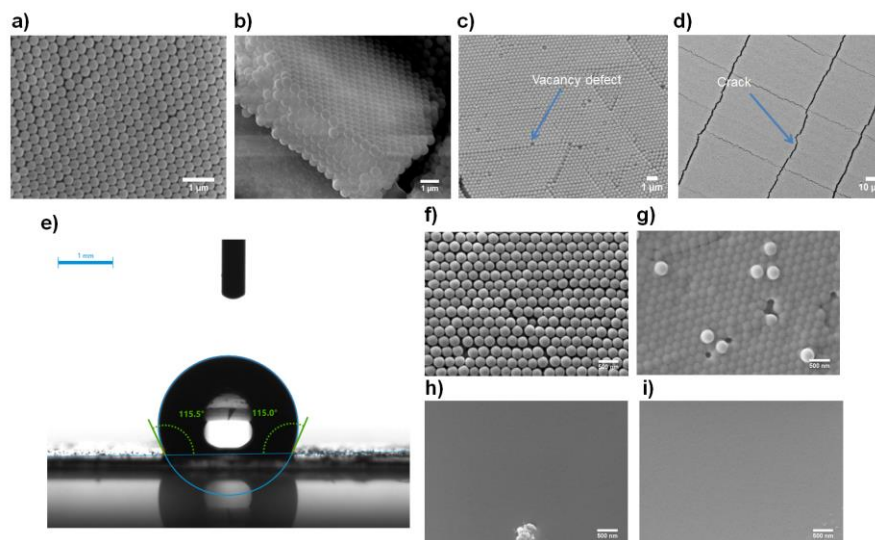


Fig.2.10. a), b), c), d) represents the SEM micrograph of PS CPCs revealing the structure and defects, e) represents contact angle measurement of PSCPC, f), g), h) and i) represents SEM micrograph of PS CPC at RT, 110°C , 150°C and 180°C , respectively.

2.4.6. Angle-dependent structural color in PS CPCs

The structural color of PS CPC was iridescent (angle-dependent). Fig. 2.11a and b show the digital photographs of a violet PS CPC at different viewing angles, which clearly indicate the angle-dependent structural color in PS CPCs. Fig. 2.11c shows the digital photograph of a green CPC on a flexible substrate at bending condition, which clearly indicate that due to the changes in viewing angle, the sample showed different color at different areas. Generally, CPCs with long-range ordered structures exhibit an angle-dependent structural color.²⁹ The PS microsphere used for the present work was highly monodispersed and showed uniform spherical morphology. This in turn facilitated highly ordered close-packed arrangements in PS CPC structure, which were evident from the SEM micrographs.

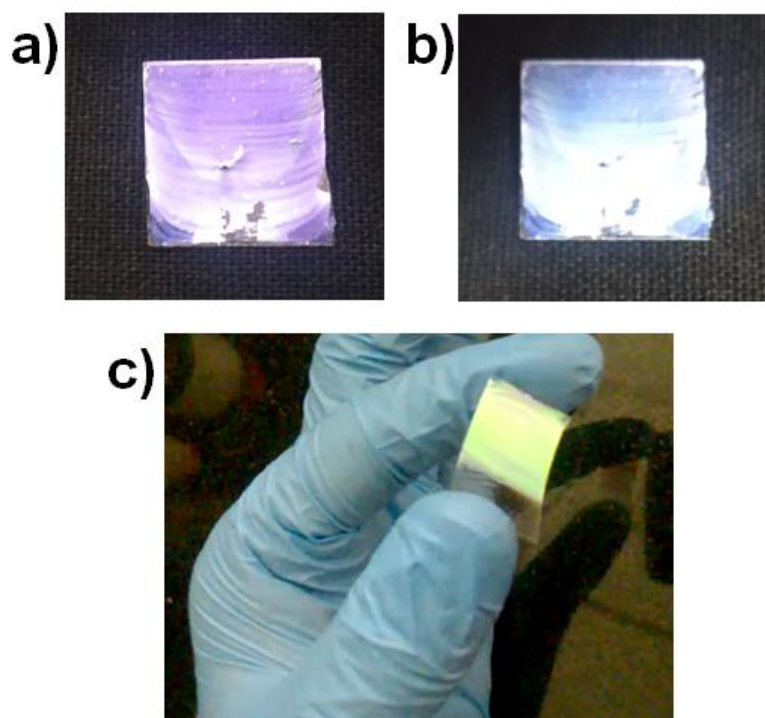


Fig.2.11. a) and b) represents the structural color of a violet PS CPC at different viewing angle, and c) shows the structural color of a green PS CPC on a flexible substrate revealing different colors at different areas due to the changes in viewing angle.

2.4.7. Mechanism of colloidal self-assembly

Colloidal self-assembly in the vertical deposition method is based on solvent evaporation and is shown in fig. 2.12a and is commonly referred to as convective assemblies. The self-assembly process takes place by the formation of a very thin liquid film the crystallization front. The self-assembly process includes nucleation, migration of particles towards the crystallization front, and crystallization. The colloidal self-assembly formation is due to the combined effect of convective drag force, electrostatic repulsion, and capillary attraction, which operate during self assembly process. The driving forces in crystallization are the immersion capillary forces which is an attractive force. In the initial stages of the self-assembly process, the solid substrate (here the substrate is both glass and flexible polymer film) is wetted by the solvent (water), which is facilitated by the low water contact angle. If the water contact angle is high, water film dewets before the immersion capillary force is acted. As the zeta potential of the PS colloid is high and the colloid is more stable, particles in the colloid undergo no aggregation before the formation of a well-ordered structure. As the interaction with the substrate is small, colloid particles in contact with the substrate are free to move for self-organization. During evaporation (fig. 2.12a), the meniscus is pinned at the substrate and due to evaporation, particles are moved towards the crystallization front via convective particle flux (fig. 2.12a). This convective flow opposes random Brownian motion, and the colloidal particles are dragged from the bulk dispersion to the nucleating center. When the thickness of the liquid film at the substrate becomes less than that of particle size, immersion capillary forces act at the triple-phase boundary (solid particles, liquid solvent and air medium above the colloid), which is attractive and directs the particle to come together to obtain close-packed structure(fig. 2.12b). Crystallization is completed until all the solvent is evaporated, which is followed by the drying of the CPC.

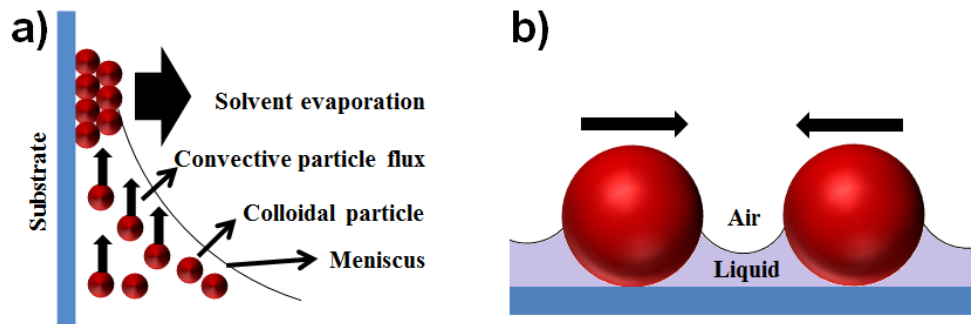


Fig. 2.12. a) Mechanism of colloidal-self-assembly in vertical deposition method and b) capillary force acting at the triple phase boundary which direct the colloid particles to come together.

2.4.8. Optical properties of PS CPC powder

In some special applications, CPC in film form is not recommended. For example, in some color display, CPC should be in powder form to prepare ink formulation for printing applications. Therefore, here we made CPCs using a vertical deposition method, transferred the CPC powder, and lightly ground using a mortar and pestle into CPC powder. Powdered CPC made using an orange CPC is shown in fig. 2.13a, which shows that the powdered CPC was white and is challenging due to the loss of structural color. SEM image in fig. 2.13b and c reveal that the powder CPC consists of particles of a wide distribution of size. To study the structural color of powdered CPC, we have taken the optical microscope (OM) images and is shown in fig. 2.13d and e. CPC powder consists of both orange-colored particles as well as white-colored particles, which is due to the different orientations of particles in the powder form. However, CPC powder was white to the naked-eye. Fig. 2.13f and g show the schematic representation of the reflection in both CPC film and CPC powder, respectively. In CPC film, wavelength region matching the PBG is diffracted, and the structural color can be observed by the naked-eye. However, in the CPC powder, due to the changes in the orientation of particles, incident light is reflected in a different direction. Scattering of incident light in multiple directions dominates over the reflected light in a particular direction along the viewing angle. Hence, the powder CPC looks white for the naked-eye. But the structural color of powder CPC was observed with OM, since it can

selectively collect the reflected light from a small area under focus. The white color of powder CPC prevents it from the practical applications of structurally colored materials. To understand more about the structural color of powder PC and to make a more stable PC, silica IO-PC was prepared.

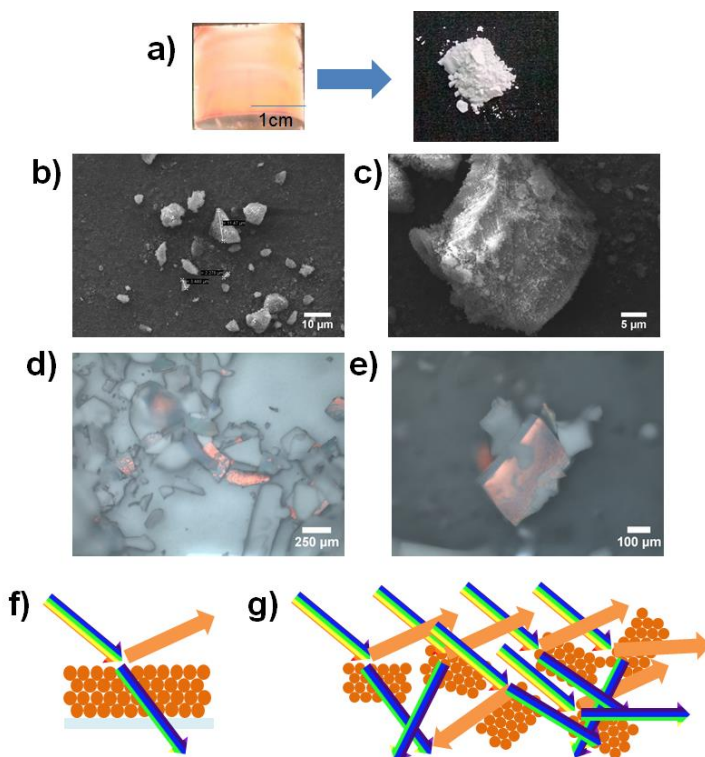


Fig. 2.13. a) Digital photograph of orange PS CPC and CPC powder, b) and c) SEM images of PS CPC powder at different magnifications, 10 μm and 5 μm respectively, d and e) represents OM images of PS CPC powder with scale bar 250 μm and 100 μm respectively, f) and g) depicts schematic representation depicting the reflection in both CPC film and CPC powder, respectively.

2.4.9. Fabrication of silica IO-PC using PS CPC as a template

Silica IO-PC were fabricated using PS CPC as a sacrificial template. Fig. 2.14a shows the schematic representation of the template-based fabrication method of silica IO-PC. Precursor solution containing TEOS, ethanol, and HCl was infiltrated into the air-voids of PS CPC and kept at 500 $^{\circ}\text{C}$ for 2 h. At higher temperature, PS CPCs was removed by thermal etching, and silica IO-PC was formed and sintered. Fig. 2.14b

represents the photograph of silica IO-PC, which showed a blue structural color. SEM image is shown in fig. 2.14c reveal the formation of porous IO-PC structure. The structure of the IO-PC was the exact inverse structure of the PS CPC template. SEM image shows the hexagonal and periodic arrangement of macropores. From the SEM image, pores in the next bottom layer are visible, which suggests that these pores are interconnected, providing a network structure. The IO-PC structure showed variation in pore size, which ranges from around 230 to 250 nm. The highly ordered arrangement of silica IO-PC causes periodic modulation in the refractive index, which leads to Bragg diffraction, structural color, and the existence of PBG. Fig. 2.14d represents the FTIR spectra of silica IO-PC. The bands observed at around 1075 cm^{-1} , 801 cm^{-1} , and 450 cm^{-1} were due to Si–O–Si asymmetric vibration, Si–O symmetric vibrations, and Si–O–Si bending vibration respectively, which confirmed the synthesis of silica.

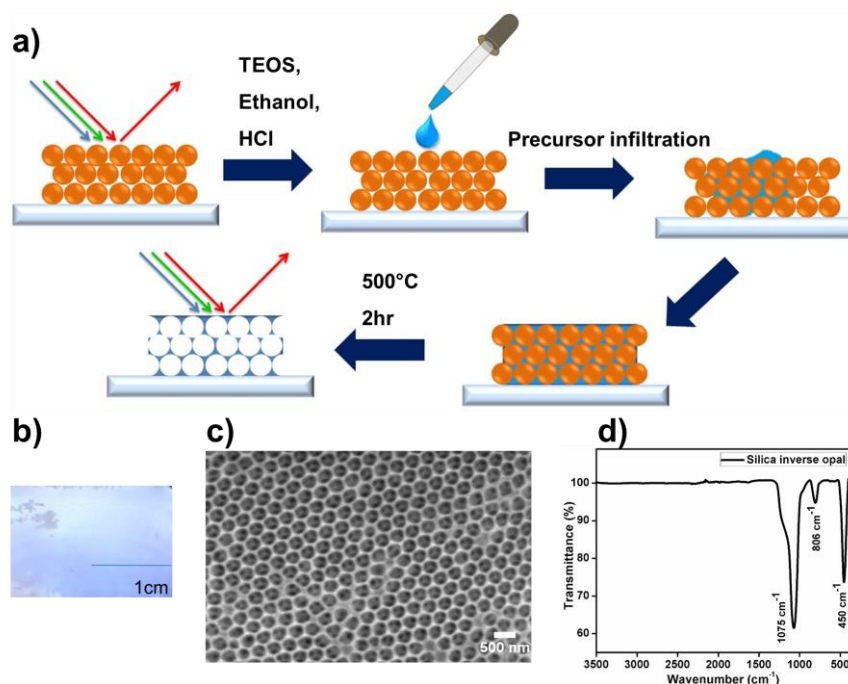


Fig. 2.14. a) Schematic representation of PS CPC based template fabrication of silica IO-PC, b) and c) represents digital photograph and SEM image of silica IO-PC respectively, and d) represents the FTIR spectra of silica IO-PC.

2.4.10. Optical properties of silica IO-PC powder

Unlike PS CPC, silica IO-PC is more stable and can be employed for higher temperature applications. Additionally, in PS CPCs, there is only physical contact among PS microspheres. Nevertheless, IO-PC has interconnected network structure, making the particles of the silica IO-PC powder more stable. Silica IO-PC was scratched out, subsequently lightly ground using a mortar and pestle into powder form. Photograph of silica IO-PC powder shown in fig. 2.15a shows that the powder is white in color. SEM image in fig. 2.15b and c reveal that the silica IO-PC powder consisted of particles having a wide range of size distribution. Further, to know more about the optical properties, we have taken the OM image and is shown in fig. 2.15d. OM image reveals the blue colored particles of silica IO-PC powder. Due to the changes in the orientation of particles of silica IO-PC powder, incident light is reflected in different directions, shown in the schematic representation in fig. 2.15e. Scattering of incident light in multiple directions dominates over the reflected light, and the IO-PC powder looks white to the naked-eye at all the viewing angle. However, the structural color of powder CPC was visible with OM.

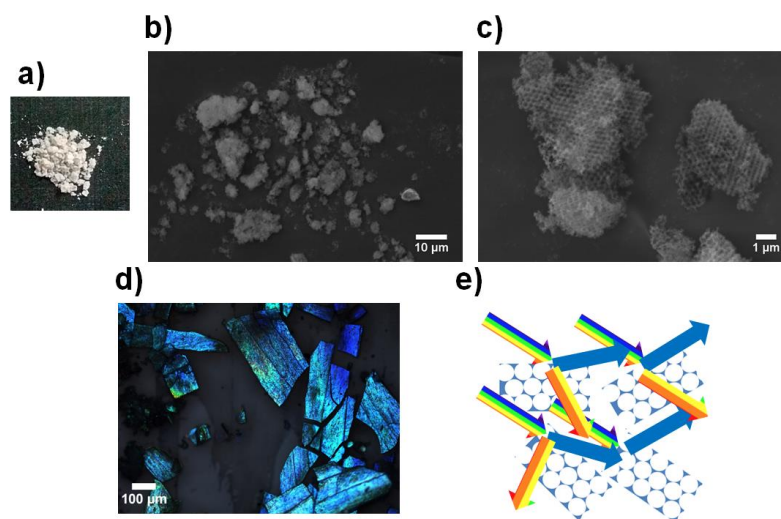


Fig. 2.15. a) photograph of silica IO-PC powder, b) and c) represents SEM image of silica IO-PC powder (Scale bar: 10 μm and 1 μm), d) represents OM image of silica IO-PC powder (Scale bar: 100 μm) and e) represents the schematic diagram showing reflection in silica IO-PC powder.

To impart the structural color to the IO-PC powder, we absorbed the scattered light with charcoal powder. It has already been reported that scattered light in CPCs can be absorbed using black particles. But they all utilized smaller nanoparticles as the background absorber for the scattered light (smaller than the microsphere used in CPC). When smaller particles enter into the voids of CPC or IO-PC, non-uniform particle distribution affects the periodicity in refractive index modulation. Further, it reduces the refractive index contrast, which decreases the brightness of structural color. Here we utilized charcoal, which is black (photograph in fig 2.16a) as the background absorber for scattered light. SEM image of charcoal in fig. 2.16b indicates flake-like morphology. Charcoal powder consisted of flakes of different sizes and which is larger (larger than 1 μm), and hence not able to enter into the pores of silica IO-PC (pore size of silica IO-PC was below 1 μm). Further, we mixed the charcoal with silica IO-PC powder using a mortar and pestle. When the weight % of charcoal was 4 %, we got a blue color for silica IO-PC powder (photograph in fig. 2.16c). Interestingly, the color of the powder was angle-independent. Low angle-dependent structural color is highly promising for display and sensing applications. Additionally, we increased the charcoal content to 8 weight % and which lead to a pale black appearance (photograph in fig. 2.16d). At higher weight % of charcoal, the reflected light was also absorbed. Fig. 2.16e represents the SEM image of the mixture of silica IO-PC powder and charcoal, which reveal that charcoal flakes act as a platform for absorbing scattered light. Schematic representation in fig. 2.16f depicts the coloration mechanism of the mixture of silica IO-PC and charcoal powder. When a light incident on silica IO-PC powder, due to the periodic arrangement, wavelength region at the PBG is reflected, and scattered light is absorbed by the black background (charcoal), giving structural color.

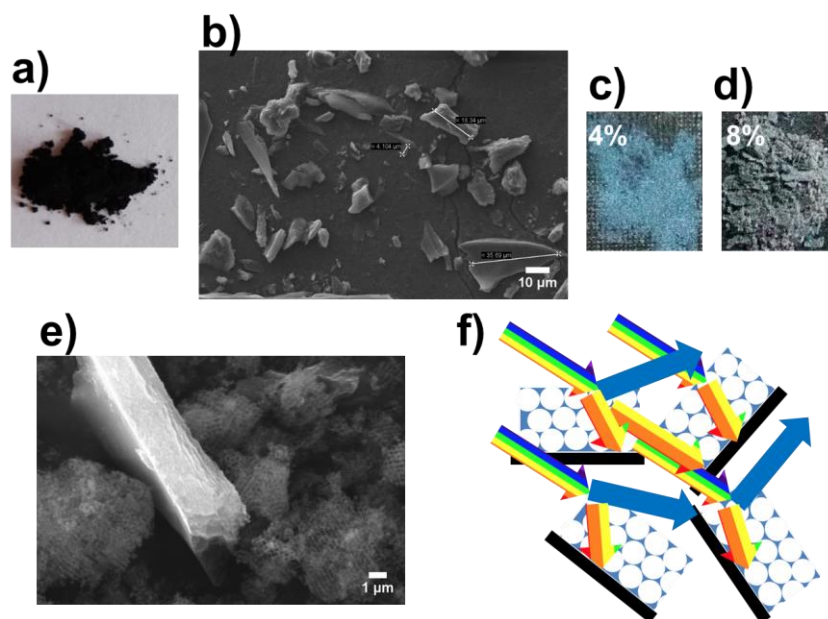


Fig. 2.16. a) Digital photograph and b) SEM image of charcoal powder respectively, c) and d) Digital photograph of 4 and 8 weight % charcoal containing silica IO-PC powder respectively, e) and f) SEM image of charcoal containing silica IO-PC powder and schematic representation of reflection in charcoal containing silica IO-PC powder.

2.5. Conclusion

In this chapter, highly monodispersed, stable PS microspheres colloid having high zeta potential and low PDI were synthesized by emulsion polymerization. Particle size was tuned by varying the monomer concentration. Further, PS CPC with long-range ordered structure was fabricated both on plasma-treated glass and flexible polymer substrates. PC CPCs on flexible polymer substrate was stable even under bending condition. The powder PS CPC was not structurally colored due to light scattering and the random orientation of particles in the powder. Additionally, silica IO-PC was fabricated using PS CPC as a sacrificial template and angle-independent structural colored silica IO-PC powder was prepared using charcoal as an absorber for scattered light.

References

1. E. Armstrong and C. O'Dwyer, *Journal of Materials Chemistry C*, 2015, **3**, 6109-6143.
2. Y. Zhao, Z. Xie, H. Gu, C. Zhu and Z. Gu, *Chemical Society Reviews*, 2012, **41**, 3297-3317.
3. J. Sun, B. Bhushan and J. Tong, *Rsc Advances*, 2013, **3**, 14862-14889.
4. L. Gonzalez-Urbina, K. Baert, B. Kolaric, J. Perez-Moreno and K. Clays, *Chemical reviews*, 2011, **112**, 2268-2285.
5. N. Vogel, M. Retsch, C.-A. Fustin, A. del Campo and U. Jonas, *Chemical reviews*, 2015, **115**, 6265-6311.
6. K. Zhong, P.-J. Demeyer, X. Zhou, O. Kruglova, N. Verellen, V. V. Moshchalkov, K. Song and K. Clays, *Journal of Materials Chemistry C*, 2014, **2**, 8829-8836.
7. E. Sowade, T. Blaudeck and R. R. Baumann, *Crystal Growth & Design*, 2016, **16**, 1017-1026.
8. J. Chen, P. Liu, X. Du and Z. Xie, *Langmuir*, 2018, **34**, 13219-13224.
9. S. Y. Leo, Y. Ni, C. Xu, Y. Zhang, Y. Dai, P. Qi, A. T. Xie, V. Basile, C. Taylor and P. Jiang, *Advanced Functional Materials*, 2017, **27**, 1703522.
10. Y.-L. Ko, H.-P. Tsai, K.-Y. Lin, Y.-C. Chen and H. Yang, *Journal of colloid and interface science*, 2017, **487**, 360-369.
11. H. He, M. Zhong, D. Konkolewicz, K. Yacatto, T. Rappold, G. Sugar, N. E. David, J. Gelb, N. Kotwal and A. Merkle, *Advanced Functional Materials*, 2013, **23**, 4720-4728.
12. P. Zhou, D. Zhou, L. Tao, Y. Zhu, W. Xu, S. Xu, S. Cui, L. Xu and H. Song, *Light: Science & Applications*, 2014, **3**, e209.
13. H. Li, J. Wang, F. Liu, Y. Song and R. Wang, *Journal of colloid and interface science*, 2011, **356**, 63-68.
14. E. Eftekhari, X. Li, T. H. Kim, Z. Gan, I. S. Cole, D. Zhao, D. Kielpinski, M. Gu and Q. Li, *Scientific reports*, 2015, **5**, 14439.

15. X. Jia, T. Zhang, J. Wang, K. Wang, H. Tan, Y. Hu, L. Zhang and J. Zhu, *Langmuir*, 2018, **34**, 3987-3992.
16. S. Y. Leo, W. Zhang, Y. Zhang, Y. Ni, H. Jiang, C. Jones, P. Jiang, V. Basile and C. Taylor, *Small*, 2018, **14**, 1703515.
17. Z. Cai, L. A. Luck, D. Punihaoale, J. D. Madura and S. A. Asher, *Chemical science*, 2016, **7**, 4557-4562.
18. H. Nam, K. Song, D. Ha and T. Kim, *Scientific reports*, 2016, **6**, 30885.
19. J. Hou, H. Zhang, B. Su, M. Li, Q. Yang, L. Jiang and Y. Song, *Chemistry–An Asian Journal*, 2016, **11**, 2680-2685.
20. Y. Li, X. Zhou, Q. Yang, Y. Li, W. Li, H. Li, S. Chen, M. Li and Y. Song, *Journal of Materials Chemistry C*, 2017, **5**, 4621-4628.
21. H. Cong, B. Yu, J. Tang, Z. Li and X. Liu, *Chemical Society Reviews*, 2013, **42**, 7774-7800.
22. Y. Xia, B. Gates, Y. Yin and Y. Lu, *Advanced Materials*, 2000, **12**, 693-713.
23. X. Ye and L. Qi, *Nano Today*, 2011, **6**, 608-631.
24. O. D. Velev and A. M. Lenhoff, *Current Opinion in Colloid & Interface Science*, 2000, **5**, 56-63.
25. M. Bardosova, M. E. Pemble, I. M. Povey and R. H. Tredgold, *Advanced Materials*, 2010, **22**, 3104-3124.
26. J. Zhang, X. Luo, X. Yan and G. Zhu, *Thin Solid Films*, 2010, **518**, 5204-5208.
27. Y. G. Ko, D. H. Shin, G. S. Lee and U. S. Choi, *Colloids and Surfaces A: Physicochemical and Engineering Aspects*, 2011, **385**, 188-194.
28. J. Kleinert, S. Kim and O. D. Velev, *Langmuir*, 2010, **26**, 10380-10385.
29. P. Liu, L. Bai, J. Yang, H. Gu, Q. Zhong, Z. Xie and Z. Gu, *Nanoscale Advances*, 2019, **1**, 1672-1685.
30. O. L. J. Pursiainen, J. J. Baumberg, H. Winkler, B. Viel, P. Spahn and T. Ruhl, *Opt. Express*, 2007, **15**, 9553-9561.
31. B. Hatton, L. Mishchenko, S. Davis, K. H. Sandhage and J. Aizenberg, *Proceedings of the National Academy of Sciences*, 2010, **107**, 10354-10359.
32. J. I. L. Chen, G. von Freymann, S. Y. Choi, V. Kitaev and G. A. Ozin, *Advanced Materials*, 2006, **18**, 1915-1919.

33. J. W. Galusha, C.-K. Tsung, G. D. Stucky and M. H. Bartl, *Chemistry of Materials*, 2008, **20**, 4925-4930.
34. Y. Zhang, L. Mu, R. Zhou, P. Li, J. Liu, L. Gao, L. Heng and L. Jiang, *Journal of Materials Chemistry C*, 2016, **4**, 9841-9847.
35. D. Wang, V. Salgueiriño-Maceira, L. M. Liz-Marzán and F. Caruso, *Advanced Materials*, 2002, **14**, 908-912.
36. R. C. Schroden, M. Al-Daous and A. Stein, *Chemistry of Materials*, 2001, **13**, 2945-2950.
37. V. P. Shrivastava, S. Sivakumar and J. Kumar, *ACS Applied Materials & Interfaces*, 2015, **7**, 11890-11899.
38. Z. Pan, J. Ma, J. Yan, M. Zhou and J. Gao, *Journal of Materials Chemistry*, 2012, **22**, 2018-2025.
39. P. Jiang, J. Bertone, K. S. Hwang and V. Colvin, *Chemistry of Materials*, 1999, **11**, 2132-2140.
40. E. Eftekhari, I. S. Cole and Q. Li, *Physical Chemistry Chemical Physics*, 2016, **18**, 1743-1749.
41. Y.-Q. Zhang, J.-X. Wang, Z.-Y. Ji, W.-P. Hu, L. Jiang, Y.-L. Song and D.-B. Zhu, *Journal of Materials Chemistry*, 2007, **17**, 90-94.
42. C.-Y. Hong, I. Drikis, S.-Y. Yang, H.-E. Horng and H.-C. Yang, *Journal of applied physics*, 2003, **94**, 2188-2191.

Chapter 3

**Fluorescence enhancement of dye by
tuning the photonic band gap and
host-guest complex formation**

3.1. Abstract

It is well-known that enhanced fluorescence of dye molecules can be achieved by the formation of host-guest complex that triggers the efficiency of chemical sensors, bio-imaging and photovoltaic devices. In this chapter, dual enhancement in fluorescence intensity has been demonstrated by tuning three-dimensional (3D) periodic architecture of colloidal photonic crystals (CPCs) and host-guest chemistry. CPC offers a seemingly platform with slow photon effect at the edges of photonic band gap (PBG). These photons with reduced group velocity facilitate enhanced excitation and light extraction which help in fluorescence enhancement, while the host-guest chemistry of rhodamine B (RhB) with cucurbit[7]uril (CB7) reduces aggregation caused quenching which provides an additional fluorescence enhancement. We validated augmentation of fluorescence intensity of a model dye, RhB using size-tuned polystyrene (PS) CPC films where RhB forms inclusion complex with the host, CB7. As compared to planar PS film (control sample), over 150-fold fluorescence enhancement has been achieved using monolithic CPC films. Our strategy for generating dual enhanced fluorescence can spur the ultra-sensitive detection capabilities of fluorescence-based chemical and biochemical sensors, providing stronger signal and lower limit of detection.

3.2. Introduction

Optical chemical sensors based on fluorescence are increasingly appealing due to its high sensitivity, selectivity, faster response time and technical simplicity. In this scenario, significant progress has been paved by designing novel molecules for fluorescent signal amplification to achieve increased sensitivity and lower limit of detection (LOD). Till date, various methods have been reported for fluorescence amplification. For example, Yuan *et al.* demonstrated photoinduced fluorescence enhancement in colloidal CdSeTe/ZnS core/shell quantum dots (QD).¹ Recently, Knoblauch *et al.* reported metal-enhanced fluorescence on silvered conical-bottom 96-well plate platform as a

potential diagnostic assay for enhanced detection of very low volumes of fluorophores.² In another work, Wang *et al.* studied surface plasmon resonance-enhanced fluorescence on core-shell Ag@SiO₂ nanoparticles concentrated in front of a nanochannel, for sensitive fluorescent determination of highly reactive oxygen species.³ In spite of these strategies, fluorescent signal amplification on colloidal photonic crystal (CPC) has set up a new avenue due to low cost and easy fabrication.⁴⁻⁶

Self-assembled CPCs are well-ordered periodic dielectric architecture of monodispersed inorganic/organic microspheres, providing brilliant structural color due to Bragg diffraction. A typical CPCs structure consists of periodic arrangement of colloidal microspheres and air voids. This periodically modulated refractive index in CPCs inhibits a spectral range of electromagnetic waves, viz. photonic bandgap (PBG) or photonic stopband. Apart from the fascination of structural color, the unique optical properties of CPCs offer a hallmark method to manipulate the direction of light propagation.⁷⁻⁹

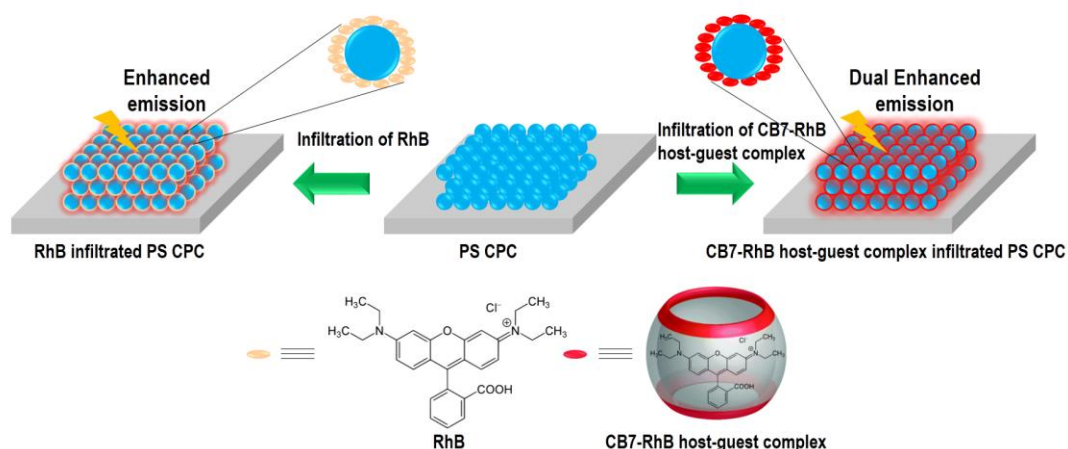
Slow photons at the blue and red edges of PBG are a workhorse to control fluorescence emission by overlapping PBG with excitation or emission of fluorophores. CPCs can either inhibit or enhance emission which is determined by fluorescence emission maxima and PBG minima.^{9,10} In practice, CPCs provide an expedient platform for fluorescence enhancement by tuning its leaky eigenmodes either with the fluorophore excitation or with the emission wavelength.⁹ Until now various strategies have been explored for further fluorescence enhancement on CPCs. For example, Wang and co-workers¹¹ have demonstrated a 162-fold enhancement of fluorescence signal on heterostructure CPCs with dual stopbands. Later, Li *et al.*⁹ reported 236-fold fluorescence enhancement on double-heterostructure CPC and recently, 230-fold enhancement of fluorescence emission was reported by using diffusion swelling method on CPC.¹² More recently, over 100-fold fluorescence enhancement was achieved based on a multiple heterostructure CPC with a super-wide stopband.¹³

In these methods, CPCs of different PBG layers were stacked over the other. The main advantage of such a structure is that both the excitation and emission wavelength of a fluorophore can overlap with the same CPC architecture with more than one PBG obtained using particles of different sizes. However, due to size mismatch, the stacked CPCs are not stable.

Indeed, most of the above strategies focus on the fabrication of complex CPC architectures, additional fluorescence enhancement by utilizing host-guest chemistry is not reported to the best of our knowledge. Despite the fact that PBG effect has been explored in the fluorescence enhancement, dye encapsulated cucurbituril (CB, host molecule) complex on CPC can offer further enhancement in fluorescent intensity. Cucurbituril, a pumpkin-shaped macrocyclic host, has emerged with its intriguing binding affinities of guest molecules in their hydrophobic cavity.¹⁴⁻¹⁸ The host-guest complexes of CBs impart higher stability both in solution and on a solid surface. For example, it is demonstrated that guest molecules such as styryl dye, rhodamine 6G and spermine are stable in solution, and rhodamine B, ferrocene, and viologens are stable even on solid surfaces.¹⁹⁻²⁴ It is reported that encapsulated fluorescent dye within CB cavity exhibits remarkable changes in photophysical properties. CB has been widely used as a supramolecular host to form an inclusion complex for fluorescence enhancement of the guest molecules. For example, the encapsulation of anilinoanthracene sulfonates into cucurbit[7]uril, (CB7) resulted in a 25-fold enhancement in fluorescence intensity.²⁵ Host-guest complex formation of CB7 with berberine in aqueous solution resulted in a 500-fold increase in fluorescence intensity.²⁶ Addition of cucurbit[10]uril, (CB10) to iridium polypyridyl complex resulted in a 40-fold enhancement in luminescence intensity.²⁷

In this work, we demonstrated dual enhanced fluorescence by the coalesced effect of dye encapsulated CB7 and monolithic 3D polystyrene (PS) CPCs. A schematic illustration depicting the method adopted for fluorescence

enhancement of a model dye, RhB is shown in Scheme 3.1. Firstly, the fluorescence intensity of RhB is amplified using PS CPC films. Further, additional fluorescence enhancement of RhB has been achieved by the introduction of the host-guest complexation of RhB (guest) with CB7 (host) molecules. The method adopted here is simple by the use of host-guest chemistry in combination with PS CPCs that provide over 150-fold fluorescence enhancement without the use of any intricate methods.



Scheme 3.1. Schematic illustration of the method adopted for fluorescence enhancement.

3.3. Experimental

3.3.1. Materials

Styrene, rhodamine B (RhB), and cucurbit[7]uril (CB7) were purchased from Sigma-Aldrich (India). Sodium dodecyl sulfate (SDS) and potassium persulfate (KPS) were purchased from Merck (India). For all the experiments ultrapure deionized water (18.2 M Ω .cm, 25 °C, Milli-Q D3, Merck) was used.

3.3.2. Synthesis of polystyrene (PS) microspheres and fabrication of PS CPCs

Monodispersed PS microspheres of varying particle sizes were synthesized as reported elsewhere²⁸ and the colloidal suspension was purified by centrifugation. Briefly, 100 mL of DI water was taken in a three-neck round

bottom flask. A certain amount of sodium dodecyl sulfate (SDS) as an emulsifier, potassium persulfate (KPS) as initiator was added with stirring under N₂ gas atmosphere and was heated to 75 °C in an oil bath for 15 min. Then, a certain amount of styrene was added dropwise and the reaction mixture was kept at a constant stirring of 350 rpm and temperature of 75 °C for 9 h to get monodispersed PS colloid. Glass coverslips were cleaned by sonication consecutively in ethanol, toluene and again in ethanol for 15 min each followed by N₂ plasma treatment for 5 min to make the glass surface clean and hydrophilic. Monolithic PS CPCs were prepared on a cleaned glass substrate via evaporation induced vertical deposition method.²⁹ The PBG of CPC was tuned by varying the diameter of PS microspheres. The thickness of CPCs was controlled by varying the concentration (wt %) of PS colloids.

3.3.3. Preparation of CB7-RhB host-guest complex

Here, RhB was used as the model fluorescent dye. CB7-RhB host-guest complex having a different molar ratio of CB7 was prepared in water. Briefly, a certain volume of the appropriate molar concentration of aqueous RhB and CB7 solutions were mixed, ultrasonicated for 15 min to form inclusion complex and kept in dark condition. In all the cases, the concentration of RhB was 10⁻⁶ M and the fluorescence enhancement of RhB by CB7 was studied.

3.3.4. Preparation of fluorescent PS CPC films

To compare fluorescence intensities among PS CPC films, the number of dye molecules (number density) should be identical on all the samples. Hence, a circular spot of similar diameter (5 mm) were made on each film (before dye infiltration) to keep the identical number density of dye molecules. The periphery of the circular spot was made hydrophobic using PAP pen in order to keep the solution within the circular spot during dye infiltration. An equal volume (1.5 μl) of 10⁻⁶ M RhB or CB7-RhB host-guest complex of different molar ratios in water was infiltrated into the PS CPCs and dried under vacuum in a desiccator for overnight. Similarly, control samples were prepared using CPCs

films heated to 120 °C for two hours to obtain a planar PS film on the glass substrate. 1.5 μl of 10^{-6} M RhB was drop cast onto the control sample and dried in a desiccator.

3.3.5. Characterization

Arrangement of PS CPCs and particle size of PS microspheres were analyzed using a field-emission scanning electron microscope (FEI Nova NanoSEM 450). A thin layer of gold was sputtered on PS CPC films to avoid charging effect. UV-visible reflection spectra were recorded using a UV-visible spectrophotometer (UV-2600, Shimadzu). Fluorescence emission spectra were recorded using Spectrofluorimeter (Fluorolog - HORIBA JobinYvon Inc). The thickness of CPC was measured on Dektak XT profilometer (Bruker). The hydrodynamic particle size of PS microspheres was obtained by Dynamic Light Scattering (Nano ZS Malvern instrument). Fluorescence lifetime experiments were conducted using a Delta Flex modular time-correlated single-photon counting (TCSPC) spectrometer system.

3.4. Results and discussion

3.4.1. Fabrication of PS-based CPCs

To manifest fluorescence amplification via enhanced excitation or light extraction, PBG edge of CPC is required to match either with excitation or emission wavelength of the fluorophore. Slow photon at the blue and red edge of PBG (known as PBG effect or slow photon effect), can be used to increase the interaction of light with fluorophores. Here, we used CPCs made of PS microspheres and its PBG was tuned by varying the diameter of PS microspheres as described in Chapter 2. Briefly, PS microspheres of different particle sizes with narrow size distribution were prepared by emulsion polymerization and CPCs were fabricated using evaporation induced vertical deposition method (Chapter 2). Here we selected three CPCs having different structural colors and hence different PBGs. We selected CPCs having violet, green and orange

structural color and are named as violet CPC, green CPC and orange CPC, respectively. Photographs, SEM micrographs and reflectance spectra of all the CPCs were shown in fig. 3.1. The structural color of various CPCs and corresponding PBG positions are described in table 3.1. The obtained PBG (from reflectance spectra) of violet, green, and orange-colored CPC films at 414 nm, 559 nm and 599 nm, respectively. We selected CPCs of different PBG positions to study the effect of both surface area and PBG effect. Due to the existence of air-voids, PS CPCs that we used here is porous in structure, and hence CPCs have a larger surface area. Additionally, due to spherical shape, PS microspheres provide a large surface area. Notably, it is known that fluorescence intensity changed, when the surface area of the solid surface changed. Therefore, in order to study the effect due to surface area, we have included violet CPCs made of small particles. Violet CPC shows no PBG effect on the fluorescence intensity of the model dye rhodamine B (RhB), since the excitation and emission wavelength of RhB is very far from PBG. Green and Orange CPCs were selected to study the effect of PBG on fluorescence intensity of rhodamine B.

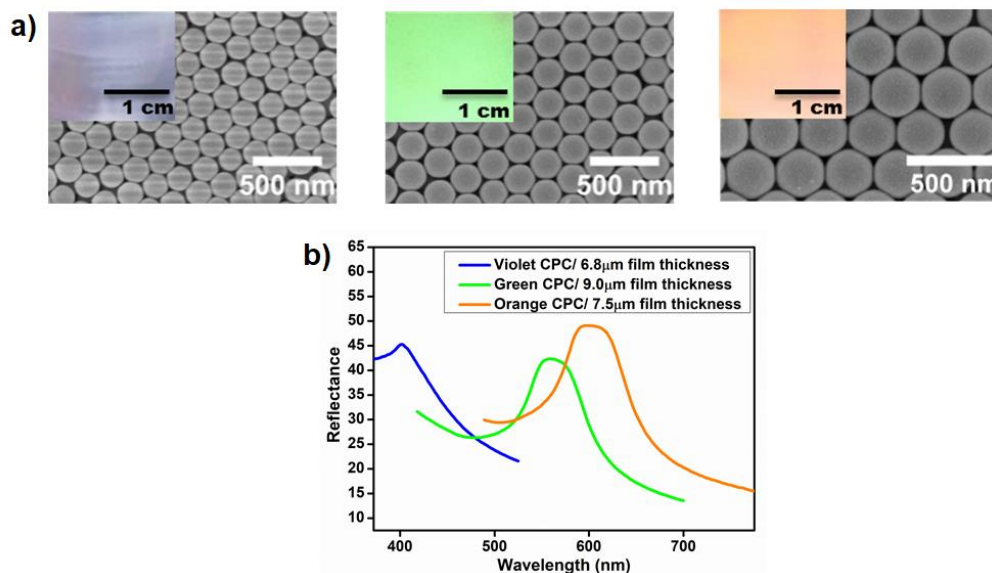


Fig. 3.1. a) SEM micrographs, corresponding digital photographs (inset) and b) reflectance spectra of violet, green and orange colored PS CPCs with film thickness of 6.8, 9.0 and 7.5 μm , respectively.

Table 3.1. Photonic band gap (PBG) positions (from reflectance spectra) of violet, green and orange colored PS CPCs.

Color of PS CPC	Experimental λ_{\max} (nm)
Violet	414
Green	559
Orange	599

The intensity of reflected light depends upon the thickness of the CPC. It is well-known that when the intensity of reflectance is changed the fluorescence intensity of the dye molecule on a CPC is also changed. To minimize the effect of variations in fluorescence intensity, we kept the thickness of all the CPCs similar and the thickness of PS CPC films was optimized for highest reflectivity. The thickness of CPC films was tuned by varying the concentration of the PS colloid. For each of the PS CPC films, the intensity of reflectance reached the maximum for a film thickness of around 6.7 μm . Therefore, in all the fluorescence enhancement studies we used CPC films of thickness about 6.7 μm to obtain maximum Bragg diffraction.

3.4.2. Fluorescence enhancement of RhB dyes on PS CPC

To investigate the effect of PBG, absorption and emission maxima of RhB dye from aqueous solutions were recorded. Fig. 3.2 shows the absorption and emission spectra of an aqueous solution of RhB (10^{-6} M). The spectra showed absorption maxima at 554 nm (absorption spectra) and emission maxima at 577 nm (fluorescence spectra) when excited at 518 nm.

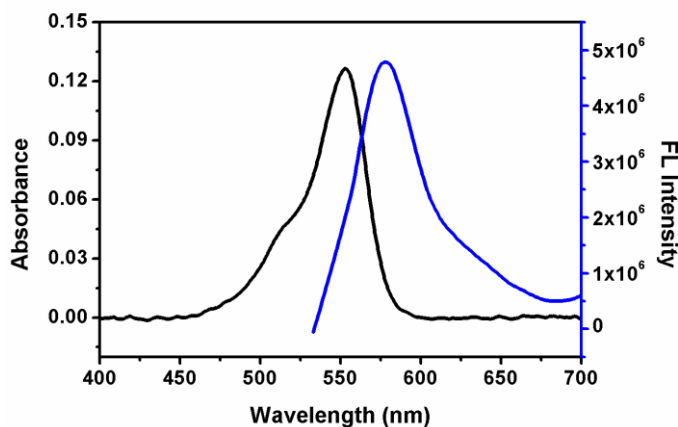


Fig. 3.2. a) Absorption and b) FL spectra of 10^{-6} M aqueous RhB solution.

To examine the effect of PBG on fluorescence intensity, PS CPCs films having different PBG and planar PS film as a control sample were prepared. The control PS film was prepared by heating PS CPC film at 120 °C for 2 h. For all fluorescence enhancement studies, planar PS films on glass substrate were used as the control sample for the comparison of fluorescence intensities with CPCs. The control sample was transparent and have no structural color, since it lacks the periodic arrangement for Bragg diffraction. By using PS in both control and PS CPC samples, variation in fluorescence intensity due to the effect of RhB-PS molecular interaction is kept minimal. The control PS sample has a planar structure and therefore used to understand the effect of PBG on PS CPC films that have curved surfaces. For the fluorescence enhancement studies, control PS film and PS CPCs of uniform thickness were used.

In order to keep the density of RhB molecules relatively identical in fluorescence enhancement studies, control PS film and PS CPC films were made to a circular spot of 5 mm diameter (schematic representation in fig. 3.3a) in and made hydrophilic using N_2 plasma for 5 min prior to dye infiltration. Since the area of the circular spot and the volume of dye solution used for drop casting are identical, the density of molecules in both the control sample and CPC film are the same. About 1.5 μ l of 10^{-6} M RhB solution was drop cast on the control

sample (planar PS film) and fluorescence intensity was measured by exciting at 518 nm. Fluorescence intensity (FL_{max}) recorded from five different areas of control PS film is shown in fig. 3.3b. We found that there is no significant variation in the fluorescence intensity indicating the more or less uniform distribution of RhB molecules in all the area of control PS film.

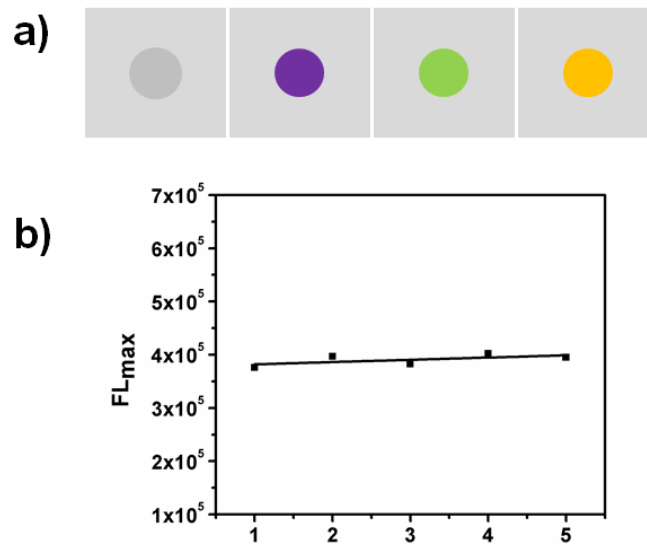


Fig. 3.3. a) Schematic representation of the control sample and all the CPC samples b) FL_{max} from different points of RhB coated control samples (PS).

In all fluorescence experiments RhB dye molecules were excited at 518 nm. Fluorescence spectra of RhB infiltrated PS CPC and the corresponding fluorescence enhancement factor (EF) calculated on various PS CPC films are shown in fig. 3.4 and fig. 3.6d, respectively. The fluorescence EF is calculated as the ratio of fluorescence intensity of RhB dye at 577 nm on different PS CPC films to that of RhB on control PS film. The fluorescence EF of RhB is found to be 24, 30 and 40 for violet, green and orange colored PS CPCs, respectively (fig. 3.6d). It is noteworthy that the PBG edge of violet colored PS CPC is neither at the excitation nor at the emission wavelength of RhB. However, the fluorescence intensity on violet colored PS CPC is relatively higher than the smooth PS control

film which is due to the large specific surface area of the 3D porous structure of PS CPC.

Our studies revealed that as compared to violet colored PS CPC, the fluorescence EF on green and orange colored PS CPCs was relatively higher. The blue edge of PBG of green and orange colored PS CPCs are near the excitation wavelength of RhB. Therefore, the fluorescence was amplified due to enhanced excitation owing to the photonic band edge effect. This indicates that the existence of PBG in green and orange colored PS CPCs leads to an additional fluorescence enhancement. The fluorescence EF in orange colored PS CPC is greater than that of green colored PS CPC due to the overlapping of emission of light with the blue edge of the PBG of orange colored PS CPC which resulted in higher fluorescence intensity. From the above observations, we inferred that fluorescence enhancement on green and orange colored PS CPC is higher than violet colored CPC due to PBG effect.

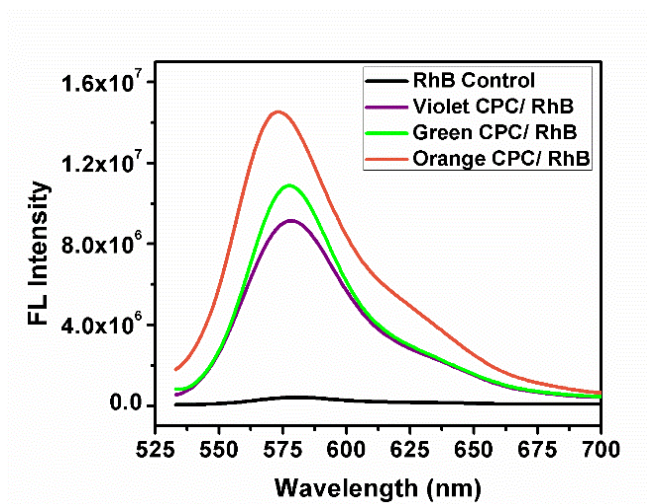


Fig. 3.4. Fluorescence spectra of RhB on violet, green and orange colored PS CPCs.

In order to affirm that the fluorescence EF is mainly contributed by PBG effect, we studied the fluorescence enhancement of methylene blue (MB) on violet, green and orange colored PS CPC. Here, MB was excited at 650 nm for all fluorescence enhancement studies. Table 3.2 shows the fluorescence EF of MB

on different PS CPCs. The fluorescence EF obtained was found to be 6, 7, and 10 for violet, green and orange colored PS CPCs, respectively, which is negligible, since neither the excitation wavelength nor the emission wavelength of MB is at the PBG edge of any of the CPCs. Compared to MB, the fluorescence EF of RhB was higher due to the overlap of excitation and emission wavelength with PBG in the case of RhB. Therefore, we could confirm that in the case of RhB infiltrated PS CPC, enhanced fluorescence is mainly due to PBG effect.

Table 3.2. Fluorescence enhancement factor of methylene blue on violet, green and orange colored CPCs.

Color of PS CPC	Fluorescence enhancement factor
Violet	6
Green	7
Orange	10

3.4.3. Host-guest complexation triggered enhanced fluorescence

Having understood the effect of PBG of PS CPCs on RhB emission, we further studied the fluorescence enhancement of RhB upon host-guest complex formation with CB7. From CB family, we selected CB7 for preparing host-guest complex with RhB. Owing to the molecular structure and size of RhB, the host CB7 cavity can accommodate a single molecule of RhB. The addition of CB7 to aqueous solutions of RhB facilitates the formation of the host-guest complex and resulted in significant changes in photophysical properties of dye molecules. Fig. 3.5a shows the absorption spectra of an aqueous solution of RhB (10^{-6} M) in the presence of different molar ratios of CB7 which indicate that absorption maxima remain almost constant irrespective of the CB7 concentration. Fig. 3.5b depicts

the fluorescence intensity (excitation wavelength at 518 nm) of aqueous RhB solution (10^{-6} M) in the presence of various molar ratio of CB7. There is a significant increase in fluorescence intensity with an increase in the molar ratio of CB7, which confirms the formation of CB7-RhB host-guest complex. Fluorescence intensity increases gradually till molar ratio of 1.5 and a further increase in CB7 concentration has no effect on fluorescence intensity. Compared to neat RhB, CB7-RhB host-guest complex of molar ratio, viz. 0.5, 1 and 1.5 showed 1.9, 2.5 and 6.7 fold fluorescence enhancement, respectively. Digital photographs (in daylight) of aqueous CB7-RhB host-guest complex of different molar ratios of Cb7 shown in fig. 3.5c, indicate a visible change in the intensity of RhB with an increase in CB7 concentration.

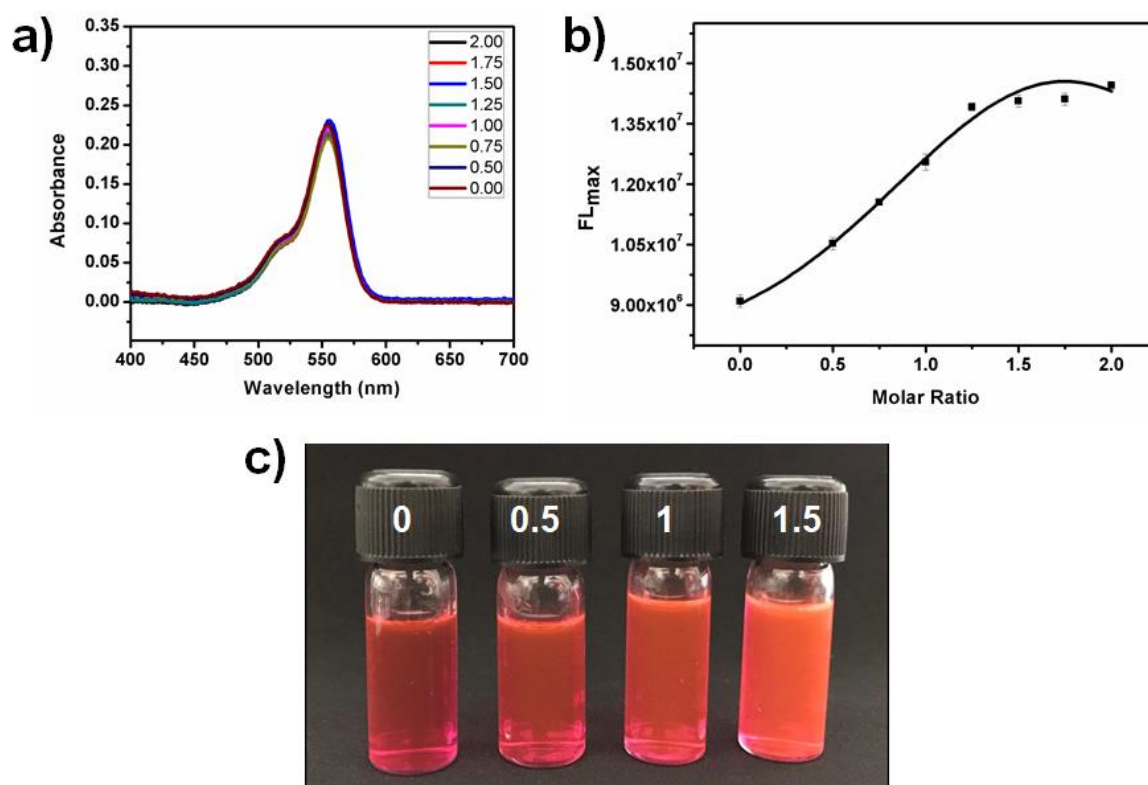


Fig. 3.5. a) Absorption spectra of 10^{-6} M aqueous solution of RhB in the presence of various molar ratio of CB7 b) FL maxima of 10^{-6} M aqueous solution of RhB in the presence of various molar ratio of CB7 and c) Digital photographs of aqueous solution of RhB in the presence of various molar ratio of CB7.

3.4.4. Host-guest complexation and PBG effect triggered enhanced fluorescence

Further, the fluorescence intensity of RhB encapsulated CB7 complex was amplified using 3D PS CPC and evaluated the augmented fluorescence intensity due to PBG effect. Fluorescence spectra of CB7-RhB host-guest complex formed using three molar ratios of CB7 (0.5, 1 and 1.5-abbreviated as CB-RhB₁, CB-RhB₂ and CB-RhB₃, respectively) on various PS CPCs and the control sample (RhB on control PS film) excited at 518 nm, are shown in fig. 3.6.a, b and c. Here, RhB encapsulated CB7 infiltrated PS CPC films exhibited significant enhancement in the fluorescence intensity than both control PS sample and RhB (without CB7 host) infiltrated PS CPC samples. Fig. 3.6.d shows the fluorescence EF of RhB alone, CB-RhB₁, CB-RhB₂ and CB-RhB₃ on violet, green and orange colored PS CPCs. In all the cases, fluorescence EF increases with an increase in the molar ratio of CB7 and particularly, orange colored PS CPC showed the highest fluorescence intensity. We obtained the highest value of 190-fold for CB-RhB₃ on orange colored PS CPC. The fluorescence intensity of control PS film was the lowest since it has no PBG.

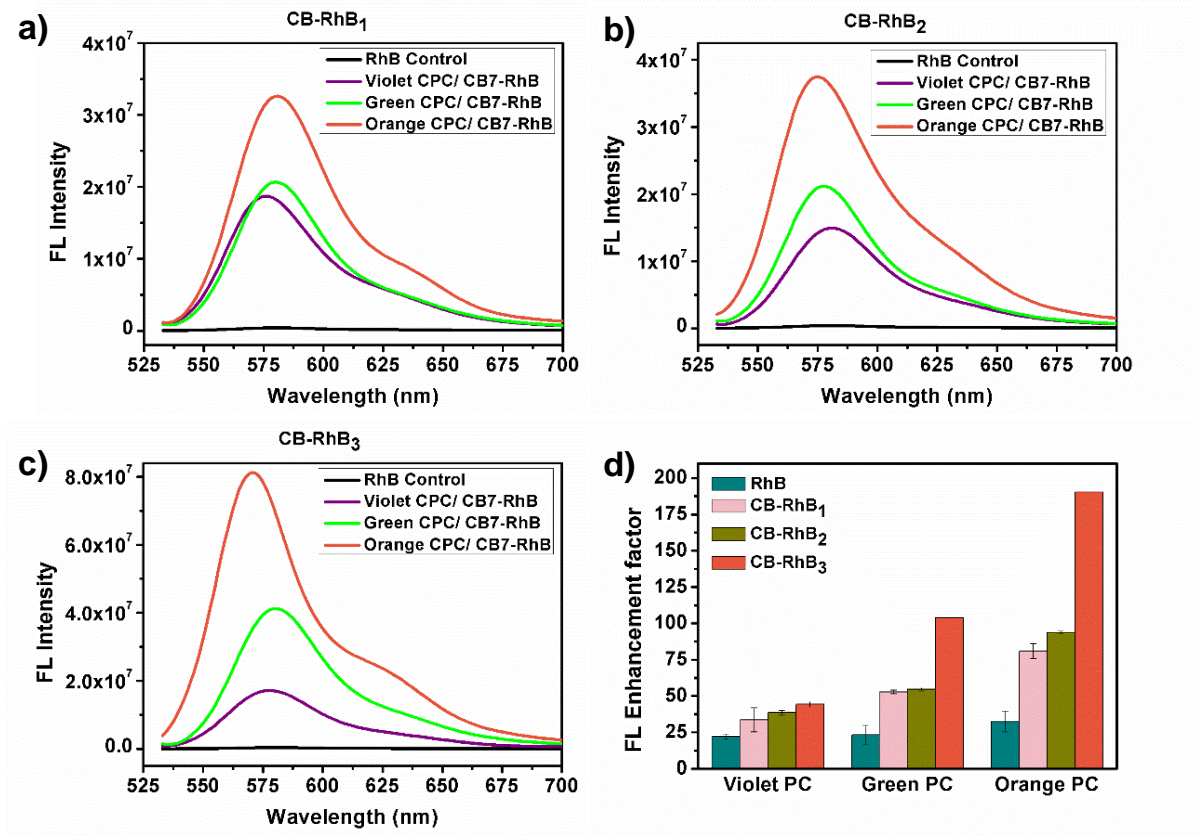
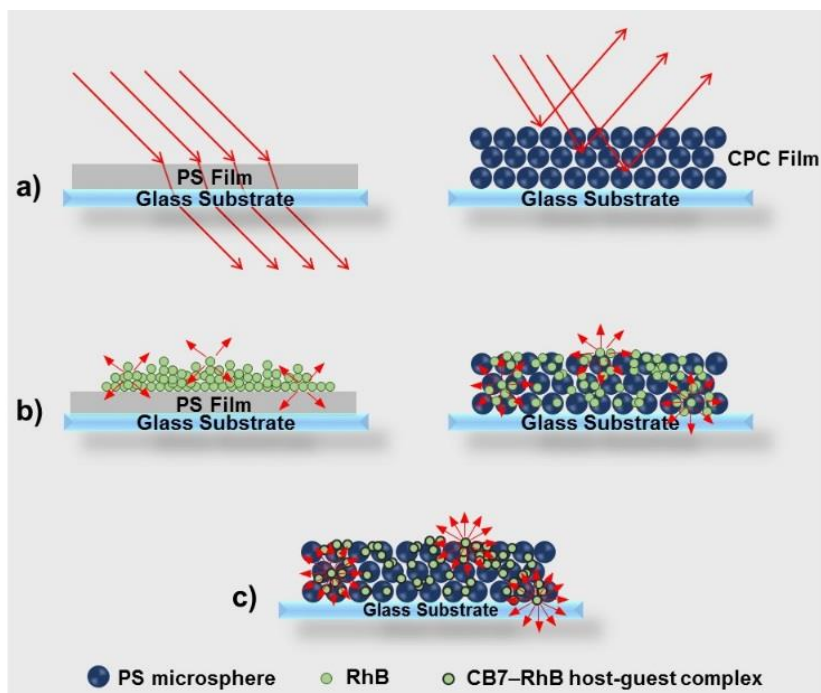


Fig. 3.6. Fluorescence spectra of CB7-RhB complex of different molar ratio of CB7 a) 0.5, b) 1, and c) 1.5 on various PS CPCs and d) Fluorescence enhancement factor of RhB, CB-RhB₁, CB-RhB₂ and CB-RhB₃ on violet, green and orange colored PS CPCs.

3.4.5. Mechanism of fluorescence enhancement

Based on the above studies, we propose the following mechanism for the fluorescence enhancement on PS CPCs (Scheme 3.2). It is obvious that most of the incident light is transmitted through the smooth PS film of control sample (Scheme 3.2a). On the other hand, in the case of CPCs, the incident light with wavelength region matching PBG is prohibited to propagate through it and thus reflected (Scheme 3.2a). Therefore, the number of RhB molecules excited is more on CPCs than on PS film which resulted in higher fluorescence intensity of emitted light (Scheme 3.2b). We observed that fluorescence intensity on each PS CPCs with different structural color and PBG was amplified in different extend. Among all, fluorescence intensity on green and orange colored PS CPCs were

higher compared to that of violet colored PS CPC. This could be due to the effect that PBG edge of violet colored PS CPC overlap neither with the excitation nor with the emission wavelength of CB7-RhB complex. Nonetheless, the fluorescence intensity of violet colored PS CPC is higher than that of the control PS films. This is due to the light scattering mechanism of PS microsphere particles with close-packed concave surface morphology in the lateral direction as compared to the planar PS film. In contrast, the PBG blue edge of green and orange colored PS CPC matches with the excitation wavelength. It is reported that absorption of photon near the blue edge of PBG facilitates enhanced light-matter interactions due to the localized density of states (LDOS) and spontaneous emission is enhanced, since LDOS is increased away from PBG.⁴ At the blue and red edges of PBG, photons propagate with reduced group velocity. These slow photons help in enhanced optical absorption. Remarkably, fluorescence EF on orange colored PS CPC is higher than that of green PS CPC, since the blue edge of PBG of orange colored PS CPC couple with the emission wavelength causing enhanced extraction. Fluorescence EF of CB7-RhB complex on PS CPC shown in fig. 3.6d reveals that the fluorescence intensity can be further increased by host-guest complex formation, since all the CB7-RhB complex on CPC that we studied here showed better EF than RhB on PS CPC. We observed that the fluorescence intensity on PS CPCs increases with increase in molar ratio of CB7, which facilitates more CB7-RhB complex formation.



Scheme 3.2. Schematic representation of mechanism of fluorescence enhancement of RhB and CB7-RhB host-guest complex on PS CPC films.

In order to confirm the fluorescence enhancement of RhB by the encapsulation within CB7 cavity and to know the contribution of host-guest complex effect, we measured fluorescence intensity of CB7-RhB complex of different molar ratio of CB7 on planar PS films. Fluorescence spectra shown in fig. 3.7a revealed that fluorescence intensity increases with an increase in the molar ratio of CB7. Fluorescence EF of CB-RhB₁, CB-RhB₂ and CB-RhB₃ on planar PS film with respect to RhB on planar PS film shown in fig. 3.7b indicate that fluorescence EF increases with increases in the molar ratio of CB7. We obtained two-fold enhancement for CB-RhB₃ on planar PS CPC film. However, fluorescence EF value obtained using planar PS film was lower compared to that of PS CPC films which is due to the absence of PBG effect and fluorescence enhancement found in planar PS film is contributed by host-guest complex formation. Further, we examined the role of CB7 on fluorescence life-time to understand more about fluorescence enhancement. Fluorescence decay curve for RhB and CB-RhB₃ on planar PS film is shown in fig. 3.7c and; life-time constants

and relative percentages are displayed in Table 3.3. Interestingly, the average fluorescence lifetime of CB-RhB₃ (73 ns) on planar PS film was higher than that of RhB (37 ns), which reveals that the formation of host-guest complex facilitates higher fluorescence intensity. The encapsulated RhB molecules within CB7 cavity experiences a more hydrophobic environment. Geometrical confinement within CB7 cavity facilitates RhB molecule to get chemically isolated from the surroundings (Scheme 3.2c). Additionally, de-aggregation of dye molecules by the formation of host-guest chemistry significantly reduces aggregation caused by quenching (Scheme 3.2c). However, in the case of RhB infiltrated sample, aggregation of the dye molecule is more likely. In order to understand the contribution of PBG effect, we kept the effect due to host-guest complex minimal in fluorescence enhancement calculation by considering CB-RhB₁, CB-RhB₂ and CB-RhB₃ coated planar PS film as control sample for corresponding CPC films and the fluorescence EF is shown in fig. 3.7d. Fluorescence EF values were lower compared to those calculated using RhB (without CB encapsulation) coated planar PS film as control sample. Here, the main contribution for fluorescence enhancement is due to PBG effect except in the case of violet colored CPC film in which fluorescence enhancement is due to large surface area. We obtained the highest value of 96-fold for CB-RhB₃ on orange colored PS CPC by minimizing the effect of host-guest complex in fluorescence EF calculation. It implies that host-guest complex formation in CB-RhB₃ makes the fluorescence EF value from 96 to 190, which is about 2 times higher when RhB coated planar PS film is used as control sample. Fluorescence EF of RhB on orange colored CPC film was 40 (fig.3.6) and further enhanced to 190 which is about 5 fold by the combined effect of PBG and host-guest formation. Thus, the combined effect of PBG and host-guest complex formation help to achieve higher fluorescence EF.

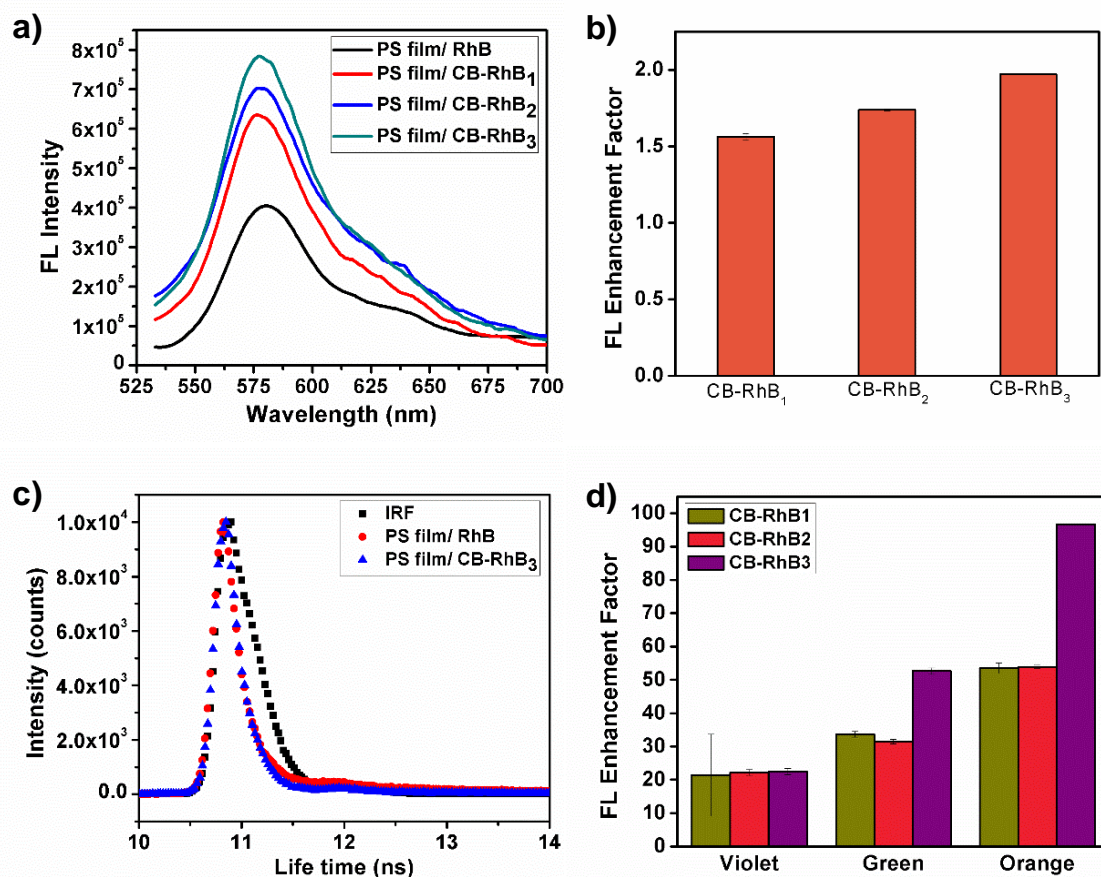


Fig. 3.7. a) Fluorescence spectra of RhB and CB-RhB₁, CB-RhB₂ and CB-RhB₃ on planar PS film b) Fluorescence enhancement factor of CB-RhB₁, CB-RhB₂ and CB-RhB₃ with respect to RhB coated/ planar PS film c) Fluorescence decay curves of RhB and CB-RhB₃ on planar PS film and d) Fluorescence enhancement factor of CB-RhB₁, CB-RhB₂ and CB-RhB₃ on violet, green and orange colored CPC films, calculated using host-guest complex coated planar PS film of corresponding molar ratio as control sample.

Table 3.3. Fluorescence lifetime T_i , relative percentage (in parenthesis) and average life-time T_{Av} of RhB and CB-RhB₃ on planar PS film.

	T₁ (ns)	T₂ (ns)	T₃ (ns)	T_{Av} (ns)
RhB on PS film	37.17 (49.92)	37.01 (50.07)	-	37.09
CB-RhB₃ on PS film	71.36 (37.19)	75.86 (12.83)	72.56 (49.98)	72.52

3.5. Conclusion

In summary, this chapter describes successful demonstration of augmented fluorescence enhancement of guest dye molecule by the incorporation of a macrocycle-based host-guest complex into monolithic 3D CPCs having different PBG. Slow photon near the PBG of CPC facilitates enhanced light-matter interaction, while CB7 helps in preventing aggregation-induced self-quenching of RhB. Thus, the synergistic effect of the macrocyclic host, CB7 and highly ordered structure of CPC significantly contribute to achieving over 150-fold fluorescence enhancement of RhB. Importantly, the host-guest complex formation may decrease the quantum yield of photobleaching. This approach could be extended to highly sensitive fluorescence-based detections such as chemical and biochemical sensing.

References

1. C. T. Yuan, W. C. Chou, D. S. Chuu, Y. N. Chen, C. A. Lin and W. H. Chang, *Applied Physics Letters*, 2008, **92**, 183108.
2. R. Knoblauch and C. D. Geddes, *Nanoscale*, 2019, **11**, 4337-4344.
3. H.-S. Wang, C. Wang, Y.-K. He, F.-N. Xiao, W.-J. Bao, X.-H. Xia and G.-J. Zhou, *Analytical Chemistry*, 2014, **86**, 3013-3019.

4. P. Lodahl, A. Floris van Driel, I. S. Nikolaev, A. Irman, K. Overgaag, D. Vanmaekelbergh and W. L. Vos, *Nature*, 2004, **430**, 654.
5. J. I. L. Chen, G. von Freymann, S. Y. Choi, V. Kitaev and G. A. Ozin, *Journal of Materials Chemistry*, 2008, **18**, 369-373.
6. X. Su, X. Sun, S. Wu and S. Zhang, *Nanoscale*, 2017, **9**, 7666-7673.
7. S. John, *Physical Review Letters*, 1987, **58**, 2486-2489.
8. E. Yablonovitch, *Physical Review Letters*, 1987, **58**, 2059-2062.
9. E. Eftekhari, X. Li, T. H. Kim, Z. Gan, I. S. Cole, D. Zhao, D. Kielpinski, M. Gu and Q. Li, *Scientific Reports*, 2015, **5**, 14439.
10. C. Vion, C. Barthou, P. Bénalloul, C. Schwob, L. Coolen, A. Gruzintev, G. Emel'chenko, V. Masalov, J.-M. Frigerio and A. Maître, *Journal of Applied Physics*, 2009, **105**, 113120.
11. H. Li, J. Wang, F. Liu, Y. Song and R. Wang, *Journal of Colloid and Interface Science*, 2011, **356**, 63-68.
12. E. Eftekhari, I. S. Cole and Q. Li, *Physical Chemistry Chemical Physics*, 2016, **18**, 1743-1749.
13. L. Zhang, J. Wang, S. Tao, C. Geng and Q. Yan, *Advanced Optical Materials*, 2018, **6**, 1701344.
14. J. Kim, I.-S. Jung, S.-Y. Kim, E. Lee, J.-K. Kang, S. Sakamoto, K. Yamaguchi and K. Kim, *Journal of the American Chemical Society*, 2000, **122**, 540-541.
15. J.-X. Liu, L.-S. Long, R.-B. Huang and L.-S. Zheng, *Inorganic Chemistry*, 2007, **46**, 10168-10173.
16. C. Márquez, R. R. Hudgins and W. M. Nau, *Journal of the American Chemical Society*, 2004, **126**, 5806-5816.
17. N. Zhao, G. O. Lloyd and O. A. Scherman, *Chemical Communications*, 2012, **48**, 3070-3072.
18. K. I. Assaf and W. M. Nau, *Chemical Society Reviews*, 2015, **44**, 394-418.
19. M. Freitag and E. Galoppini, *Langmuir*, 2010, **26**, 8262-8269.
20. A. C. Gomes, C. I. R. Magalhães, T. S. M. Oliveira, A. D. Lopes, I. S. Gonçalves and M. Pillinger, *Dalton Transactions*, 2016, **45**, 17042-17052.

21. R. L. Halterman, J. L. Moore and W. T. Yip, *Journal of Fluorescence*, 2011, **21**, 1467-1478.
22. D. A. Ivanov, N. K. Petrov, E. A. Nikitina, M. V. Basilevsky, A. I. Vedernikov, S. P. Gromov and M. V. Alfimov, *The Journal of Physical Chemistry A*, 2011, **115**, 4505-4510.
23. S. K. Kim, K. M. Park, K. Singha, J. Kim, Y. Ahn, K. Kim and W. J. Kim, *Chemical Communications*, 2010, **46**, 692-694.
24. L. Mingzhu, H. Fang, L. Qing, L. Jian, X. Liang, J. Lei, S. Yanlin, W. Shu and Z. Daoben, *Angewandte Chemie International Edition*, 2008, **47**, 7258-7262.
25. B. D. Wagner, N. Stojanovic, A. I. Day and R. J. Blanch, *The Journal of Physical Chemistry B*, 2003, **107**, 10741-10746.
26. M. Megyesi, L. Biczók and I. Jablonkai, *The Journal of Physical Chemistry C*, 2008, **112**, 3410-3416.
27. L. R. Alrawashdeh, A. I. Day and L. Wallace, *Dalton Transactions*, 2013, **42**, 16478-16481.
28. Z. Pan, J. Ma, J. Yan, M. Zhou and J. Gao, *Journal of Materials Chemistry*, 2012, **22**, 2018-2025.
29. P. Jiang, J. F. Bertone, K. S. Hwang and V. L. Colvin, *Chemistry of Materials*, 1999, **11**, 2132-2140.
30. Y.-Q. Zhang, J.-X. Wang, Z.-Y. Ji, W.-P. Hu, L. Jiang, Y.-L. Song and D.-B. Zhu, *Journal of Materials Chemistry*, 2007, **17**, 90-94.
31. C.-Y. Hong, I. Drikis, S. Y. Yang, H. E. Horng and H. C. Yang, *Journal of Applied Physics*, 2003, **94**, 2188-2191.

Chapter 4

Aptasensor based on stimuli-responsive photonic crystals of core-shell microspheres for pesticide detection

4.1. Abstract

Stimuli-responsive photonic crystals are able to alter their Photonic band gap (PBG) via changes in lattice spacing upon exposure to external stimuli. In the context of optical sensing, stimuli-responsive PCs (RPCs), having low angle-dependent structural color is highly recommended. In the present chapter, an aptasensor based on stimuli-responsive photonic crystals (RPC-A) of core-shell microspheres having low angle-dependent structural color is demonstrated for the selective detection of an organophosphorous pesticide (omethoate). Herein, we synthesized core-shell microspheres of polystyrene@poly(methyl methacrylate-ethylene glycol dimethacrylate-acrylic acid) [PS@poly(MMA-EGDMA-AA)] for the colloidal photonic crystal (CPC) fabrication. The RPC was made selective for pesticide binding using single-stranded DNA-aptamer as the recognition probe. Omethoate selective aptamer sequence was selected and covalently attached to poly(MMA-EGDMA-AA) hydrogel shell via EDC-NHS chemistry. Unlike the conventional hydrogel-based RPCs comprising inverse opal PC, microgel based PC, polymerized crystalline colloidal array, etc., herein, we prepared RPCs of core-shell (CS) microspheres embedded in polyvinyl alcohol (PVA) matrix. Generally, a CPC becomes responsive by the swelling and deswelling of hydrogel. However, the swelling/deswelling of hydrogel on a non-expandable glass substrate offer poor structural stability to conventional RPCs, thus limiting its practical application in various technologically relevant areas such as sensing, anti-counterfeiting, and color display. The RPC developed in the present study with microspheres embedded in PVA matrix is structurally stable towards analyte solution. The specific binding of omethoate with single-stranded DNA-aptamers cause shrinkage of poly(MMA-EGDMA-AA) hydrogel shell and thereby, the corresponding shift in Bragg diffraction spectra can be used for the detection of a wide concentration range of omethoate.

4.2. Introduction

To increase the agricultural production, pesticides play a significant role. Unfortunately, environmental pollution and human health risks caused by pesticide residues present in fruits and vegetables due to its overuse is an ever-present threat.

Among various pesticides, organophosphorus pesticides are one of the commonly used pesticides and the presence of its residues is lethal to the living things. Omethoate is an organophosphorus pesticide which is used as an effective pest control for vegetables, fruits, and crops. The environmental and health concerns have increased the demand for developing low cost and fast detection methods with high selectivity and sensitivity. To date, various approaches have been developed for pesticide detection. For example, Catalá-Icardo *et al.* has used liquid chromatography for the simultaneous determination of several organothiophosphorus pesticides.¹ Sun *et al.* used acetylcholinesterase biosensor based on prussian blue-modified electrode for detecting organophosphorous pesticides.² Huang *et al.* used a sensitive fluorescence assay of organophosphorus pesticides using acetylcholinesterase and copper-catalyzed click chemistry.³ However, all these methods demand more time, sophisticated instrumentation and skilled personnel. Again, these methods are suitable for the detection of a particular class of pesticides and hence not applicable for the detection of a selected pesticide.

Interestingly, aptamer-based sensors attracted significant attention due to high selectivity. Aptamers are single-stranded oligonucleotides obtained by *in-vitro* selection or systematic evolution of ligands by exponential enrichment (SELEX).⁴ They are used as a recognition probe in a variety of sensors as they have several advantages over the existing biosensors utilizing natural receptors such as enzymes and antibodies. Aptamers have shorter generation time and lower costs. Aptasensors, the sensors based on aptamers have high recognition ability and high affinity to target specific molecules. Moreover, aptasensors for a variety of pesticides have been already reported.^{5,6} For example, Zhang *et al.* reported fluorescence determination of omethoate with omethoate aptamer.⁷ Pang *et al.* developed a single aptamer-based Surface Enhanced Raman Scattering method for rapid detection of multiple pesticides.⁸ To address some of the disadvantages of existing sensors, we have developed a photonic crystal (PC) based aptasensor.

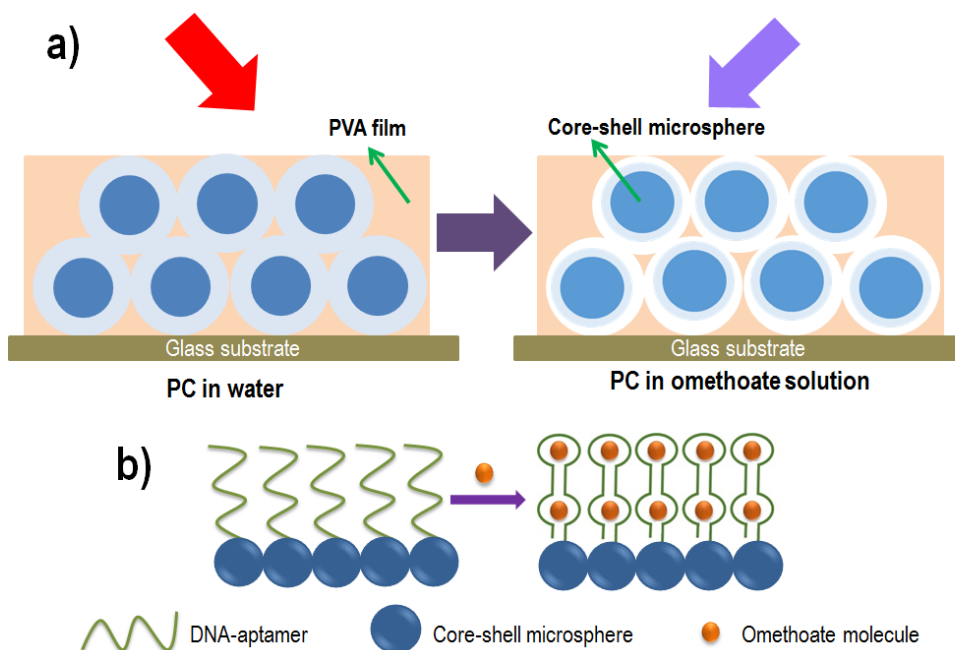
Recently, stimuli-responsive color changing materials of PCs, namely responsive PCs (RPCs) have emerged as potential sensors with its low cost and easy fabrication method. RPCs for sensing various analytically important stimuli such as temperature,^{9,10} pressure,^{11,12} humidity,¹³ pH,¹⁴ solvent,¹⁵ glucose,^{16,17} protein,¹⁸ surfactants,¹⁹ and ions²⁰

has already been reported. In this context, hydrogels are an important class of stimuli-responsive component in RPCs, since they can undergo volume phase transition (swelling/deswelling) by external stimuli. The stimuli-responsive color changing in hydrogel based RPCs rely on swelling induced variation in lattice spacing of PC structure. Depending upon the changes in lattice spacing (increase or decrease), RPCs exhibit blue or red shift in photonic band gap (PBG) position and the corresponding changes in structural color endow label-free naked-eye detection of analyte molecules. For example, Ye *et al.* developed aptamer-functionalized colloidal PC hydrogel for the screening of heavy metal ions.²¹ The specific binding of heavy metal ions, such as Hg²⁺ and Pb²⁺, to single-stranded aptamers in the hydrogel network caused the hydrogel to shrink, and which results in blue shift in the Bragg diffraction peak position. In another work, Pan *et al.* made a visually detectable RPC having polyacrylamide inverse opal hydrogel (IOH_{PAM}) using polystyrene (PS) CPC as a template.²² IOH_{PAM} changed its periodicity in the arrangement in response to alcohols with different structures, chain lengths and concentrations thus underwent fast and drastic changes in its structural color and a corresponding displacement in the reflectance spectra. Several types of architectures such as microgel PC,²³ inverse opal PC,²⁴ polymerized crystalline colloidal array,²⁵ and core-shell microsphere-based PC²⁶ has been explored for RPC fabrication. Among them, core-shell microsphere-based RPCs have superior properties since they exhibit the features of both shell and core. Meanwhile, the rigid core provides structural stability and the stimuli-responsive hydrogel shell can provide additional functionality. However, core-shell RPC based aptasensor for pesticide detection has not been reported so far to the best of our knowledge.

Colloidal photonic crystal (CPC) of colloidal microspheres can be easily fabricated through colloidal self-assembly and they possess an orderly arranged close-packed structure.^{27,28} Depending upon the degree of order in the arrangement of the colloidal microspheres, colloidal self-assembly can generate photonic crystalline structures²⁹ or photonic amorphous structures.²⁹ In detail, periodically ordered photonic structures exhibit angle-dependent structural color due to the anisotropic nature of their microscopic structure, whereas disordered photonic structure exhibit angle-independent structural color due to the isotropic nature of their microscopic structure.²⁹

In the context of optical sensing, low angle-dependent structural color is highly recommended. Herein, a low angle-dependent structural color shifting photonic crystals of PS@poly(MMA-EGDMA-AA) core-shell microsphere with a long-range periodic arrangement of the microspheres, but having short-range order of core and shell has been prepared.

Herein, we present an efficient strategy for the preparation of CPCs of core-shell microspheres, and RPC based aptasensor has been developed for omethoate detection. In order to avoid the brittle nature of RPC, the core-shell microspheres were self-assembled in PVA matrix. Omethoate selective aptamer was functionalized on to the carboxylic functional group of hydrogel shell via EDC-NHS chemistry. A schematic illustration depicting the mechanism of omethoate sensing is shown in Scheme 4.1. During detection, omethoate molecules bind to single-stranded DNA aptamers in the hydrogel network, which leads to shrinking of hydrogel shell and the resultant blue shift of Bragg diffraction peak can be used for the analyte sensing.



Scheme 4.1. Mechanism of omethoate sensing using core-shell microsphere RPC: a) Shrinking of hydrogel shell in the presence of omethoate and corresponding blue shift in Bragg diffraction and b) binding mechanism of omethoate with DNA-aptamer on the core-shell microsphere.

4.3. Experimental

4.3.1. Chemicals and materials

Single stranded-DNA aptamer for the selective binding of omethoate (AAG CTT GCT TTA TAG CCT GCA GCG ATT CTT GAT CGG AAA AGG CTG AGA GCT ACG C) was purchased from Eurofins Genomics India Pvt., Ltd. Styrene (Sigma-Aldrich, 99%), Acrylic acid, AA (Aldrich, 99%), Methyl methacrylate, MMA (Sigma-Aldrich, 99%), Ethylene glycol dimethacrylate, EGDMA (Sigma-Aldrich), N, N'-Methylenebis(acrylamide) (BIS), Potassium persulfate (Sigma-Aldrich, 98%). All pesticides (Omethoate, Methyl parathion and Carbofuran) and reagents were of analytical reagent grade and were purchased from Sigma-Aldrich. 1-Ethyl-3-(3-dimethylaminopropyl)carbodiimide, EDC (Fluka) and N-Hydroxysuccinimide, NHS (Aldrich) and Polyvinyl alcohol, PVA (Mw 31,000-50,000) was purchased from Sigma-Aldrich. Ultra-pure MilliQ water (18.2 mΩ cm) was used in all experiments.

4.3.2. Synthesis and self-assembly of monodispersed PS@poly(MMA-EGDMA-AA) core-shell microspheres

Monodispersed core-shell (CS) microspheres of PS@poly(MMA-EGDMA-AA) were synthesized by a modified emulsifier-free emulsion polymerization method. Briefly, 6.65 mmol of MMA, 4.62 mmol of AA, 0.56 mmol of EGDMA, 58.16 mmol of styrene, 0.212 mmol of BIS and 100 ml deionized water were taken in a round bottom flask. The reaction mixture was kept at 70 °C for 30 min. 73.9 mmol of aqueous potassium persulfate solution (KPS) was added dropwise and the polymerization was carried out at 80 °C for 10 h under N₂ gas atmosphere. The temperature and stirring speed were kept constant throughout the reaction. The CS microspheres were purified via centrifugation. Glass coverslips (substrate) for CPC fabrication were cleaned and made hydrophilic by N₂ plasma treatment for 5 min. Photonic crystals of CS microspheres (CS-RPC) were prepared via evaporation induced vertical deposition method.³⁰ For the fabrication of structurally stable, intact and orderly arranged CS microsphere assembly in the PVA matrix (PVA-RPC), CS microspheres were dispersed

in 0.2 weight % aqueous PVA solution and self-assembled onto hydrophilic glass substrate via evaporation induced vertical deposition method.

4.3.3. Fabrication of aptasensor based on RPC (RPC-A)

After being washed thoroughly with water, the carboxyl groups anchored on the CS microspheres of PVA-RPC were activated with EDC-NHS by immersion in 1 mL pH 6.0 MES buffer solution containing 0.5 mM EDC and 0.5 mM NHS for 30 min at room temperature. The activated PVA-RPC was washed several times with pH 6.0 PBS. 30 μ L of 200 nM aptamer solution was added and kept at room temperature for 30 min, followed by overnight refrigeration at 4 °C. After thoroughly washing with PBS buffer, the aptamer-functionalized PVA-RPC (aptasensor based on stimuli responsive photonic crystal, RPC-A) was obtained.

4.3.4. Characterization

The morphology, the diameter of the core and the thickness of the shell, of core-shell polymer microspheres were analyzed with FEI Tecnai 30 G2S-TWIN Transmission Electron Microscope (TEM). Microsphere self-assembly and periodicity of all the RPCs were analyzed using an EVO 18 Special Edition Scanning Electron Microscope, SEM (Carl Zeiss, Germany). The reflectance spectra of all the samples were recorded using a UV-Visible spectrophotometer (UV-2600, Shimadzu). X-ray Photoelectron Spectroscopy (XPS) data were collected using PHI 5000 Versa Probe II ULVAC-PHI Inc., USA equipped with micro-focused (200 μ m, 15 KV) monochromatic Al K α X-ray source ($h\nu = 1486.6$ eV). Survey scans were recorded with an X-ray source power of 50 W and pass energy of 187.85 eV. Narrow scans of the major elements were recorded at 46.95 eV pass energy. Data analysis and peak fitting of the XPS spectra were done using PHI's Multipak software. The carbon peak at 284.6 eV was used for the calibration of the XPS spectra. Fourier Transform-Infrared (FT-IR) spectra were obtained on a PerkinElmer FT-IR spectrometer. Dynamic Light Scattering (DLS) measurements were performed on a Zetasizer Nano ZS (Malvern Instruments). Thermogravimetric Analysis (TGA) thermograms were recorded in the heating process by using Thermal Analysis System (HITACHI, STA7300) under nitrogen gas atmosphere at a rate of 10 °C/min. Differential

Scanning Calorimetry (DSC) was used to acquire glass transition temperature (T_g) of the microspheres using Perkin Elmer Pyris 6 DSC at a heating rate of 10 °C/min. Photographs of all the samples were taken with Nikon D4 digital camera.

4.4. Results and Discussion

4.4.1. Synthesis of monodispersed PS@poly(MMA-EGDMA-AA) core-shell microspheres

Monodispersed core-shell (CS) microspheres were synthesized by a modified emulsifier-free emulsion polymerization method. The as-synthesized colloidal suspension was appeared white in color as shown in the photograph (Fig. 4.1a). DLS spectrum in fig. 4.1b. shows that the hydrodynamic size of the particle is about 230 nm and the polydispersity index (PDI) of the colloid was very low as 0.003, indicating that the particles are highly monodispersed. Depending upon the polarity and hydrophilicity of co-monomers (styrene, MMA, and AA), polymerization reaction facilitates core-shell microsphere formation, which is very distinct from the TEM image shown in Fig. 4.1c. Each core-shell microsphere consisted of a highly hydrophobic polystyrene core and a highly hydrophilic poly (MMA-EGDMA-AA) hydrogel shell. EGDMA cross-links MMA and AA to form the hydrogel shell. The TEM image indicates that the average diameter of the microspheres was 200 ± 10 nm, and the thickness of the shell was about 45 ± 15 nm. Unlike polystyrene microsphere, the hydrophilic shell can absorb large amounts of water, which facilitates volume phase transition through hydrogel swelling/deswelling, which can be utilized for stimuli-responsive photonic crystal (RPC) fabrication. The carboxyl group anchored on the polymer chain of the outer layer (shell) increases the water affinity of the shell, hence the CS microsphere exhibit very large swelling in water. Additionally, compared to soft hydrogel shell, hard polystyrene core has a rigid structure which provides better structural stability and offers high-quality RPC film.

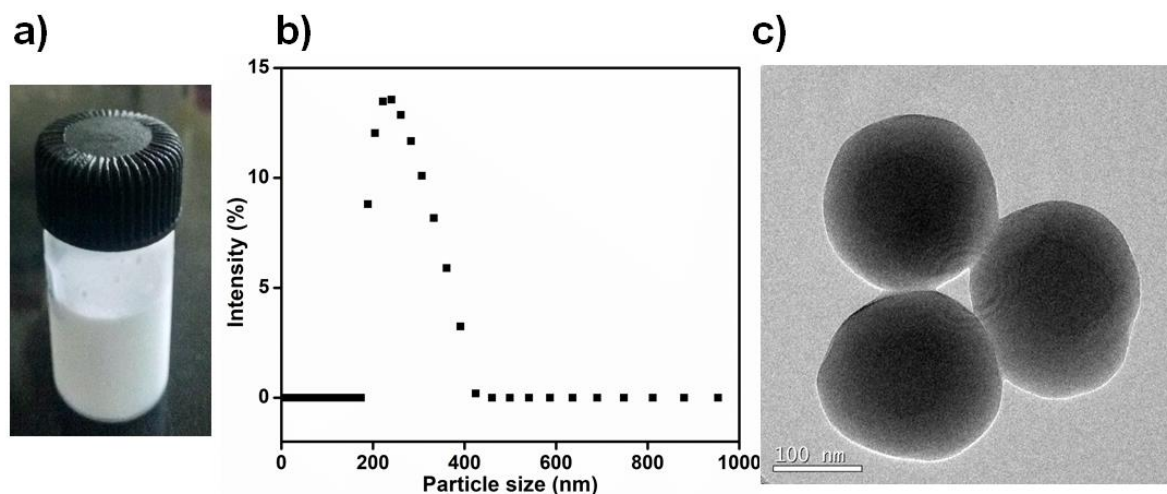


Fig. 4.1. a) Digital photograph b) DLS spectrum of CS microsphere suspension, and c) TEM image of CS microspheres

The FT-IR spectra of the CS microsphere is shown in Fig. 4.2a The aromatic C-H stretching vibration peaks at 2920 cm^{-1} and 3026 cm^{-1} and aromatic C=C stretching vibration peak at 1600 cm^{-1} , 1492 cm^{-1} , and 1451 cm^{-1} were due to the presence of benzene rings indicating the existence of polystyrene core in CS microsphere. The peak at 1730 cm^{-1} originated from the carbonyl stretching of poly (MMA-EGDMA-AA) hydrogel shell. Additionally, XPS analysis was performed to evaluate the presence of carboxyl functional group on the CS microsphere surface. The XPS survey spectra and atomic % of CS microsphere are shown in Fig. 4.2b and Table 4.1, respectively which show C (90.6%), and O (9.4%) as major elements. The elemental composition of PS microspheres measured from XPS survey spectra (chapter 2) is also shown in Table 4.1. The elemental composition of oxygen in CS microspheres was higher compared to PS microspheres, which is due to the presence of poly (MMA-EGDMA-AA) hydrogel shell. Narrow scan of C1s shown in Fig. 4.2c reveals the presence of C-C, C-O, O-C=O bonds and $\pi\text{-}\pi^*$ shake-up satellites peak originating from c aromatic ring. Obviously, the presence of O-C=O bond at 288.0 eV indicates the presence of carboxyl group available for further functionalization.

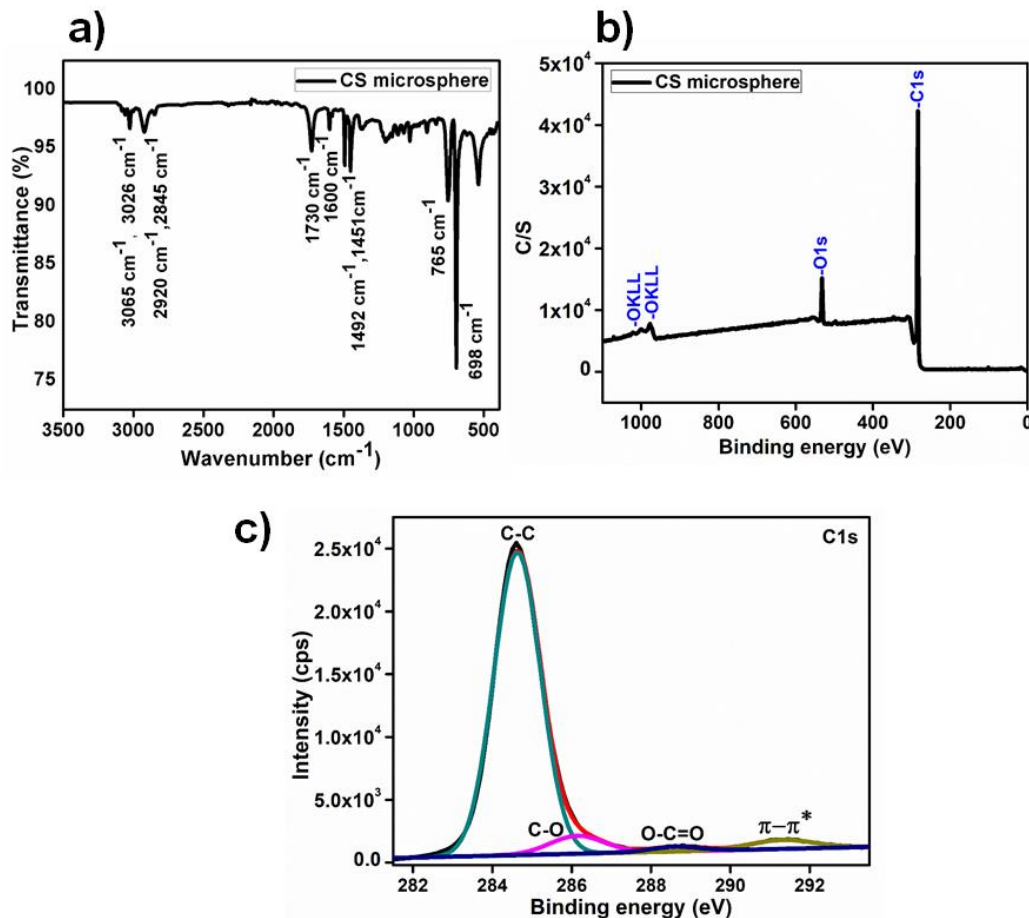


Fig. 4.2. a) FT-IR spectra b) XPS survey spectra and c) C1s narrow scan of CS microspheres.

Table 4.1. Atomic % of CS and PS microspheres from XPS data.

Element	Atomic %	
	CS	PS
C1s	90.6%	95.9%
O1s	9.4%	3.3%

The TGA and DSC curves of CS microspheres are shown in Fig. 4.3a and b, respectively. TGA thermogram indicates that the temperature at which 50 % weight loss occurs ($T_{0.5}$) was at 418 °C. $T_{0.5}$ of PS microsphere was 414 °C (Chapter 2). Compared to PS microspheres, $T_{0.5}$ of CS microsphere was higher, which may be due to the presence

of poly (MMA-EGDMA-AA) hydrogel shell. From the DSC thermogram the glass transition temperature (T_g) was found to be 130 °C, which was also higher than that of PS microsphere (T_g of PS microsphere was 106 °C, Chapter2), may be also due to the presence of poly (MMA-EGDMA-AA) hydrogel shell.

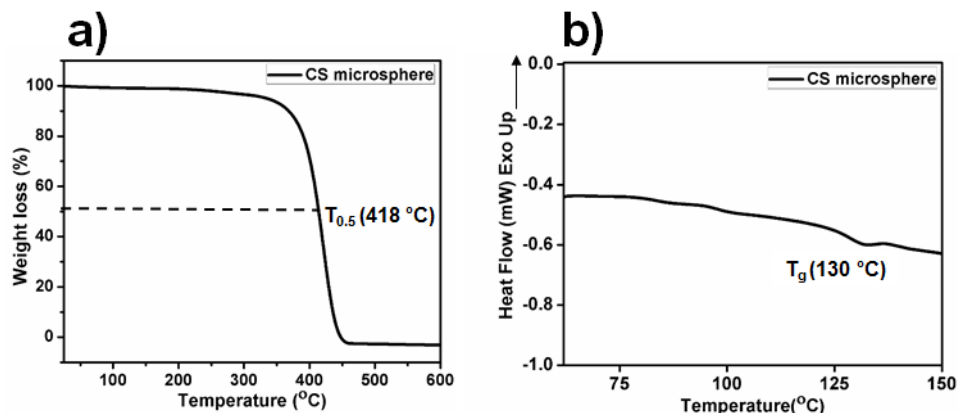


Fig. 4.3. a) TGA and b) DSC curve of CS microspheres.

4.4.2. Fabrication of CS microsphere-based PCs (CS-RPCs)

Further, utilizing the CS microsphere as a building block, self-assembly of CS microspheres (CS-RPC) were prepared by vertical deposition method onto a hydrophilic glass substrate. The digital photograph of CS-RPC in Fig. 4.4.a show bright green color. The SEM image depicted in Fig. 4.4.b shows a well-ordered close-packed arrangement of CS microspheres in the RPC. UV-Vis reflection spectra are shown in Fig. 4.4.c clearly indicated the reflection maxima (λ_{max} or PBG) at 466 nm.

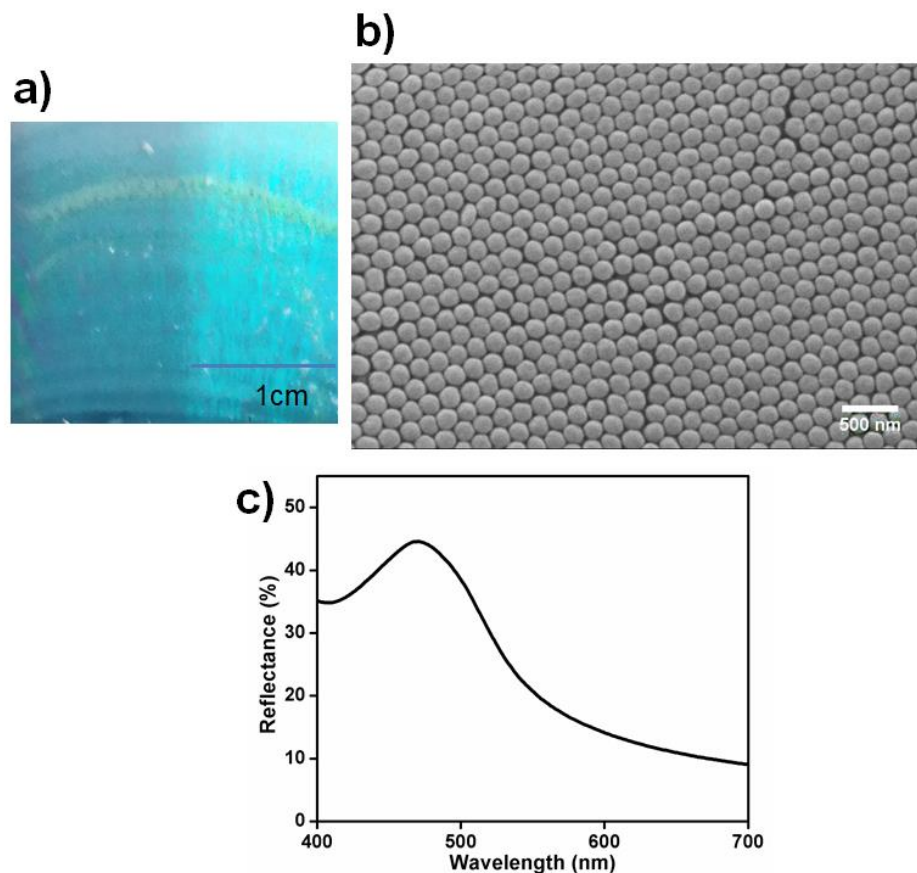


Fig. 4.4. a) Digital photograph, b) SEM image and c) reflectance spectra of CS-RPC respectively.

Further, we investigated the angular-dependence of structural color from the ordered structure of as-prepared CS-RPC. Interestingly, the photograph of RPC shown in fig. 4.5.a indicate almost identical color at all viewing angles. In practice, devices such as color display and sensors require a low angle-dependence of structural color materials. Interestingly, herein we obtained PC having low angle-dependent structural color. It is well-known that the angle dependence of structural color is determined by the degree of order of building block (colloidal microspheres) of CPC.²⁹ If the constituent particles of PC are arranged in long-range order, structural color varies with viewing angle, and short-range ordered colloidal particle of CPC impart low angle-dependence of structural color.²⁹ Astonishingly, PDI of CS microsphere was 0.003, which was very low, and the arrangement of the CS microsphere in the current study shows long-range order (SEM image shown fig. 4.4.b), and hence the RPC is expected to show angle-dependent

structural color. Interestingly, it is noted that the as-synthesized core-shell microspheres are lacking uniform shape and the thickness of shell around the polystyrene core is different in different regions (TEM image shown in fig. 4.1. c), making the periodicity in self-assembled PC structure of comparatively short-range order, henceforth making the structure isotropic. In detail, fig. 4.5.b and c show the schematic representation of the close-packed arrangement of uniform and non-uniform CS microsphere in CS-PCs, respectively. In fig. 4.5.b microsphere is uniform having the same thickness of shell around all the region of the core, and the PC film of such a CS microsphere shows not only long-range order of CS microsphere but also long-range order in the periodic arrangement of both core and shell in CS-PCs. Since it is anisotropic, structural color may change with viewing angle. However, CS-microsphere that we synthesised was non-uniform in shape (TEM image in fig. 4.1c). In fig. 4.5.c, CS microsphere has uniform size (since we obtained low PDI), but the thickness of the shell is not uniform around all the regions of the core (TEM image in fig. 4.1c). Even though PC made of such a CS microsphere shows long-range order in the arrangement of CS microspheres (SEM image in fig. 4.4b), if we separately consider core and shell, the arrangement of both the core and the shell is short range. Since it is isotropic in the arrangement of core and shell, structural color may not change with viewing angle. Therefore, the self-assembled PC architecture in the current study shows angle-independent structural color, which favours the applications of color displays and sensors. We consider the self-assembled structure of the CS microsphere as photonic crystalline structure (but not as amorphous structure), since it has long-range order in the CS microsphere arrangement.

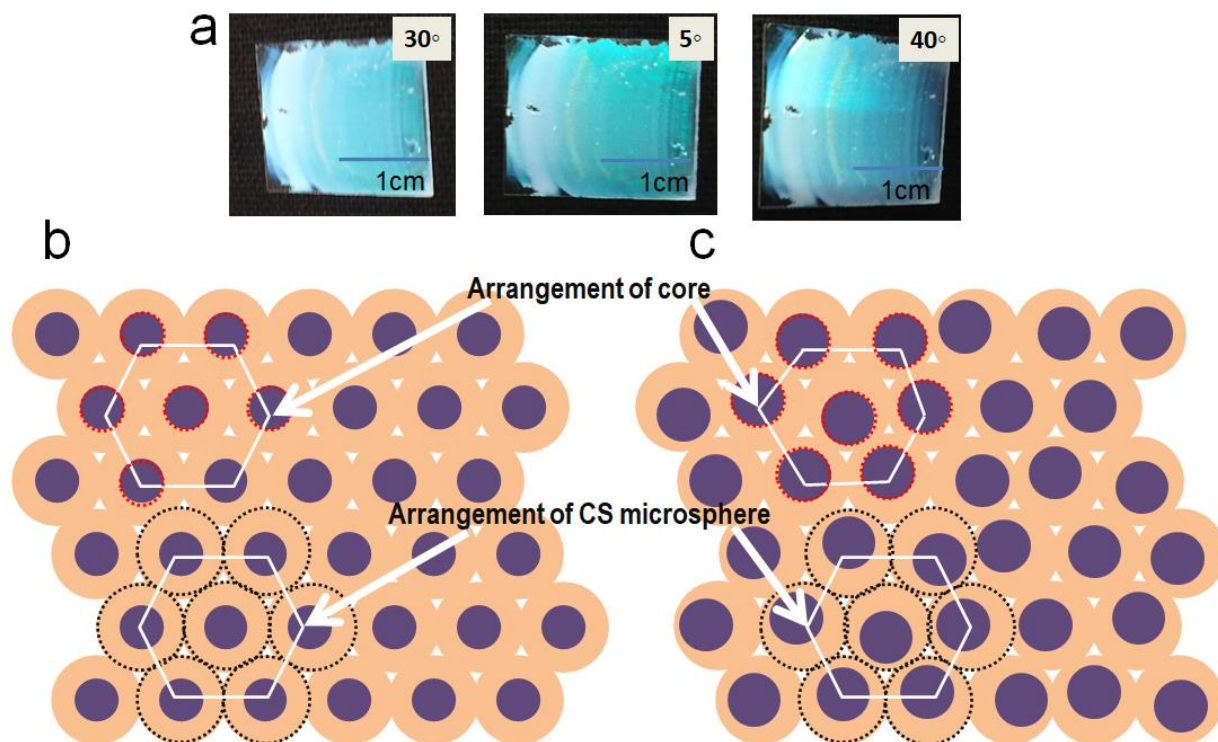


Fig. 4.5. a) Digital photographs of CS-RPC at various viewing angle, b) and c) represents schematic representation of arrangement of uniform and non-uniform CS microsphere in CS-RPC, respectively.

In order to increase the structural stability of RPC towards analyte solution, a composite film having self-assembled CS microspheres embedded in PVA matrix was prepared as mentioned in the experimental section. Hereafter it is abbreviated as PVA-RPC. The digital photograph and OM image of PVA-RPC film shown in fig. 4.6.a and b depicts its green structural color obtained using CS microsphere assembly. Their corresponding SEM image shown in fig. 4.6.c indicates the orderly arrangement of CS microspheres even in PVA-RPC. As in the case of CS-RPC, PVA-RPC also showed an angle-independent structural color. When we immerse PVA-RPC in water, the film structure was maintained even after swelling in water. The swelling of the hydrogel shell may be non-uniform, and the non-uniform swelling/deswelling on non-swelling glass substrate in the case of CSPC (CSPC has no PVA matrix) makes the film structure unstable towards the water. In the case of PVA-RPC, the ordered structure of CS microsphere was locked

by a non-swelling PVA matrix. Since both PVA matrix and glass film are non-swelling and swelling/deswelling of CS microsphere is within the PVA matrix, PVA-RPC film shows structural stability towards swelling/deswelling in water. This system avoids the collapse of CS microsphere arrangement towards water and stimuli-responsive PC of such a film may increase the sensor performance in that direction.

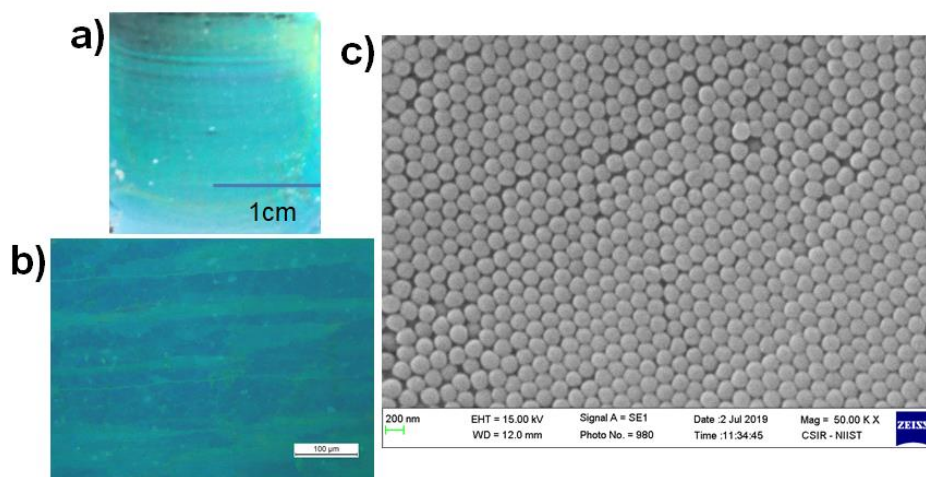


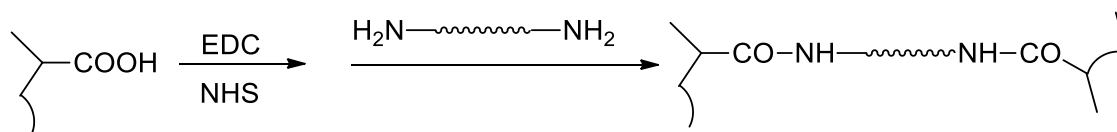
Fig. 4.6. a), b) and c) represents digital photograph, OM image and SEM micrograph of PVA-RPC film, respectively.

4.4.3. Fabrication of photonic crystals-based aptasensor (RPC-A) and sensing of omethoate

It is well-known that PCs of stimuli-responsive hydrogel undergo volume changes towards analyte molecules, leading to variation in center-to-center spacing of building blocks (colloidal microspheres), which impart changes in structural color. Such a color change under external stimuli can be used for visual detection applications. The photonic crystal aptasensor (RPC-A) was prepared by functionalizing the core-shell microsphere of PC (PVA-RPC system) with omethoate selective DNA-aptamer via the well-known EDC-NHS coupling (Scheme 4.2). The RPC-A can selectively bind omethoate in aqueous solution leading to changes in the periodicity of PC. The aptamer sequence was selected based on a previous report³¹ in which the aptamer sequence, AAG CTT GCT TTA TAG CCT GCA GCG ATT CTT GAT CGG AAA AGG CTG AGA GCT ACG C, have been identified for the selective binding of omethoate by SELEX technique. In the present study, we chose the same aptamer sequence as the recognition probe for omethoate

detection. The selective binding to omethoate was achieved by the secondary structure of aptamer where the DNA sequence is subjected to conformational changes resulting in the formation of loops through weak interactions to capture target molecules. Wang Li *et al.* have simulated the secondary structure of the aptamer sequence using DNAMAN software and they have estimated the equilibrium dissociation constant for omethoate as $2.5 \mu\text{M}$.³¹

However, the binding of aptamer with omethoate is not easy to quantify for screening omethoate. In contrast, the selective binding of omethoate with RPC-A makes the target pesticide sensing easy and inexpensive. The recognition of omethoate by the single-stranded aptamer impart conformational change of the sequence to capture the pesticide, causing the shrinkage of the hydrogel shell structure of CS microsphere. Thus the diffraction peak of PVA-RPC will be blue shifted. Further, the Bragg diffraction peak could be used to screen a range of omethoate concentration.



Scheme 4.2. Covalent coupling of aptamer with carboxyl group of CS microsphere in PVA-RPC via EDC-NHS coupling.

To prepare RPC-A, the PVA-RPC was activated with EDC-NHS solution and treated with aptamer solution. Aptamer functionalization on poly(MMA-EGDMA-AA) hydrogel shell through amide bond (-CO-NH-) was confirmed by XPS analysis. The XPS survey spectra and atomic % of PVA-RPC and RPC-A were depicted in Fig. 4.7.a, b and in Table 4.2 respectively, which show the presence of N as an additional element in RPC-A. The Nitrogen peak arise from the aptamer bonded to the CS microsphere shell. Phosphorus atom from the aptamer structure was not detected by XPS since compared to other elements, the atomic % of P is very low, and the composition is not within the detection limit of XPS. Compared to PVA-RPC, atomic % of carbon in RPC-A was higher due to an increase in carbon content after aptamer functionalization. The high-resolution C1s spectra shown in Fig. 4.7.c shows the presence of C=O, C-O, C-N and C-

C/C=C. The C-N bond can be attributed to the presence of amide bond. The presence of amide bond was further confirmed by narrow scan N1s spectrum (Fig. 4.7.d), which showed the presence of C=N, N-C=O and N-H. Morphology of the resultant functionalized CPC was investigated using SEM. The SEM image shown in Fig. 4.7.e reveals the regular and hexagonal close-packed arrangement of core-shell microsphere assembly, suggesting structural stability of PVA-RPC film towards aptamer functionalization.

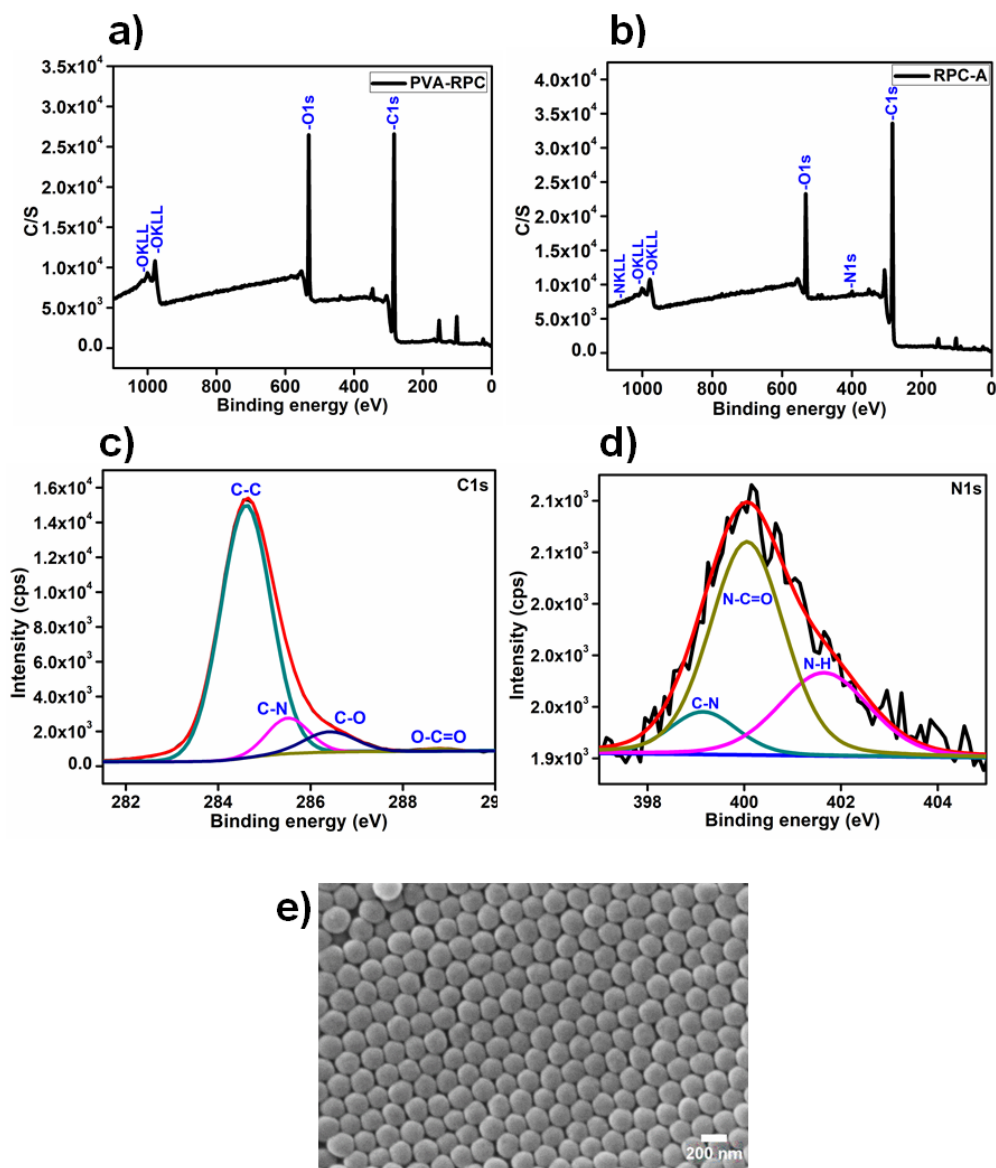


Fig. 4.7. a), b) represent XPS survey spectra of PVA-RPC and RPC-A respectively, c), d) represents C1s and N1s narrow scan of RPC-A and e) represents the SEM micrograph of RPC-A film.

Table 4.2. Atomic % of PVA-RPC and RPC-A.

Sample	Atomic %		
	C	O	N
PVA-RPC	71.3	28.7	-
RPC-A	80.0	19.0	1.1

The PBG of CPC can be calculated using Bragg's diffraction model.³²

$$\lambda_{max} = 2d_{(111)}(n_{eff}^2 - \sin^2\theta)^{1/2} = 2(2/3)^{1/2} D(n_{eff}^2 - \sin^2\theta)^{1/2}$$

where, λ_{max} represents the wavelength maxima of reflection peak, $d_{(111)}$ is the interplanar distance between adjacent (111) crystallographic planes, D is the sphere diameter and n_{eff} is the effective refractive index of CS-RPC film which is obtained from the equation, $n_{eff}^2 = \sum f_i n_i^2$, where n_i is the refractive index of CS microsphere and air voids and f_i is the corresponding volume fraction. According to the modified Bragg equation, λ_{max} changes when either interplanar distance or effective refractive index of PC structure is changed. Hence, prior to omethoate response studies, RPC-A was first washed and equilibrated in deionised water for 4 hrs. RPC-A was equilibrated in deionized water in order to minimize the effect of λ_{max} shift due to water infiltration into the shell of CS microspheres and voids of RPC-A during omethoate sensing. After equilibrating in deionized water, λ_{max} of dried RPC-A was shifted from 470 nm to 509 nm and the corresponding reflection spectra are shown in Fig. 4.8.

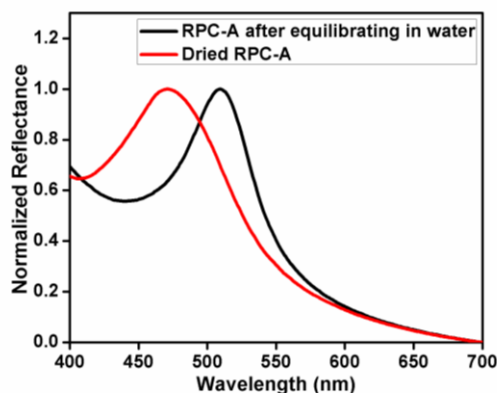


Fig. 4.8. Reflectance spectra of dried RPC-A and RPC-A after equilibrating with water.

To check the stimuli-response of RPC-A, the reflection spectra and corresponding λ_{\max} of RPC-A film in different omethoate solutions were taken and are shown in Fig. 4.9a and Fig. 4.9b respectively. As shown in Fig. 4.9a obvious blue shift was observed with an increase in omethoate concentration from 0 μM to 10 μM . The original Bragg diffraction wavelength of 509 nm was shifted to 506, 504, 498, 474, 472 when the omethoate concentration was increased to 0.3, 0.6, 1.2, 2.4 and 10 μM respectively. Additionally, no obvious blue shift was observed when omethoate concentration was increased from 10 μM to 30 μM , suggesting the detection range of the aptasensor as 0.3 to 10 μM . Interestingly, the response of aptasensor towards omethoate was fast facilitating rapid sensing and the structure of RPC-A film was stable towards omethoate solution, which increases the credibility of Bragg diffraction peak. In order to confirm omethoate binding of RPC-A, a control experiment was performed with a non-functionalized PVA-RPC film. The reflectance spectra of PVA-RPC towards a range of concentrations of omethoate solution are shown in Fig. 4.9c. The reflection peak of PVA-RPC showed no peak shift, revealing the specific binding of omethoate with aptamer is the main reason for the diffraction peak shift in the case of RPC-A. Additionally, for further improvement in sensor performance, higher sensitivity and the peak shift over the entire visible region should be achieved.

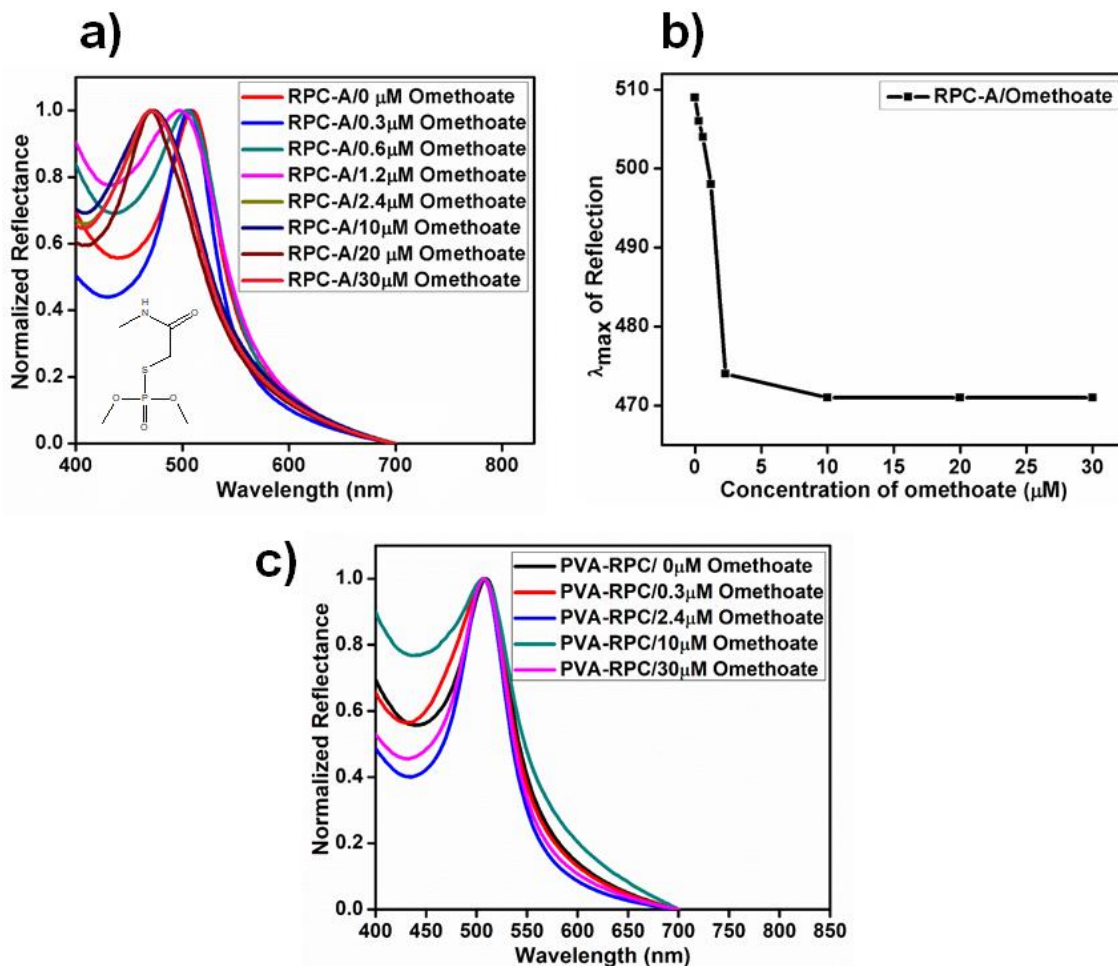


Fig. 4.9. a) and b) represents reflectance spectra and corresponding λ_{\max} of RPC-A film in different concentrations of omethoate solutions, respectively, c) represents reflectance spectra of non-functionalized PVA-RPC film in different omethoate solutions.

4.4.4. Selectivity studies of RPC-A

The selectivity of RPC-A was demonstrated by studying the response to other environmentally relevant pesticides such as methyl parathion and carbofuran, and the Bragg diffraction peak were analyzed. Corresponding reflection spectra and the λ_{\max} of reflection of RPC-A towards methyl parathion and carbofuran are shown in Fig. 4.10, which clearly indicated no peak shift. Hence, it was observed that only omethoate can bind to the RPC-A and which induce a significant

diffraction shift, suggesting the possibility of the RPC-A film in the selective sensing of a wide concentration range of omethoate.

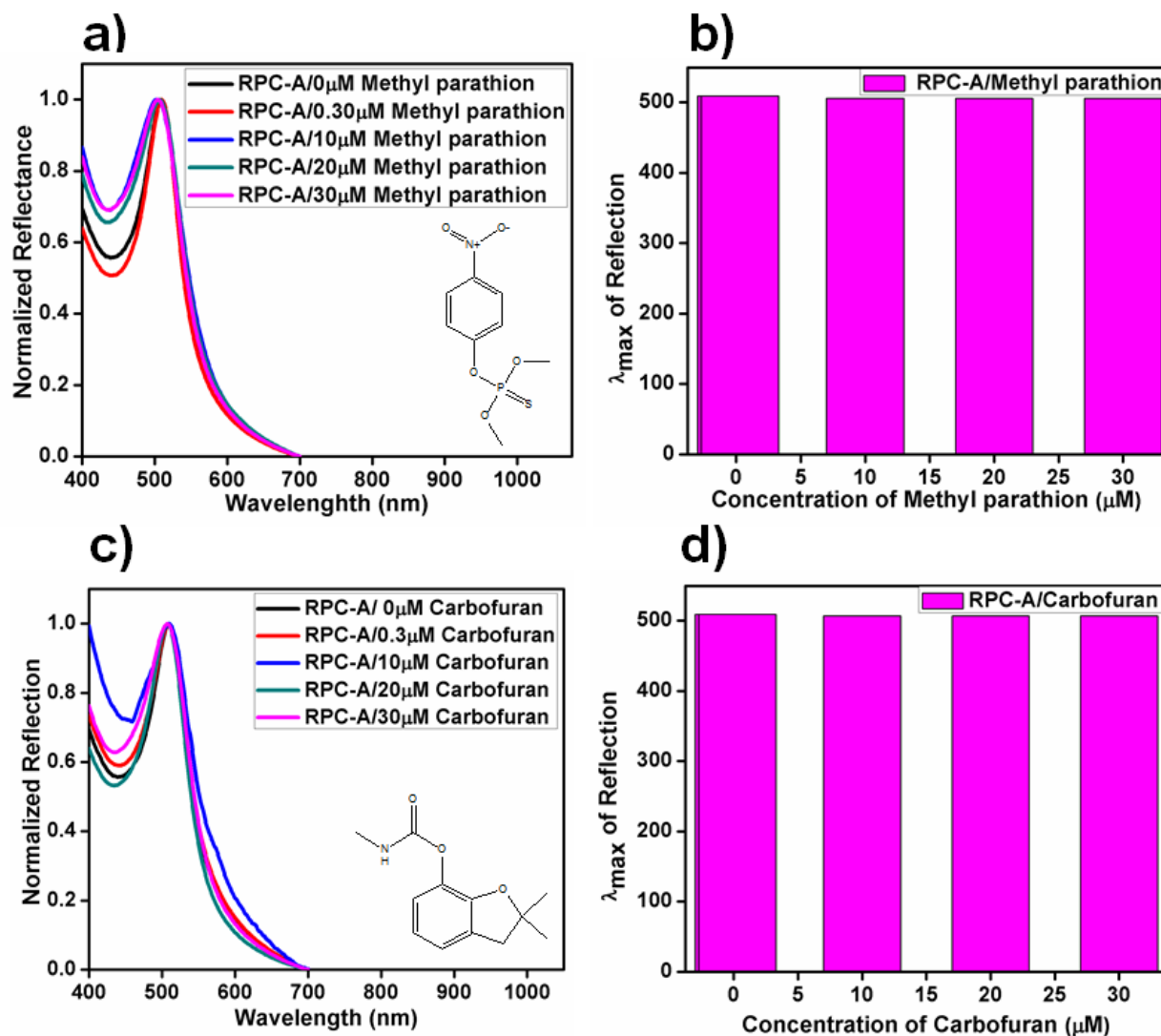


Fig. 4.10. a), b) represents reflectance spectra and corresponding λ_{\max} of RPC-A film in different methyl parathion solutions, respectively and c), d) represents reflectance spectra and corresponding λ_{\max} of RPC-A film in different carbofuran solutions, respectively.

4.5. Conclusions

In summary, we have successfully demonstrated stimuli-responsive single stranded DNA-aptamer functionalized core-shell microsphere PC for the selective detection of omethoate. The aptasensor was fabricated using monodispersed PS@poly(MMA-EGDMA-AA) core-shell microspheres embedded within the PVA matrix. The specific binding of target pesticide with aptamers causes shrinkage of hydrogel shell, which was observed as a corresponding blue shift in the Bragg diffraction peak position of the aptasensors. The Bragg shift can be used for the qualitative estimation of the target pesticide. More importantly, the aptasensor showed low angle-dependent structural color, which is highly desirable for sensing performance. This aptasensor could detect a wide concentration range of omethoate. In addition, improvements in sensitivity and the peak shift over the entire visible region would significantly expand the applicability of the aptasensor.

References

1. M. Catalá-Icardo, L. Lahuerta-Zamora, S. Torres-Cartas and S. Meseguer-Lloret, *Journal of Chromatography A*, 2014, **1341**, 31-40.
2. X. Sun and X. Wang, *Biosensors and Bioelectronics*, 2010, **25**, 2611-2614.
3. N. Huang, Y. Qin, M. Li, T. Chen, M. Lu and J. Zhao, *Analyst*, 2019, **144**, 3436-3441.
4. A. Bahreyni, R. Yazdian-Robati, M. Ramezani, K. Abnous and S. M. Taghdisi, *Microchimica Acta*, 2018, **185**, 272.
5. H. Shi, G. Zhao, M. Liu, L. Fan and T. Cao, *Journal of Hazardous Materials*, 2013, **260**, 754-761.
6. Q. Liu, H. Wang, P. Han and X. Feng, *Analyst*, 2019, **144**, 6025-6032.
7. C. Zhang, B. Lin, Y. Cao, M. Guo and Y. Yu, *Journal of Agricultural and Food Chemistry*, 2017, **65**, 3065-3073.
8. S. Pang, T. P. Labuza and L. He, *Analyst*, 2014, **139**, 1895-1901.
9. Y. Takeoka and M. Watanabe, *Langmuir*, 2003, **19**, 9104-9106.

10. D. Yan, W. Lu, L. Qiu, Z. Meng and Y. Qiao, *RSC Advances*, 2019, **9**, 21202-21205.
11. Y. Fang, Y. Ni, S.-Y. Leo, C. Taylor, V. Basile and P. Jiang, *Nature Communications*, 2015, **6**, 7416.
12. K. Sumioka, H. Kayashima and T. Tsutsui, *Advanced Materials*, 2002, **14**, 1284-1286.
13. H. Hu, Q.-W. Chen, K. Cheng and J. Tang, *Journal of Materials Chemistry*, 2012, **22**, 1021-1027.
14. K. Lee and S. A. Asher, *Journal of the American Chemical Society*, 2000, **122**, 9534-9537.
15. Y. Zhang, Q. Fu and J. Ge, *Nature Communications*, 2015, **6**, 7510.
16. C. Zhang, M. D. Losego and P. V. Braun, *Chemistry of Materials*, 2013, **25**, 3239-3250.
17. M. M. Ward Muscatello, L. E. Stunja and S. A. Asher, *Analytical Chemistry*, 2009, **81**, 4978-4986.
18. J.-T. Zhang, X. Chao, X. Liu and S. A. Asher, *Chemical Communications*, 2013, **49**, 6337-6339.
19. J.-T. Zhang, N. Smith and S. A. Asher, *Analytical Chemistry*, 2012, **84**, 6416-6420.
20. W. Liu, L. Li, S. Liu, B. Liu, Z. Wu and J. Deng, *Journal of Materials Chemistry C*, 2019, **7**, 8946-8953.
21. B.-F. Ye, Y.-J. Zhao, Y. Cheng, T.-T. Li, Z.-Y. Xie, X.-W. Zhao and Z.-Z. Gu, *Nanoscale*, 2012, **4**, 5998-6003.
22. Z. Pan, J. Ma, J. Yan, M. Zhou and J. Gao, *Journal of Materials Chemistry*, 2012, **22**, 2018-2025.
23. M. Chen, L. Zhou, Y. Guan and Y. Zhang, *Angewandte Chemie International Edition*, 2013, **52**, 9961-9965.
24. X. Feng, J. Xu, Y. Liu and W. Zhao, *Journal of Materials Chemistry B*, 2019, **7**, 3576-3581.
25. J. H. Holtz, J. S. W. Holtz, C. H. Munro and S. A. Asher, *Analytical Chemistry*, 1998, **70**, 780-791.
26. L. Nucara, V. Piazza, F. Greco, V. Robbiano, V. Cappello, M. Gemmi, F. Cacialli and V. Mattoli, *ACS Applied Materials & Interfaces*, 2017, **9**, 4818-4827.

27. J. H. Moon and S. Yang, *Chemical Reviews*, 2010, **110**, 547-574.
28. N. Vogel, M. Retsch, C.-A. Fustin, A. del Campo and U. Jonas, *Chemical Reviews*, 2015, **115**, 6265-6311.
29. P. Liu, L. Bai, J. Yang, H. Gu, Q. Zhong, Z. Xie and Z. Gu, *Nanoscale Advances*, 2019, **1**, 1672-1685.
30. P. Jiang, J. F. Bertone, K. S. Hwang and V. L. Colvin, *Chemistry of Materials*, 1999, **11**, 2132-2140.
31. L. Wang, X. Liu, Q. Zhang, C. Zhang, Y. Liu, K. Tu and J. Tu, *Biotechnology letters*, 2012, **34**, 869-874.
32. V. V. Vipin, P. R. Chandran, A. M. Ramachandran, A. P. Mohamed and S. Pillai, *New Journal of Chemistry*, 2019, **43**, 16264-16272.

Chapter 5

Summary and Scope of Future Work

This thesis is focused on the bio-inspired structural color of polymer-based colloidal photonic crystals (CPC). The main objective of the work was to explore the applications of CPCs in different fields. Size controlled synthesis of highly monodispersed polymeric microspheres and the use of microspheres for the fabrication of vibrant colored CPCs has been studied systematically. Highly monodispersed polymeric microspheres were synthesized by emulsion polymerization method and large area CPCs with periodic arrangement of microspheres were fabricated via vertical deposition method. The PBG of CPCs was tuned and these CPCs were used for structurally colored inverse opal PC (IO-PC) powder preparation, photonic crystal (PC) enhanced fluorescence, and stimuli-responsive PCs (RPCs) fabrication.

Firstly, polystyrene microspheres having very low polydispersity index (PDI) have been synthesized and were characterized using various techniques. Additionally, the PS colloid was stable as indicated by the zeta potential values, suggesting its applicability in fabricating good quality CPCs. PS based CPCs (PS CPCs) were fabricated on plasma-treated hydrophilic glass substrates as well as on flexible polymer films. Additionally, PS CPCs were employed as a sacrificial template for the preparation of three-dimensionally ordered macroporous (3D-OM) silica IOPC. Charcoal flakes were used for regaining the structural color of silica IO-PC powder by way of absorbing scattered light.

Further, we demonstrated augmented fluorescence enhancement of guest dye molecule by the combined effect of macrocycle-based host-guest formation and PBG effect. Compared to the existing method of PC enhanced fluorescence with complex CPC architecture, the new strategy with the use of host-guest complex of cucurbit[7]uril (CB7) with rhodamine B (RhB), was very simple. We studied the effect of PBG position on the fluorescence enhancement by taking three different structurally colored CPCs. The contribution of the effect of PBG and host-guest complexation on the fluorescence intensity of RhB was studied in detail. The combined effects of the CB7-RhB host-guest formation and the PBG effect of CPCs significantly contribute to achieving over 150-fold fluorescence enhancement of RhB. Encapsulation of RhB in CB7 helped to prevent the aggregation-induced self-quenching, which increased the fluorescence intensity. The

slow photon effect at the PBG edge helped in enhanced light absorption and extraction, which further facilitated fluorescence signal amplification.

Finally, we demonstrated an aptasensor based on stimuli-responsive photonic crystals (RPC-A) of core-shell (CS) microspheres for the selective detection of an organophosphorus pesticide. Highly monodispersed PS@poly(MMA-EGDMA-AA) core-shell microspheres were synthesized, and CPCs were made within the PVA matrix. We successfully functionalized the CPCs with DNA-aptamer, which was used as the recognition probe. The DNA-aptamer facilitated selective detection of omethoate via the specific binding of target pesticide. RPC-A showed a shift in diffraction position towards omethoate solution by shrinkage of hydrogel shell. It was found that the RPC-A was not responsive towards the other two commonly used pesticides, methyl parathion and carbofuran. Importantly, the aptasensor showed low angle-dependent structural color, which is highly desirable for sensing performance, and the shift in the Bragg diffraction position can be explored to detect a wide concentration range of omethoate.

Altogether, the present thesis successfully demonstrated the potential use of CPC based bio-inspired structural color materials in some of the important applications such as 3D-OM silica IOPC, fluorescence enhancement of a conventional dyes (RhB) and an RPC-A for pesticide detection, which can be advantageous for several associated research works.

Future projections

1. Development of low-angle dependent structural color display by the coating of silica IO-PC powder
2. CPCs-based inks and large area printing of brilliant structural colors for security applications
3. IR emitting plasmonic/quantum dots incorporated colloidal photonic crystals for anti-counterfeiting applications
4. Highly sensitive fluorescence-based detections of analyte molecules by the new method of fluorescence enhancement

5. Development of dual-mode strip-based aptasensor for the selective and accurate detection of particular analytes

THESIS OUTPUT

List of Publications

1. **V. V. Vipin**, Parvathy R. Chandran, Animesh M. Ramachandran, A. P. Mohamed, Saju Pillai, Photonic band gap effect and dye-encapsulated cucurbituril-triggered enhanced fluorescence using monolithic colloidal photonic crystals, *New J. Chem.*, 2019,43, 16264-16272.
2. **V. V. Vipin**, Parvathy R. Chandran, A. P. Mohamed, Saju Pillai, Stimuli-responsive, DNA Aptamer-functionalized colloidal core-shell photonic crystal with low angle dependent structural color for the selective detection of omethoate (*manuscript under preparation*)
3. **V. V. Vipin**, Parvathy R Chandran, Silpa T.S., Mohamed A. P., Saju Pillai, Non-iridescent structural colors of silica inverse opal photonic crystal powder and charcoal flakes. (*manuscript under preparation*)
4. Meghana Mary Thomas, Parvathy R Chandran, **V. V. Vipin**, Mohamed A. P., Peter Kingshott, Saju Pillai, Ultrafast, simple, visual mode of acetone detection using core-shell based responsive colloidal photonic crystals (*under review*)

List of Conference Papers and Posters

1. Presented a paper entitled "Polystyrene colloidal crystal template for responsive photonic hydrogel", Polymer Conference for Young Researchers (PCYR-2014), held at CSIR-NIIST, Thiruvananthapuram, Kerala.
2. Presented a paper entitled "Responsive inverse opal photonic hydrogel for sensing application", International Symposium on Polymer Science and Technology (MACRO-2015), held at Kolkata, West Bengal.
3. Presented a paper entitled "Hierarchical opal and inverse opal- photonic crystal sensor platform based on mono-component colloidal crystal" Polymer

Conference for Young Researchers (PCYR-2015), held at CSIR-NIIST, Thiruvananthapuram, Kerala.

4. Presented a paper entitled “Amplifying fluorescence from opal and inverse opal- A fluorescence-based sensor platform based on 3D photonic crystal”, Materials Research Society of India (MRSI) Symposium Advanced Materials for Sustainable Applications, held at CSIR-NEIST, Assam.
5. Presented a paper entitled “Fabrication of large area thin film photonic crystals for IR reflective transparent coatings”, International Conference on Soft Materials (ICSM 2016), held at Jaipur.
6. Presented a paper entitled “Development and fabrication of core-shell microsphere based photonic crystal sensors for stimuli responsive applications”, International Conference on Nanotechnology: Ideas, Innovations and Initiatives-2017 (ICN: 3I-2017), held at IIT Roorkee.
7. Presented a paper entitled “Cucurbituril mediated enhanced fluorescence on colloidal photonic crystal”, Polymer Conference for Young Researchers (PCYR-2018), held at CSIR-NIIST, Thiruvananthapuram, Kerala.

Awards

1. **Best poster award:** Cucurbituril mediated enhanced fluorescence on colloidal photonic crystal, **V. V. Vipin**, Animesh M. Ramachandran, Parvathy R. Chandran, Saju Pillai, Polymer Conference for Young Researchers (PCYR-2018), held at CSIR-NIIST, Thiruvananthapuram, Kerala.